DETECTOR DEVELOPMENT AND POLARIZATION ANALYSES FOR THE ATACAMA COSMOLOGY TELESCOPE

A Dissertation

Presented to the Faculty of the Graduate School

of Cornell University

in Partial Fulfillment of the Requirements for the Degree of

Doctor of Philosophy

by

Brian James Koopman

December 2018

DETECTOR DEVELOPMENT AND POLARIZATION ANALYSES FOR THE ATACAMA COSMOLOGY TELESCOPE

Brian James Koopman, Ph.D.

Cornell University 2018

We are currently in an era of precision cosmology. Study of the Cosmic Microwave Background (CMB) has been central to our understanding of the universe ever since its discovery in 1965. Recent results from the Planck satellite have provided the best constraints on the 6-parameter $\Lambda\mathrm{CDM}$ model, the "standard model" of cosmology. In order to improve these constraints we must further the development of the technologies used to measure the CMB as well as our understanding of their associated systematics.

The Atacama Cosmology Telescope Polarimeter (ACTPol) and its successor instrument, known as Advanced ACTPol (AdvACT), are polarization sensitive upgrades to the Atacama Cosmology Telescope (ACT). ACT is an off-axis Gregorian telescope with a 6m primary reflector and a 2m secondary reflector. The ACTPol and AdvACT instruments utilize kilo-pixel scale arrays of superconducting transition edge sensor (TES) bolometers to measure the CMB anisotropies at frequencies ranging from 27-220 GHz. The increased spectral coverage of AdvACT will enable a wide range of CMB science, such as improving constraints on dark energy, the sum of the neutrino masses, and the existence of primordial gravitational waves. Precise polarization calibration can also enable improved constraints on cosmic polarization rotation.

In this thesis we present an overview of the AdvACT instrument before detailing the development of the AdvACT TES device geometries, which are tuned

specifically for each of AdvACT's five frequency bands (27, 39, 90, 150, and 220 GHz). Each detector couples to a single linear polarization. The angle of this coupling projected onto the sky is a critical calibration step in making maps of the CMB polarization. Any offset in this calibration angle can introduce a spurious B-mode polarization signal, resulting in non-zero EB and TB cross-correlation power spectra.

ACTPol uses a unique optical modeling based approach to this calibration. We present this procedure, as well as a method for directly measuring the relative angles of the detectors by use of a rapidly rotating polarizer. We also present maps of the polarized source Tau A, from the first three seasons of ACTPol at 90 and 150 GHz and discuss how these maps are affected by the polarization calibration. Finally, we discuss the telescope control, computer systems, and remote observations team which keep the telescope running, and briefly conclude with a summary that motivates improving calibration techniques for future CMB experiments.

BIOGRAPHICAL SKETCH

Brian Koopman graduated from Clark University in Worcester, MA in 2012, earning a double major in Physics and Mathematics with highest honors in Physics. While at Clark he studied the magnetic properties of 1D antiferromagnetic crystals, aided in the construction of a new scanning tunneling microscopy lab, and studied high temperature superconductors. He also had the opportunity to attend an NSF Research Experience for Undergraduates through Caltech at the Laser Interferometer Gravitational Wave Observatory (LIGO) site in Livingston, LA, studying the noise proprieties of piezoelectric actuators.

A few months after arriving at Cornell he joined the lab of Professor Michael Niemack. He has worked on different aspects of several telescope projects over his six years at Cornell, including the Atacama Cosmology Telescope (ACT), the CCAT-p telescope, and, more recently, the Simons Observatory (SO). As the first student in the group he has worked on many different projects over the years, ranging from custom written software for automated control of the He3/He4 dilution refrigerator in the lab, to the mapping of astrophysical sources from ACTPol data.

Brian was awarded a NASA Space Technology Research Fellowship (NSTRF) in 2013. His work under the fellowship has focused on the polarization systematics of the ACTPol telescope and the testing of new detectors for the Advanced ACT upgrade. Outside of this work he enjoys software development, particularly when it comes to automating systems and building web interfaces for various projects.

When not in the lab or on a mountain in Chile you can find Brian playing the Baritone saxophone in a local ska band, ¡Viva Mayhem![1], or with the Ithaca

[1] https://vivamayhem.com

Concert Band.

After leaving Cornell Brian will continue in the field of experimental cosmology, working on the Simons Observatory as a postdoc at Yale University. There he will work on data acquisition software.

To Mom –

for everything.

To Gram –

for all the great conversations we had.

To Lou –

for your dedication to your students.

I know you would have read these pages and been proud.

I miss you all immensely.

ACKNOWLEDGEMENTS

When I first came to graduate school I did not intend to work in experimental cosmology, but I don't think I could be happier with where I ended up. First, I'd like to thank my advisor, Mike Niemack, for taking me on as his first student, and for your encouragement and guidance, especially when I was first getting started. It's been a fun six years!

Working with the ACT collaboration has been an amazing opportunity, if only because of the wonderful people I get to work with. With around 100 people in the collaboration it'd be difficult to thank everyone, but I'd like to start by thanking collaborators at Princeton, especially Suzanne Staggs and Lyman Page, your enthusiasm for the science we do is infectious. And thanks to Suzanne for teaching me how to drive a manual transmission while at the site. Beyond Princeton I'd like to thank our other collaborating institutions and those who work there, at the University of Pennsylvania, the University of Michigan, NIST, Católica, UBC, and so many more.

I am also thankful to have had four great years with a NASA Space Technology Research Fellowship, which allowed me to travel to the site in Chile so many times. Ed Wollack always provided great conversations, from which I have learned so much.

I have really enjoyed my time at Cornell, and the students and postdocs in our group are really a major part of that. Working with you all – Shawn, Francesco, Pato, Jason, Eve, Nick, Cody, Paul, Galen, Sheroze, Kaiwen, Philip, Noah, Prah, Sarah Marie, Humna, and all of our summer students – has been a great experience. I've learned a lot from each of you over the past six years, and I hope that continues for many more. Outside of the Niemack group I have fond memories spending time with Jen, Jordan, Neil, Alex, Azar, Jonathan, Lorien,

Jacob, Jeff, Jon, Corky, Matt, and Andy. Thanks also to the group who regularly plays table tennis – Alexandra, Steve, Antoine, Valerio, Giulia, and especially to SeungCheon, who taught me my forehand loop.

I have had a lot of fun working on the computer systems at the site. Thanks to Matthew for answering all my various questions in this regard, and for teaching me how to map Tau A. And thanks to Adam for teaching me about colossus. I look forward to working with you both on the DAQ systems for SO. And speaking of the site, I want to thank all the remote observers who keep ACT running, especially those who were there from the start, Ben, Shawn, Matthew, Marius, Reneé, Emily, and Jon. Your work has led us to our current 30 strong team, a great example for how to manage remote observations.

There has been a stable site crew the past couple of years, to which I am grateful for keeping the telescope running, even if it means going up the mountain the middle of the night to fix whatever it is that has broken, or simply to push a button. Felipe Carrero and Max Fankhanel have made working at the site easy for us. The past site personal, Prajwal, Stephen, Felipe Rojas, and especially Alessandro (whose cooking I will never forget!) have been great to get to know and work with. Thanks for all your patience and hard work, without you the telescope could not run.

Thanks to Brian Keating for starting the conversation which led to collaboration on fabricating the large diameter wire grids. And thanks to his students, Fred Matsuda and Lindsay Lowry for answering all my questions and winding the actual grids, they really came out great!

If you know me at all I've probably told you about the band I play in, ¡Viva Mayhem![2] The group has really felt like family, and they've been there for me through all the ups and downs over the past five years. Paula, Dave, Jeremy,

[2] https://vivamayhem.com

Sean, Emily, Tito, Rob, Sam, Cam, Dacia, Kristen, Duncan, Madeline, and Jared, you mean the world to me, and have made my time in Ithaca all the more special. I'm looking forward to whatever the future has in store for us. And thanks to all the local bands, many of which have become close friends, Kitestring, Thru Spectrums, TeenCat, Junkyard Theory, and so many more. Keep making great music.

I'd also like to thank my family, Dad, Mom, Gram, Steve, Aunt Laura, Aunt Karen, Uncle Bub, Aunt Linda, Opa, Dorothy for your love and support. I would not be where I am today without you.

Lastly, I'd like to thank you, the reader. Your interest is appreciated.

TABLE OF CONTENTS

LIST OF TABLES

LIST OF FIGURES

CHAPTER 1

INTRODUCTION

Modern cosmology is based upon the Cosmological Principle, which can be formally stated as,

> Viewed on a sufficiently large scale, the properties of the Universe are the same for all observers [58].

Put another way, we say that the Universe is both homogeneous and isotropic, that is, it is the same in all locations (homogeneous) and in all directions (isotropic). This leads one to the conclusion that there is not anything special about our place in the Universe. While the idea dates back at least to Copernicus, it was an interpretation from Hubble that pushed us into today's era of modern cosmology.

In 1923 Hubble made observations of the apparent luminosity of Cepheids in the Andromeda Nebula. Using this information he calculated the distance to this and other nebulae. Combining this distance information with observations made the previous decade by Vesto Melvin Silpher of the redshifted spectral lines of these nebulae led Hubble, in 1929, to the conclusion that the recessional velocity of galaxies, that is their redshifts, increases with distance from us [101, 46]. This became known as Hubble's Law.

Hubble's law is consistent with an expanding universe. Extrapolating backwards would imply that at some point, these galaxies, which we measure to be moving away from each other, must have been closer together. A fluid, generally, is heated when compressed. If we think backwards in time, reversing the

expansion, compressing the matter in the universe, we realize the early universe must have been hotter and denser than at present.

In fact, looking back far enough we expect to find the Universe to be so hot that electrons do not stay bound to protons. At this point, when the Universe was less than 380,000 years old, we find a hot dense plasma of electrons, positrons, neutrinos, and photons (along with a small number of protons and neutrons). Photons would not travel far before scattering off of a free electron via Thompson scattering. This kept the radiation in thermal equilibrium with the hot dense matter.

As the Universe expands this hot matter cooled and became less dense. Eventually it cooled enough (to $\sim 3000\,\mathrm{K}$) that the electrons and protons could form neutral hydrogen. From this point, the photons no longer scattered off of free electrons (as they were bound to protons), and so they began free streaming. These photons have a characteristic black-body spectrum. Due to the expansion of the universe the effective temperature of these photons decreases to the $\sim 3\,\mathrm{K}$ that we see today. This 3 K radiation is known as the Cosmic Microwave Background (CMB) Radiation.

1.1 The Cosmic Microwave Background Radiation

In the 1940's Gamow and his colleagues first recognized that this background black-body radiation should exist [33, 6, 34]. And in 1950, Alpher and Herman estimated the present day temperature [7]. But it was not until 1965 that Arno Penzias and Robert Wilson accidentally discovered this background radiation while working on ultra-sensitive cryogenic microwave receivers for Bell Labs

[82]. This discovery would earn Penzias and Wilson the Nobel prize in 1978. The discovery of the CMB, and further study of it, has provided some of the best evidence for the Big Bang theory for the start of our Universe.

Over the past 53 years observations of the CMB have improved drastically. The black-body nature of this background radiation was first measured from the ground, but making this measurement from the ground proved difficult, often showing an excess over the expected black-body spectrum. The need to go to space became apparent. The Cosmic Background Explorer (COBE) first measured the black body spectrum of the CMB from space. Launched in November 1989, COBE reported the observed black-body spectrum a mere two months later, in January 1990 [101].

Since these initial measurements from COBE other satellites, such as WMAP and Planck, have measured the CMB with increasing precision. Additionally, ground based experiments, such as ACT and SPT, have mapped regions of the sky with higher resolution. From these maps we have found and studied galaxy clusters, through the thermal Sunyaev-Zel'dovich effect, and improved constraints on the Lambda CDM model for the early universe. Recently the capabilities of these high resolution ground based experiments has been expanded to include the ability to measure the polarization of the CMB. An example of the latest maps from ACTPol is shown in Figure 1.1.

1.1.1 CMB Polarization

The CMB is linearly polarized due to Compton scattering at the time of decoupling. Towards the end of recombination a quadrupole anisotropy can form

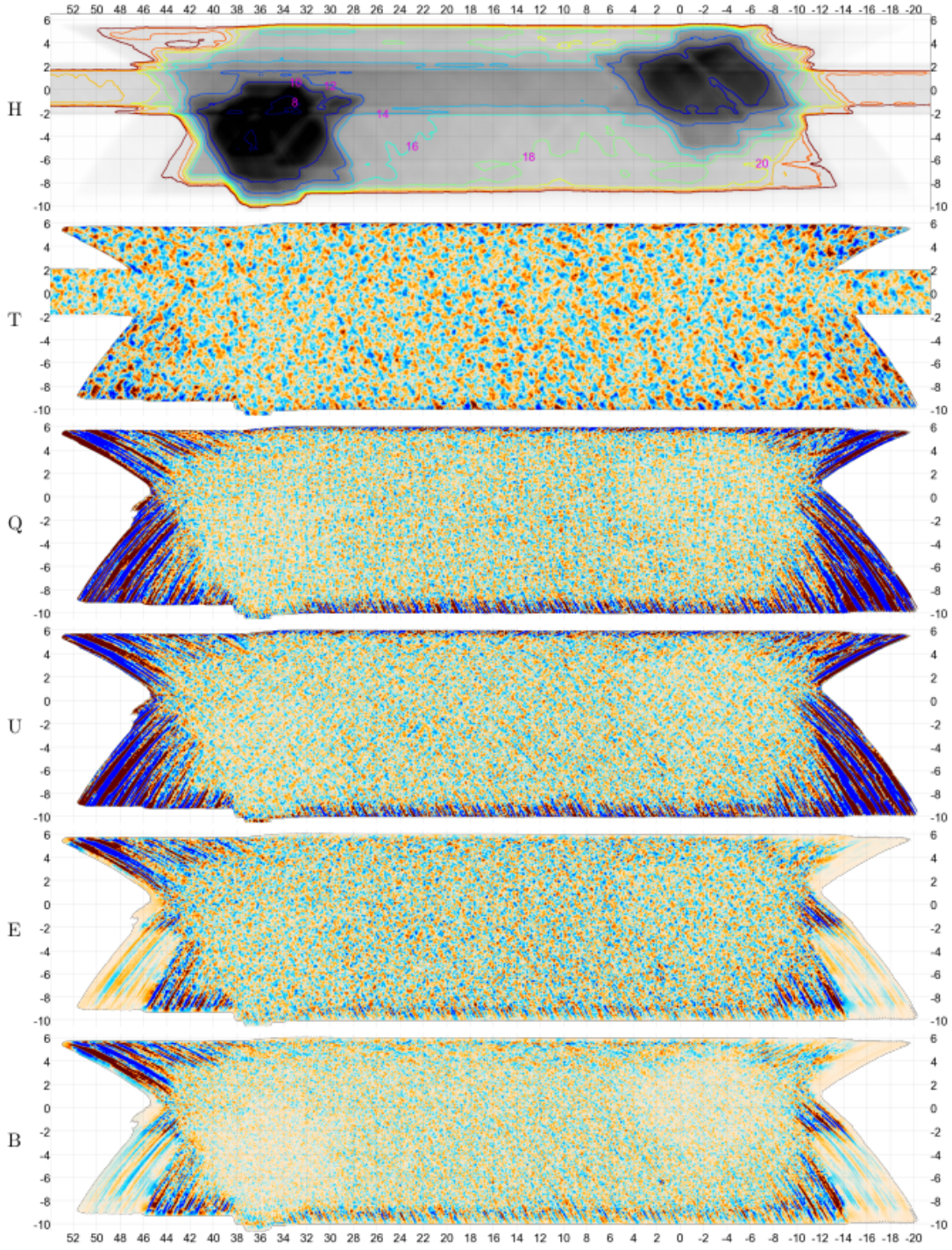

Figure 1.1: Maps of the CMB in temperature and polarization. The top panel is an exposure map. The panels below are the temperature, Q, U, E, and B polarizations. The maps are in equatorial coordinates, with the horizontal vertical axes in RA and Dec, respectively. Figure from [71].

from the diffusion of photons from hot and cold regions of space, resulting in a net polarization of the photons. This only occurs on small scales, as photons from further away hot and cold regions do not have time to meet before recombination completes. This means there will be a sharp drop off at large scales in the polarization power spectrum. At these large scales we find a peak in the power spectrum due to scattering during reionization. By measuring the polarization of the CMB we can learn more about the early universe than by just measuring the temperature alone [14].

In order to discuss the polarization of the CMB we must define some common terms used to describe the state of the polarization, namely the Stokes parameters. We introduce this by following along with Born and Wolf [12]. Start by considering a time-harmonic plane wave, with each Cartesian component of **E** and **H** of the form,

$$a\cos(\tau+\delta) = \mathrm{Re}\{ae^{-i(\tau+\delta)}\}, \tag{1.1}$$

where the amplitude, $a > 0$. The varying part of the phase is represented by τ, in general,

$$\tau = \omega t - \mathbf{k}\cdot\mathbf{r}, \tag{1.2}$$

where **k** is the wave vector and **r** is the position vector. We choose the z-axis be along the direction of propagation, often denoted **s**. We then consider the x and y components of **E**,

$$E_x = a_1\cos(\tau+\delta_1) \tag{1.3}$$

$$E_y = a_2\cos(\tau+\delta_2). \tag{1.4}$$

These equations can be rearranged in a more convenient form which describes the polarization ellipse,

$$\left(\frac{E_x}{a_1}\right)^2 + \left(\frac{E_y}{a_2}\right)^2 - 2\frac{E_x}{a_1}\frac{E_y}{a_2}\cos\delta = \sin^2\delta, \tag{1.5}$$

where

$$\delta = \delta_2 - \delta_1. \tag{1.6}$$

Since we expect the CMB to be linearly polarized we focus just on the special cases in which the polarization is said to be linear, namely if E_x or E_y is 0, or if,

$$\delta = m\pi \qquad (m = 0, \pm 1, \pm 2, \ldots). \tag{1.7}$$

We can parameterize the polarization state of a wave by the amplitudes, a_1 and a_2, and the phase difference, δ using the Stokes parameters,

$$s_0 = a_1^2 + a_2^2, \tag{1.8}$$

$$s_1 = a_1^2 - a_2^2, \tag{1.9}$$

$$s_2 = 2a_1 a_2 \cos\delta, \tag{1.10}$$

$$s_3 = 2a_1 a_2 \sin\delta. \tag{1.11}$$

While most reference texts use a variant of s_0, s_1, s_2, s_3 to describe the Stokes parameters, it is common in the field to see the Stokes vector written with parameters I, Q, U, V,

$$\vec{S} = \begin{pmatrix} s_0 \\ s_1 \\ s_2 \\ s_3 \end{pmatrix} = \begin{pmatrix} I \\ Q \\ U \\ V \end{pmatrix}, \tag{1.12}$$

a convention which we will follow throughout the remainder of this work. The Stokes parameters are related by the identity,

$$I^2 = Q^2 + U^2 + V^2. \tag{1.13}$$

These parameters can be physically interpreted as the intensity, I, amount of linear polarization, Q and U, and amount of circular polarization V. The polar-

ization angle, ϕ, of incoming polarized light is given by,

$$\phi = \frac{1}{2}\tan^{-1}\left(\frac{U}{Q}\right). \tag{1.14}$$

The fraction of linear polarization, L, is given by,

$$L = \sqrt{Q^2 + U^2}. \tag{1.15}$$

E and B Decomposition

The Stokes Q and U polarizations in the context of the CMB are typically decomposed into what are called E-mode and B-mode polarizations. This decomposition is a linear transformation of the Stokes Q-U field on the sky, the details of which have been written about thoroughly [107, 53, 108, 45, 106, 93]. Scalar perturbations (i.e. density fluctuations in the early universe) give rise to E mode polarization, while tensor perturbations (i.e. primordial gravitational waves) generate B mode polarization. These terms, E-mode and B-mode polarization, are a naming convention which arises from an analogy to the curl free and divergence free proprieties of electric and magnetic fields. A cartoon of these distinct polarization is shown in Figure 1.2.

The first detection of E-mode polarization was made using DASI [63]. This E-mode signature is about an order of magnitude smaller than the temperature signal. Primordial scalar perturbations can only generate E-modes, while primordial tensor perturbations can generate both E-modes, B-modes, and temperature anisotropies [52]. However, this is not the only source of B-modes; they can also be generated after decoupling. Gravitational lensing of E-mode polarization can mix E-modes into B-modes, causing a B-mode signature at large scales.

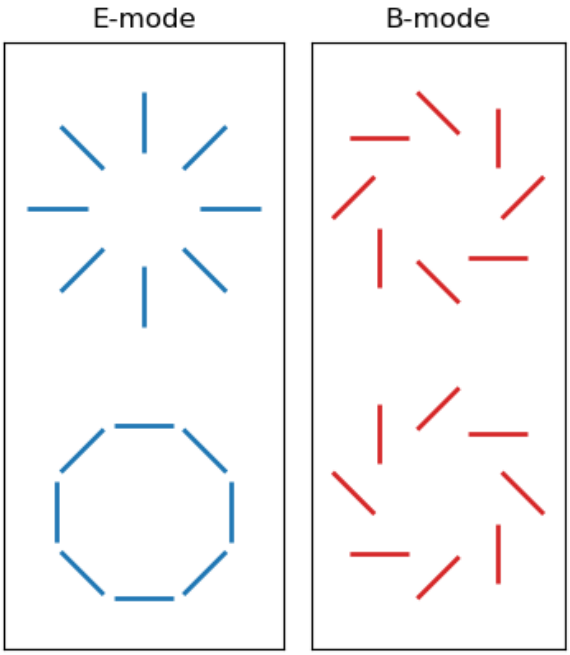

Figure 1.2: Diagram of E-mode and B-mode polarization.

The first detection of these lensing B-modes was made in 2013 by the South Pole Telescope (SPT), through combination with estimates for the lensing potential from the Herschel Space Observatory SPIRE instrument, which measures the Cosmic Infrared Background (CIB) [38]. The first direct detection was reported by the Polarbear Collaboration shortly after in 2014 [86]. If measured with high enough precision, this lensing information could be used to "de-lens" the B-mode power spectrum, to go after a measurement of the other cause of B-modes, primordial gravitational waves, the signature of inflation [75].

CMB temperature and polarization maps, like those shown in Figure 1.1, can be expanded in the spherical harmonics Y^X_{lm}. The covariances of the correspond-

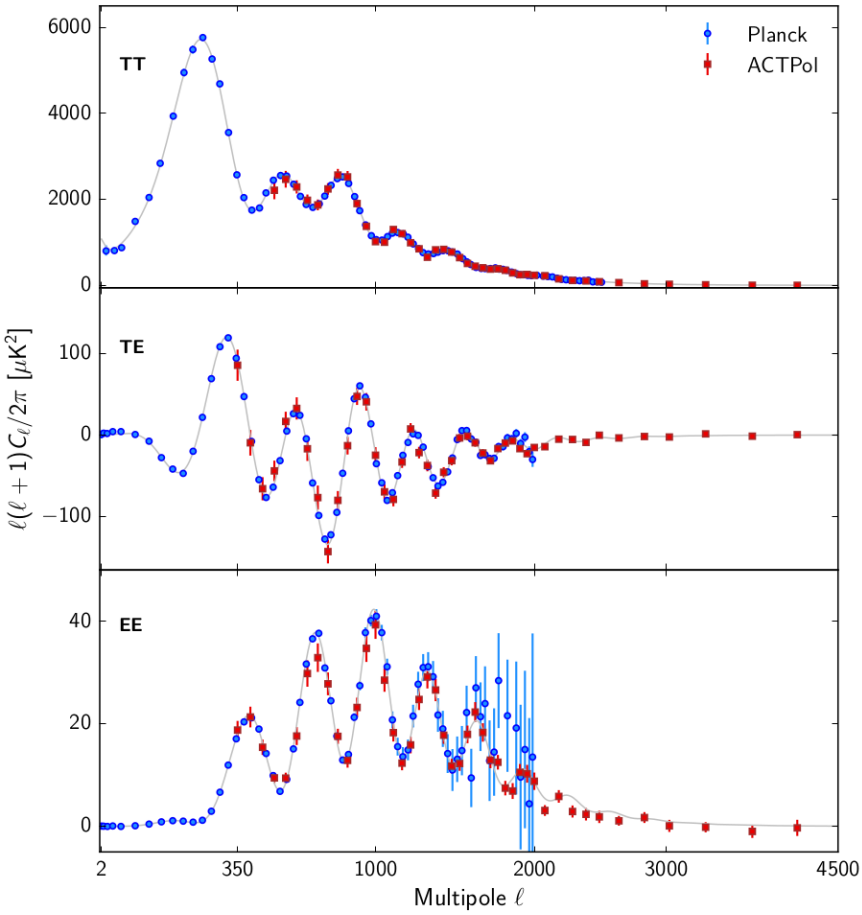

Figure 1.3: TT, TE, and EE cross correlation power spectra from [71].

ing expansion coefficients a^X_{lm} form the angular power spectra,

$$C_l^{XX}\delta_{ll'}\delta_{mm'} = \langle a^{X*}_{(lm)} a^X_{(l'm')} \rangle, \tag{1.16}$$

where XX can be any combination of T, E, or B (TT, EE, BB, TE, TB, EB) [53, 72, 54]. A comparison of the latest TT, TE, and EE power spectra from ACTPol and Planck are shown in Figure 1.3.

The amplitude of the B-mode signal is encoded in the tensor-to-scalar ratio, r. The measure of this amplitude, whether directly or after de-lensing, would directly measure the expansion rate of the Universe during inflation [2]. Currently

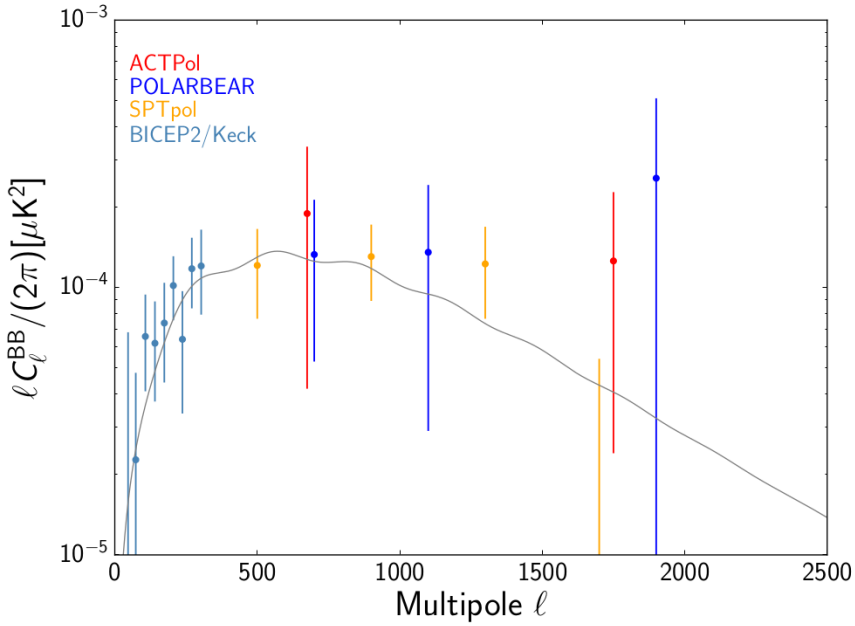

Figure 1.4: BB autocorrelation spectra from ACTPol and other projects. The solid line is the Planck best fit ΛCDM model. Figure from [71].

the best constraints on r come from a combination of data from BICEP/KECK and Planck and yield a limit of $r_{0.02} < 0.064$ at 95% confidence, where the subscript on r is the pivot scale for the spectral index of the power spectrum in units of Mpc^{-1} [85]. The latest BB power spectra from ACTPol plotted with data from POLARBEAR, SPTpol, and BICEP2/Keck is shown in Figure 1.4.

Measurement of r requires careful polarization calibration and consideration of foregrounds. A miscalibration of the detector angles generates a spurious r signal. A rotation of 0.5° can generate a signal of 0.002 [3]. Foregrounds, such as polarized dust in our galaxy, can also cause a spurious r signal. Other generators of false B-mode power include instrument polarization, which we will discuss in Chapter 3, and cosmic polarization rotation.

1.2 Cosmic Polarization Rotation

1.2.1 A History of Cosmic Polarization Rotation

Cosmic polarization rotation (CPR), also referred to as 'cosmological birefringence', is the rotation of linearly polarized light as it traverses empty space at cosmological scales [72, 15]. The search for a non-zero CPR is a test for CPT-violating physics and has been probed across the electromagnetic spectrum with observations of polarized radio and UV emission from galaxies, polarized gamma ray bursts and the cosmic microwave background (CMB) polarization signal [15, 67, 99, 36, 60].

The theory behind CPR has its origin in a counter example to Schiff's conjecture that any theory of gravity that obeys the weak equivalence principle (WEP) must also obey the Einstein equivalence principle (EEP). This counter was developed by Wei-Tou Ni in 1973 and coupled electromagnetism and gravity and resulted in a modified electromagnetic theory with a differing dispersion relation for right and left circularly polarized waves. This theory obeys the WEP, but violates parity and time-reversal invariance [1].

It was not until 1990 that this theory was used to put upper limits on these Lorentz invariance and parity violating modifications to electrodynamics by Carroll, Field and Jackiw [16]. Carroll et al. presents the theory as a modification to the electromagnetic Maxwell Lagrangian by the addition of a Chern-Simons term which ultimately violates Lorentz-invariance and CPT-symmetry. To place these upper limits they compiled polarization measurements from 160 different radio galaxies. They compared these polarization measurements to models for

the polarized synchrotron radiation emission angle. These models predict an emission parallel or sometimes perpendicular to the extended radio galaxies.

Since this first upper limit was placed there have been searches for a non-zero CPR across many wavelengths, using radio galaxies, UV emission from distant radio galaxies, hard X-rays, gamma ray bursts, and CMB polarization observations. CMB polarization observations now put the tightest constraints on CPR. And while the most popular models for CPR are wavelength independent, allowing the subtraction of other effects such as Faraday rotation (which goes as λ^2), some models include an energy dependence, making observations of high energy sources such as GRBs an important tool for testing alternative CPR models.

1.2.2 A Modification to Electrodynamics

We start with the standard electromagnetic Maxwell Lagrangian in Equation (1.17),

$$\mathcal{L}_{EM} = -\frac{1}{4} F_{\alpha\beta} F^{\alpha\beta}, \tag{1.17}$$

where $F^{\alpha\beta}$ is the electromagnetic field-strength tensor, $F^{\alpha\beta} = \partial^\alpha A^\beta - \partial^\beta A^\alpha$, and A^α is the electromagnetic four-vector potential. To this, following Carroll and Field, we add the Chern-Simons term,

$$\mathcal{L}_{CS} = -\frac{1}{2} p_\alpha A_\beta \tilde{F}^{\alpha\beta}, \tag{1.18}$$

where $\tilde{F}^{\alpha\beta}$ is the dual field-strength tensor, $\tilde{F}^{\alpha\beta} = \frac{1}{2}\epsilon^{\alpha\beta\mu\nu} F_{\mu\nu}$, and p_α is a coupling four-vector [16]. This results in the Lagrangian given here in Equation (1.19),

$$\mathcal{L} = -\frac{1}{4} F_{\alpha\beta} F^{\alpha\beta} - \frac{1}{2} p_\alpha A_\beta \tilde{F}^{\alpha\beta}, \tag{1.19}$$

It is this coupling term, p_α, which violates rotational invariance and invariance under a Lorentz boost. Applying the gauge transformation $A_\nu \to A_\nu + \partial_\nu \chi$, written as $\Delta A_\nu = \partial_\nu \chi$ to follow the convention in Carroll et al., we obtain the variation $\Delta \mathcal{L}_{CS}$,

$$\Delta \mathcal{L}_{CS} = \frac{1}{4} \tilde{F}^{\beta\alpha} \left(\partial_\alpha p_\beta - \partial_\beta p_\alpha \right). \tag{1.20}$$

In Minkowski space $\partial_\alpha p_\beta = 0$, making $\Delta \mathcal{L}_{CS} = 0$, meaning it is gauge invariant. This implies a constant p_α, which picks out a preferred direction in space-time. The spacial component of p_α violates rotational invariance, while the time component of p_α violates invariance under a Lorentz boost [16].

The effect of this additional Chern-Simons term in the Lagrangian is to modify the four-current,

$$J^\beta \to J^\beta + p_\alpha \tilde{F}^{\alpha\beta} / 4\pi. \tag{1.21}$$

This results in the following modified field equations,

$$\nabla \cdot \mathbf{E} = 4\pi\rho - \mathbf{p} \cdot \mathbf{B}, \tag{1.22}$$

$$\nabla \cdot \mathbf{B} = 0, \tag{1.23}$$

$$\nabla \times \mathbf{E} = -\frac{\partial \mathbf{B}}{\partial t}, \tag{1.24}$$

$$\nabla \times \mathbf{B} = \frac{\partial \mathbf{E}}{\partial t} + 4\pi \mathbf{J} - p_0 \mathbf{B} + \mathbf{p} \times \mathbf{E}. \tag{1.25}$$

These, of course, reduce to Maxwell's equations when the coupling term, p_α, is zero. Working from these modified field equations and following the usual steps of taking the curl of Equations (1.24) and (1.25) and substituting in appro-

priately while considering solutions of the form $\mathbf{E} = E_0 e^{i(\mathbf{kr}-\omega t)}$, we obtain the modified dispersion relation,

$$\omega^2 - k^2 = \pm (p_0 k - \omega p \cos\theta) \left(1 - \frac{p^2 \sin^2\theta}{\omega^2 - k^2}\right)^{-1/2}. \tag{1.26}$$

Equation (1.26) describes both right-handed and left-handed circularly polarized waves with the $+$ and $-$, respectively. θ corresponds to the angle between $\mathbf{p}$, the spatial part of the coupling four-vector p_α, and the wave vector $\mathbf{k}$.

The coupling four-vector, p_α, is expected to be small, allowing us to Taylor expand in powers of p_α to first order,

$$k = \omega \mp \frac{1}{2}(p_0 - p\cos\theta) \tag{1.27}$$

We know the CMB photons are linearly polarized, as they are produced by Thompson scattering. We can express a linearly polarized wave as a linear combination of two circularly polarized waves, one left-circular polarized and one right-circular polarized. In the most general form the left and right circularly polarized components take the form,

$$E_x = E_x^0 e^{i(kz-\omega t+\alpha)}, \tag{1.28}$$

$$E_y = E_y^0 e^{i(kz-\omega t+\beta)}, \tag{1.29}$$

where the sign of E_y would identify the wave as left-circular $(+)$ or right-circular $(-)$ polarization as viewed looking at the incoming wave. The sum of these two circularly polarized wave descriptions results in a linearly polarized wave.

In our case, the dispersion relation, Equation (1.27), differs for the two circularly polarized waves, and as the wave propagates a distance L the phase changes by $\phi = kL$, causing the polarization vector to rotate by,

$$\Delta\phi = \frac{1}{2}\left(\phi_L - \phi_R\right) = -\frac{1}{2}\left(p_0 - p\cos\theta\right)L. \tag{1.30}$$

This angle, $\Delta\phi$, is what we want to measure, this is the cosmic polarization rotation [16].

1.2.3 CPT Symmetry

The CPT theorem (also referred to in the literature as the TCP theorem) states that "the combined operation of time reversal (T), charge conjugation (C), and parity (P) (in any order) is an exact symmetry of any interaction." CPT symmetry is often thought of in the context of particle physics, specifically in the test that every particle should have an identical mass and lifetime as its antiparticle. A well tested example is a comparison of the mass of the K^0 and $\overline{K}^0$ [35].

In the context of our modified Chern-Simons Lagrangian and its resulting term p_α, which couples to electromagnetic fields, it is the coupling which picks out a preferred direction in spacetime and violates CPT symmetry [16]. A measurement of a non-zero cosmic polarization rotation would be the first measured violation of CPT symmetry [54].

1.2.4 Cosmological Constraints on CPT Symmetry

As described in Section 1.2.1, we can search for a non-zero CPR to test CPT Symmetry across the electromagnetic spectrum. In this section I focus on constraints from CMB observations.

The best constraints on CPR today come from observations of the polarization of the cosmic microwave background (CMB). The CMB can be used to put constraints on CPR through the cross-correlation power spectra. The distribution of inhomeogeneities in the CMB are required to be invariant under parity and since Y^T_{lm} and Y^E_{lm} have parity $(-1)^l$ and Y^B_{lm} has parity $(-1)^{l+1}$ we expect $C_l^{TB} = 0$ and $C_l^{EB} = 0$ [53].

This expectation is useful in measuring the CPR angle, α. A non-zero CPR would cause a mixing of E-modes into B-modes, resulting in non-zero EB and TB cross-correlation power spectra [54]. The amount of mixing caused by a CPR rotation, α, is given as [72, 43, 57],

$$C_l'^{TE} = \cos(2\alpha)\, C_l^{TE}, \tag{1.31}$$

$$C_l'^{EE} = \sin^2(2\alpha)\, C_l^{BB} + \cos^2(2\alpha)\, C_l^{EE}, \tag{1.32}$$

$$C_l'^{EB} = \frac{1}{2}\sin(4\alpha)\left(C_l^{BB} - C_l^{EE}\right), \tag{1.33}$$

$$C_l'^{TB} = -\sin(2\alpha)\, C_l^{TE}, \tag{1.34}$$

$$C_l'^{BB} = \cos^2(2\alpha)\, C_l^{BB} + \sin^2(2\alpha)\, C_l^{EE}. \tag{1.35}$$

Here the primes on the left side indicate the observed, rotated, power spectra. The non-primed terms give the original, unrotated, quantities. Looking at

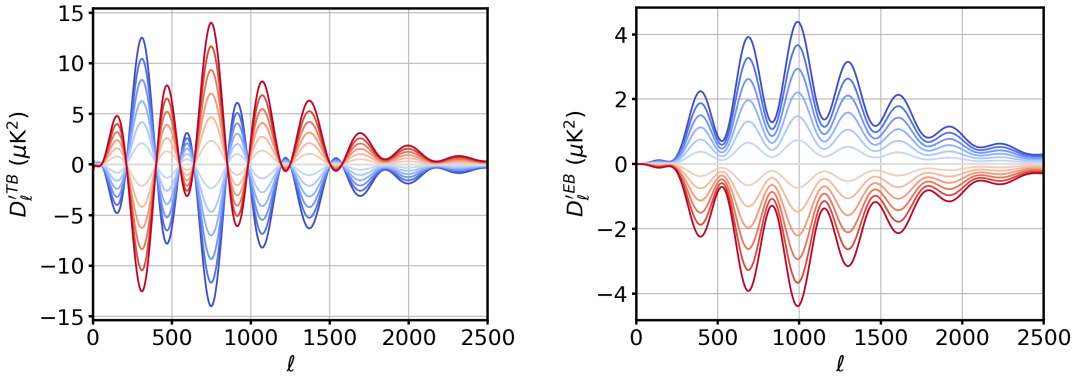

Figure 1.5: Demonstration of the effect of polarization rotation on the best fit ΛCDM model power spectra from the Planck 2015 results [84]. A polarization rotation is applied, ranging from $-3°$ to $3°$, blue to red, in increments of $0.5°$.

Equations (1.33) and (1.34), we see that a non-zero EB and TB power spectrum can result from a mixing of E into B modes.

Any miscalibration in the detector angles of an experiment is degenerate with a non-zero CPR. As a result, current constraints on α are limited by the systematic error associated with calibrating the polarization angle of the detectors. Current polarization techniques limit the angular resolution to roughly $\pm 0.5°$ [55]. In addition, using the assumption that $C_l^{\prime TB}$ and $C_l^{\prime EB} = 0$ to determine the calibration angle eliminates the ability to measure a DC CPR.

Figure 1.5 shows the effect of cosmic polarization rotation (or an angle miscalibration) on the standard ΛCDM TB and EB power spectra as described by Equations (1.31)-(1.35). This plot uses the best-fit ΛCDM model from the Planck 2015 results paper as the appropriate idealized C_ℓ^{XX} from Equations (1.33) and (1.34) [84]. The latest measured TB and EB power spectra from ACTPol are shown in Figure 1.6, and have an offset angle consistent with zero [71].

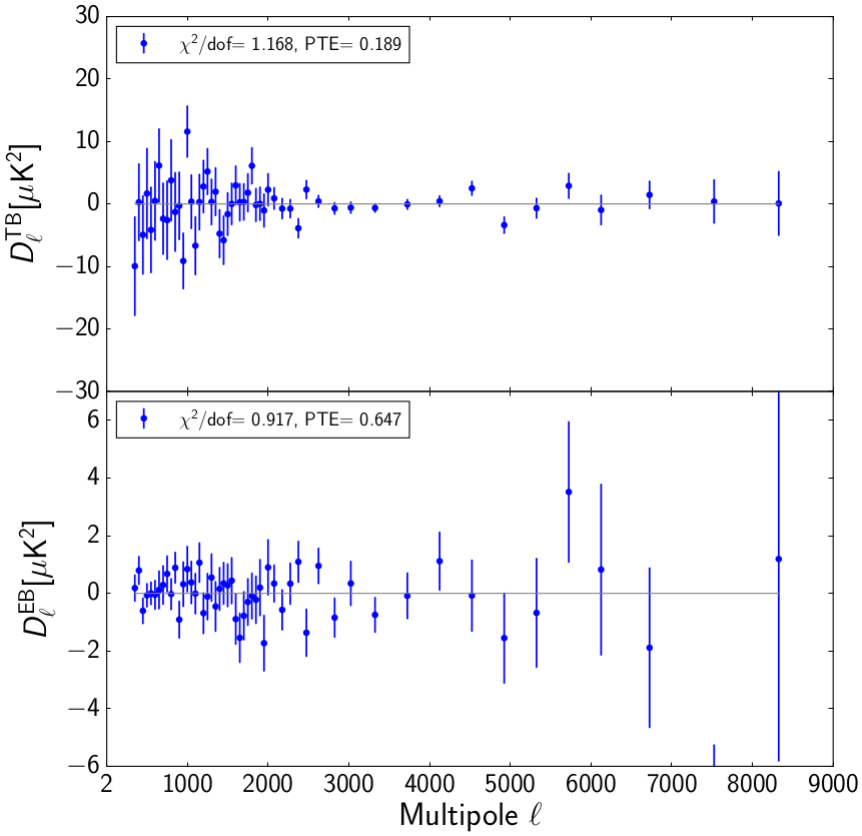

Figure 1.6: The latest TB and EB cross correlation power spectra from ACTPol. Figure from [71].

Constraints from Different CMB Experiments

To search for a non-zero CPR we must then measure the CMB temperature and polarization power spectra. Table 1.1 summarizes constraints from many of the CMB polarization experiments, both from the original teams who deployed the instruments as well as from external data analysts.

Since detector angle calibration is degenerate with CPR constraints, improvements in the angular resolution with which we can calibrate detectors decrease the systematic errors on constraints on α. For this reason we have

Experiment/Dataset	Frequency (GHz)	α [deg]	Year
WMAP + BOOMERANG	-	$-6.2^{+4.0\,+3.9}_{-4.0\,-3.7}$	2006 [28]
WMAP3 + BOOMERANG	-	-6.2 ± 4.0	2008 [103]
WMAP5 + BOOMERANG	-	-2.6 ± 1.9	2008 [104]
BOOMERANG	143	-4.3 ± 4.1	2009 [54]
QUaD	$100 + 150$	$0.55 \pm 0.82 \pm 0.5$	2009 [102]
WMAP7	$41 + 61 + 94$	$-1.1 \pm 1.4 \pm 1.5$	2010 [60, 54]
BICEP1 - DSC	$100 + 150$	$-2.77 \pm 0.86 \pm 1.3$	2013 [56]
BICEP1 - Near Grid	$100 + 150$	-1.91 ± 0.86	2013 [56]
BICEP1 - Far Grid	$100 + 150$	-1.71 ± 0.86	2013 [56]
BICEP1 - As-Designed	$100 + 150$	-1.27 ± 0.86	2013 [56]
POLARBEAR	150	$-1.08 \pm 0.20 \pm 0.5$	2014 [54, 94]
BICEP2	150	-1 ± 0.2	2014 [54, 4]
ACTPol	146	-0.2 ± 0.5	2014 [54, 76]

Table 1.1: Summary of constraints on CPR angle, α, by various CMB experiments. Uncertainties are listed with statistical followed by systematic uncertainties when available. (Note the BICEP2 constraint is derived from a combination of the EB-nulling angle and relative detector angle measurements, the systematic uncertainty is not reported.)

included constraints obtained from applying different calibration techniques in the BICEP1 experiment, which has provided great detail about their calibration methods [56]. Since angle calibration is the limiting factor in our ability to extract a CPR angle from CMB polarization data, a critical step in advancing these constraints is improving our current calibration techniques.

There are several ways to calibrate detector angles. The wide range of techniques provides value in the ability to cross-check the calibration between techniques. One method for calibrating detector angles is referred to as "self-calibration" or "EB-nulling". Since we expect a zero EB cross correlation power spectrum, we can take the global rotation angle which nulls the EB power spectrum signal as our calibration angle. This technique is attractive, it does not take

time away from observing, requires no extra hardware, and is applicable to any polarimeter, however, if there is a uniform, non-zero, CPR you lose that information [57]. It can also introduce additional rotation if there is unaccounted for polarized foregrounds, such as polarized dust, which can make EB and TB non-zero.

Other techniques include observing polarized sources, both man-made and astrophysical. Observing a modulated source allows for the extraction of the angles for the detectors from the phase and amplitude of each detector's response. We can also calibrate to previous measurements by observing a well characterized astrophysical source. The best constraints from CMB experiments use a combination of these techniques to cross-check their calibrations. Current limits on the best constraints come from uncertainties in the measurement of these man-made and astrophysical sources. These constraints are from BICEP2 with $\alpha \approx -1 \pm 0.2^\circ$ statistical (systematic uncertainty yet to be published), POLARBEAR with $\alpha = -1.08^\circ \pm 0.20^\circ$ statistical with a $\pm 0.5^\circ$ systematic and ACTPol with $\alpha = -0.2 \pm 0.5^\circ$ systematic [54].

CMB observations currently provide the best constraints on CPR and will likely continue to lead in this test of CPT violating physics on cosmological scales. The best constraints are currently limited by the uncertainty in polarization calibration techniques. We discuss the ACTPol calibration Chapter 3 and recent observations of Tau A with ACTPol in Chapter 5. Other experiments such as ALMA could improve the precision of the polarization measurements on Tau A, reducing current systematic errors and improving these constraints. Further improvements will come in the form of better detector angle calibration.

A measurement of a non-zero cosmic polarization rotation would be a

ground breaking discovery, since it would violate the CPT Theorem. However, current cosmological constraints on CPT violating CPR are consistent with zero. Measurements of the CMB provide the tightest constraints and appear to hold the most promise for improvement in the near future. Improvements in calibrating CMB detectors will continue to push these constraints lower and are a strong motivation for improving calibration techniques like those discussed in this thesis.

1.3 Overview

This thesis focuses on the polarization angle calibration for ACTPol and Advanced ACT, and includes an overview of the Advanced ACT upgrade as well as details on various subsystems, including those required to remotely control the telescope.

In Chapter 2 an overview of the AdvACT instrument is given. Details about the iterative testing of prototype transition edge sensors to tune the detector parameters are presented for each of the AdvACT frequency ranges.

In Chapter 3 the optical modeling of instrumental polarization generated by the ACTPol optical chain is presented. This plays a critical role in the calibration of the ACTPol and AdvACT CMB measurements. Each step of this calibration process is discussed and the final calibration for each detector is shown, with parameters available for reproducing the modeled polarization rotation for each existing ACT array.

In Chapter 4 the design and use of several polarization grids is presented.

These are used to cross check the modeling from Chapter 3 by measuring the polarization rotation caused by the ACTPol optics.

In Chapter 5 maps of the polarized source, Tau A, are presented for the first three seasons of ACTPol observations. The source is mapped in each detector array independently, and the effect of removing the optical modeling component of the polarization calibration is observed.

In Chapter 6 the telescope computing systems and remote observation procedure are presented. The control systems that keep the telescope running comprise a complicated network of independent systems, which must be remotely serviceable for fault resolution. Monitoring these systems and the data they collect is critical to the ACT project.

In Chapter 7 we summarize with some concluding remarks and discuss this work in the context of upcoming experiments.

CHAPTER 2

ADVANCED ACTPOL INSTRUMENTATION

The Atacama Cosmology Telescope has been used for three generations of observations over the years since it was built. Originally constructed in 2007, the first ACT camera was upgraded to the Atacama Cosmology Telescope Polarimeter (ACTPol) in 2013. Then, in 2016 the upgrade to what is known as Advanced ACTPol (AdvACT) began. Today, AdvACT is fully deployed and observations have been underway for more than two full seasons.

In this chapter we discuss the AdvACT hardware. We start, in Section 2.1, by reviewing the Atacama Cosmology Telescope Polarimeter and the components within it. Next, in Section 2.1.1, we review the upgrade to AdvACT. In Sections 2.1.2 and 2.1.3 we briefly discuss the detector readout and observing strategy. Section 2.2 focuses on the testing of prototype AdvACT detectors which informed the fabrication of the final detector arrays. We close with Section 2.3, which provides an overview of the AdvACT near receiver baffle and its utility in reducing background loading and protecting the fragile metamaterial half-wave plates and their associated electronics.

2.1 The Atacama Cosmology Telescope Polarimeter

The Atacama Cosmology Telescope (ACT), shown in Figure 2.1, is an off-axis Gregorian telescope constructed in 2007 [30]. Originally designed to measure the temperature of the CMB only, ACT observed with the Millimeter Bolometer Array Camera (MBAC) [92] until it was upgraded with the Atacama Cosmology Telescope Polarimeter (ACTPol) [95] camera in 2013. ACTPol is a polarization

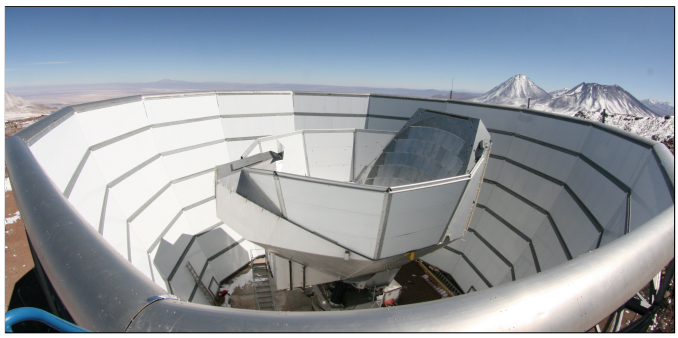

Figure 2.1: A photo of the Atacama Cosmology Telescope, courtesy of Mark Devlin. The outer panels, over which the photo is taken, form the 13 m tall ground screen. In the center of the ground screen sits the telescope, with attached co-moving ground screen. Part of the 6 m primary mirror is visible.

sensitive receiver upgrade to ACT, introducing polarization sensitivity to the instrument with three kilo-pixel scale arrays. Two of these arrays (referred to as PA1 and PA2, PA for 'polarization array') were designed for observation at 150 GHz [26]. The third, the first multichroic array of its kind, was designed to observe at both 90 and 150 GHz simultaneously [20, 44].

The primary elements of the ACTPol optical chain are a 6 m primary mirror, a 2 m secondary mirror and three optics tubes, each of which contains a set of three silicon reimaging lenses. Silicon is used due to its high index of refraction. However, without an anti-reflection coating, this would lead to a $\sim$30% loss due to reflections at each vacuum/silicon interface. A metamaterial anti-reflection coating is used to reduce these reflections to less than 1%. These coatings are fabricated using a silicon dicing saw to remove silicon, leaving pillars, reducing the effective index of refraction of each layer based on the amount of silicon removed [21, 18]. A schematic of a coating, along with its reflectance as a function of frequency, is shown in Figure 2.2. Other elements include the receiver window, several band defining filters and a set of corrugated feedhorns per array.

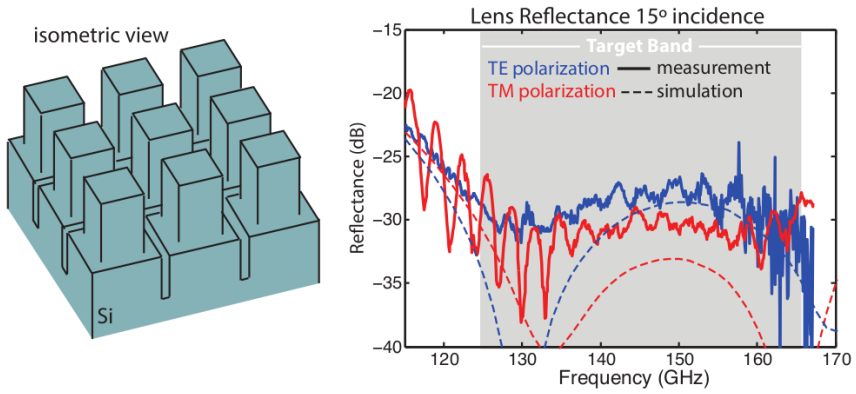

Figure 2.2: (Left): Isometric view of the anti-reflection coating used on the single frequency ACTPol lenses. This example shows a two-layer coating, like those used on the ACTPol PA1 and PA2 optics. (Right): A comparison of measurements and simulations of the reflectance as a function of frequency for the ACTPol two-layer AR coating design. Figure from [95].

Figure 2.3 shows the optical chain with a simple ray trace for one optics tube.

All of these components, except for the primary and secondary mirrors, are housed within a cryogenic receiver, pictured in Figure 2.4. The receiver, in addition to containing all of cold optical components, houses the He3/He4 dilution refrigerator. The fridge is backed by a pulse tube cooler, specifically a PT407, which assists in cooling the lower stages, close to the detector arrays. A single PT410 is responsible for cooling the optics and associated structures at 40K and 4K. This allows for continuous operation of the detectors at 100 mK [95].

The final element before the detectors themselves is the corrugated feedhorns [89]. Each feedhorn couples to an orthomode transducer (OMT) which separates incoming light into orthogonal polarizations. The angle of the two OMT fins are defined by lithography in fabrication. This angle will form the first input to the polarization calibration described in Chapter 3. The ACTPol detec-

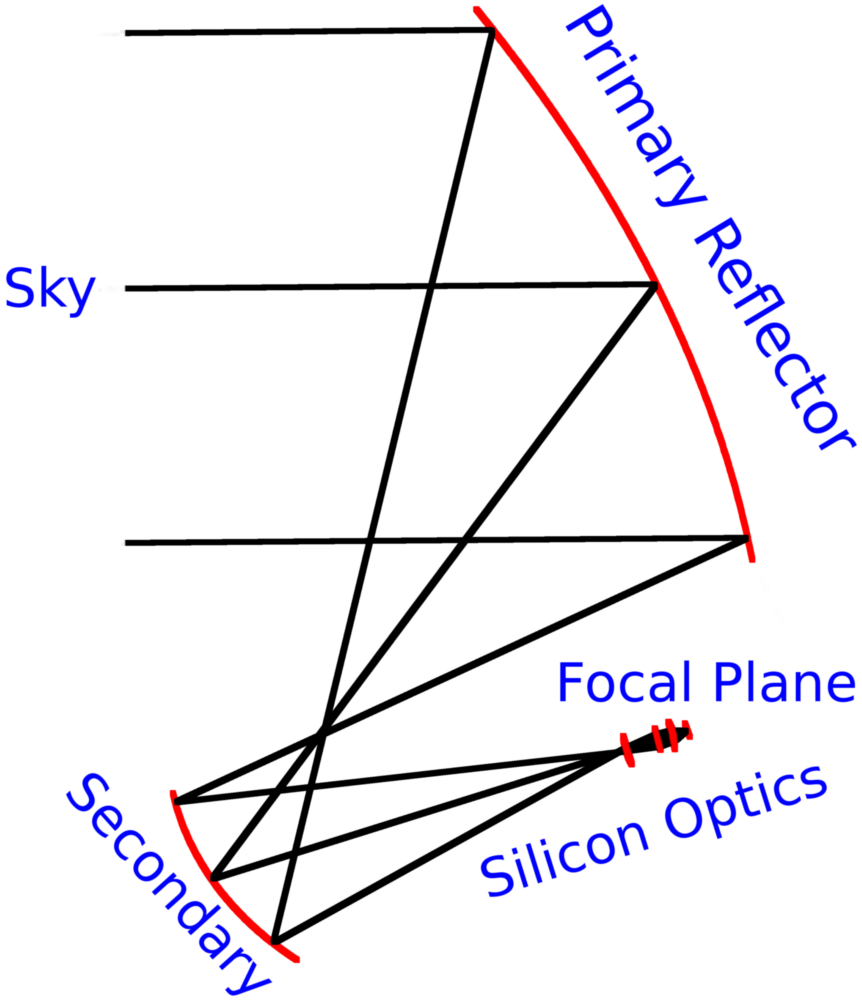

Figure 2.3: Single field ray trace of the ACTPol optics. This represents a simple, single ray, trace of the ACTPol optical chain in CODE V. A single field point on the sky is propagated first to the primary reflector, then to the secondary reflector, and through three silicon reimaging optics to the detector focal plane. Figure from [61].

tors are fabricated on 75 mm diameter wafers which were etched into hexagonal and partial hexagonal shapes (referred to as "hexes" and "semi-hexes") and tiled in an array of three hexes and three semi-hexes each. A single "hex" wafer is shown in Figure 2.4. The orthogonal antenna probes on each wafer are oriented at 0/90 degrees and 45/135 degrees, such that the full array of six wafers has sets of detectors ranging from 0 to 180 degrees at 15 degree intervals. A fully assembled array is shown in Figure 2.5.

Figure 2.4 also shows detailed photos of a single ACTPol pixel, including the OMTs and TESes. The last detailed photo shows a single TES, with the detector in the center, surrounded by the lossy gold meander, in which the power coupling to the OMTs is deposited as heat. This is what ultimately heats up the TES, which we see as a change in resistance. The SiN legs serve two purposes, one is to hold the Nb lines which bring the signals to and from the TES, and the other is to provide a weak thermal coupling to the 100 mK bath.

2.1.1 The Advanced ACTPol Upgrade

ACTPol was innovative with many of the hardware upgrades. The continually operating dilution fridge lowered the bath temperature when compared to other fridge technologies used in the field and allowed for 24 hour a day observations. The third array, PA3, was the first multichroic TES detector array of its kind, setting the stage for what would become the norm on future experiments, including the next set of upgrades on ACT.

Beginning in 2016, ACTPol began to be upgraded to what is known as Advanced ACTPol. The upgrade replaces each array in ACTPol with a new ar-

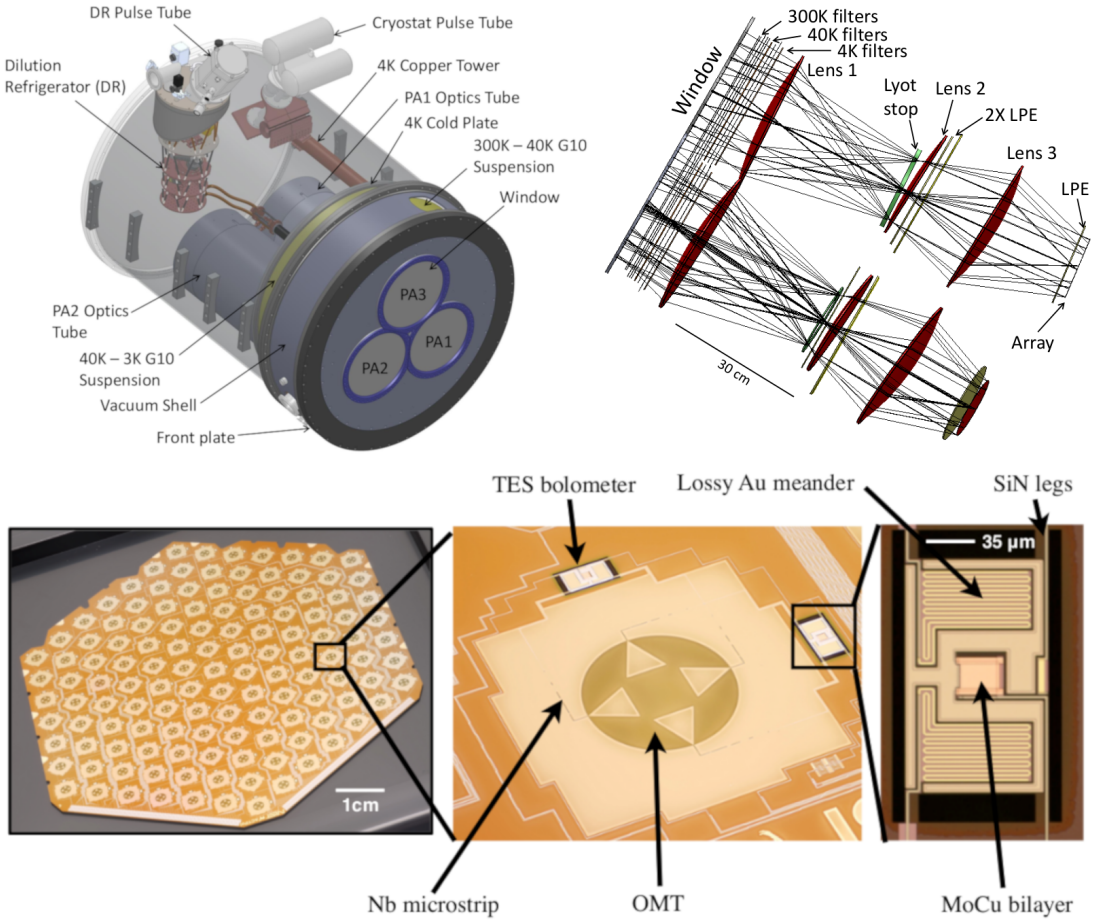

Figure 2.4: ACTPol optics and detector components. (Top Left): A CAD model of the ACTPol receiver. The length is 1.5m. The PA3 optics tube and the outer shell have been removed to show more of the internal components. (Top Right): A ray trace of the three optics tubes. The top optical path is the PA3 optics tube, while the bottom one is the PA1 optics tube. PA2 components are located behind the PA1 optics tube in this view. (Bottom): A single 148 GHz ACTPol detector 'hex' wafer containing 127 pixels and 254 TESes. Each array contains three of these wafers, along with three 'semi-hex' wafers. Each zoom in shows the consistent components, and is described in the text. All figures from [95].

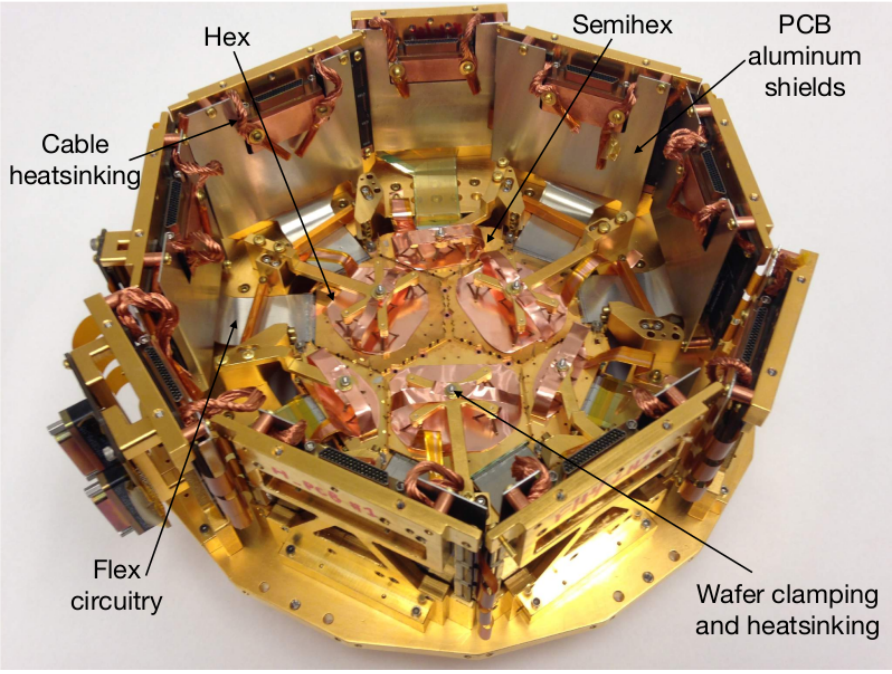

Figure 2.5: The fully assembled ACTPol PA2 array. This photo is taken from the back side of the array, with the feedhorn apertures pointed down at the table. The three hex and three semi-hex wafers make up the focal plane, with wafer clamping and heatsinking holding the wafers in place and providing a conduction path to cool the detector wafers. The cold readout components are connected via flexible circuitry, and are housed on PCBs that stand vertically behind the array. Figure from [95].

ray, fabricated on a single 150 mm wafer [24]. AdvACT expands the frequency range covered by ACTPol, from 90 and 150 GHz to cover 27, 39, 90, 150, and 230 GHz. This is achieved across four separate arrays, all multi-chroic, like the 90/150 GHz array from ACTPol. These are divided into the high-frequency (HF) array, observing at 150 GHz and 230 GHz [105, 90, 59], two mid-frequency (MF) arrays, observing at 90 and 150 GHz [17], and a low-frequency (LF) array, observing at 27 and 39 GHz [91].

Single frequency observations of the CMB are limited by foregrounds such

as synchrotron, spinning dust emission, galactic dust, and dusty star forming galaxies. AdvACT's high and low frequency coverage allows for the removal of these foregrounds, with the low frequency coverage aiding in the removal of synchrotron and spinning dust emission. The wide frequency coverage (27-230 GHz) and fine angular resolution ($1.4'$ at 150 GHz) of AdvACT will enable a wide range of science such as improving constraints on dark energy, the sum of the neutrino masses, and the existence of primordial gravitational waves [39].

The AdvACT deployment is, much like ACTPol was, a staged process, integrating a new array after a thorough development and testing process. This process begins with the fabrication of prototype transition edge sensors and single pixels. These prototypes are then tested in the lab to measure their properties, such as their critical temperature, thermal conductivity, saturation power, and more. Feedback based on the results of this testing is provided to the fabrication team, physical parameters in the detectors are adjusted and the final array is fabricated. The detector arrays are fabricated on monolithic 150mm wafers, allowing for higher pixel packing density than the tiled focal planes of ACTPol. The detector array is assembled with its readout electronics connected to the detectors via superconducting flexible circuitry [79] into an array package and installed into the ACTPol receiver [51]. A photo of the AdvACT HF array is shown on the right of Figure 2.6.

Each polarization array has been given sequential numbers and is usually referred to, in the case of say the first array, as either pa1 or ar1, or "polarization array 1" or "array 1". This nomenclature will be used throughout. ACTPol deployed arrays 1-3, while AdvACT has so far deployed arrays 4-6.

The deployment of AdvACT began in 2016 with the installation of the HF

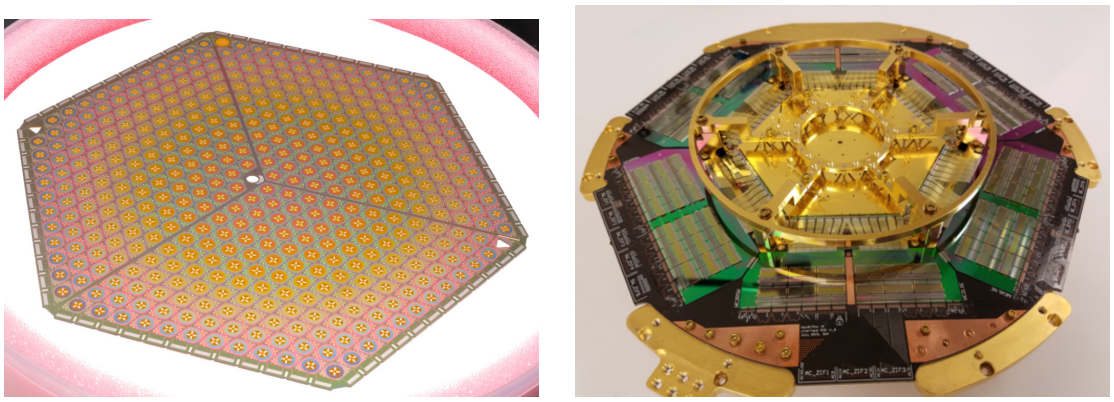

Figure 2.6: (Left): An AdvACT MF array detector wafer. Photo courtesy of the NIST Quantum Sensors group. (Right): The assembled AdvACT HF array as viewed from the backside.

array (pa4), which replaced the first ACTPol array (pa1). In 2017, the remaining ACTPol arrays were replaced by the two AdvACT MF arrays. The LF array is complete, but not on the sky. It will replace one of the MF arrays when deployed in early 2019.

In addition to new detector arrays, for AdvACT we have been developing a set of three rapidly rotating half-wave plates (HWPs). These rotate at $\sim$2 Hz, modulating the incoming polarization at $\sim$8 Hz. This should allow for reduction of low frequency atmospheric noise, and has been demonstrated to work on the Atacama B-mode Search (ABS) using a sapphire HWP, which suppressed atmospheric noise by a factor of more than 500 with less than 0.1% leakage from intensity to polarization [66, 65]. The AdvACT HWPs are ambient temperature metamaterial silicon HWPs. These are constructed from several layers of silicon wafers that have machined grooves. When stacked together these wafers behave as an achromatic, birefringent material, which should have lower loss then a sapphire HWP, as they are approximately twice as birefringent [39]. We discuss HWP loss in more detail in Section 2.3.1. A photo of all three silicon

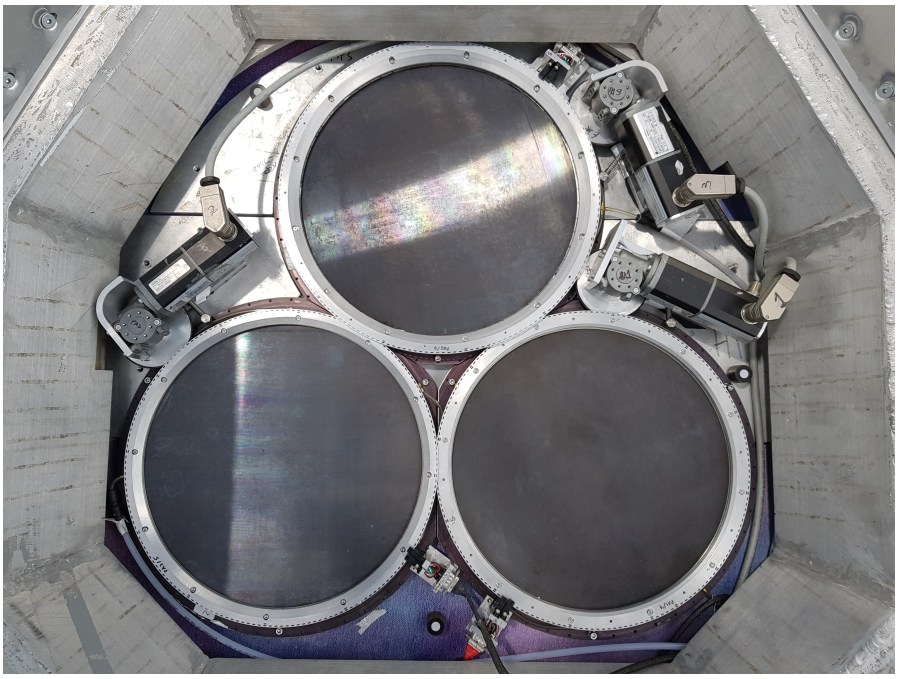

Figure 2.7: All three silicon metamaterial HWPs deployed on AdvACT. The HWPs sit on an air bearing and are spun by nearby motors at $\sim$2 Hz. The angular position of each HWP is readout by an optical encoder. Photo courtesy of Felipe Carrero.

HWPs deployed on AdvACT is shown in Figure 2.7.

As of this writing the three HWPs are not deployed on AdvACT. They were deployed for a two week test period in October of 2017. This should provide enough data to make maps of relatively small areas of equivalent depth to those made from the first season of ACTPol. This small data set will allow us to study potential systematics introduced by the HWPs before collecting entire seasons of data with them deployed.

2.1.2 Readout

Given the large number of detectors in the ACTPol and AdvACT focal planes, it becomes impracticable to run wires individually to each detector from room temperature. This alone would cause the focal plane to not reach base temperature. To reduce the number of wires required to read out the entire array we use a type of multiplexing called time division multiplexing (TDM). This enables the readout of many more detectors than there are readout lines. This is enabled by the use of the multichannel electronics (MCE) provided by the University of British Colombia (UBC) [10, 9].

The TDM architecture for ACTPol uses DC superconducting quantum interference devices (SQUIDs) as amplifiers. The detector readout architecture is configured, for the HF array, into 32 columns of 64 rows each. Each TES in the array has its own stage one SQUID (SQ1), providing the first stage of amplification. Each column is readout by a unique SQUID series array at 1K, which provides a second level of amplification. Each row has an associated flux activated switch (FAS), which can be flux-biased to be in a normal state. This is done for a single row at a time, while the remaining rows are left superconducting. The normal FAS enables readout of the associated row. This switching is done at 7.8 kHz, though downsampled in the timestreams to $300 - 400$ Hz [40]. This architecture varies among the AdvACT arrays when it comes to the number of rows in the array. Since the HF detectors are smallest, more can be fit onto a single 150 mm wafer, such that the HF array has the highest multiplexing factor. For the remainder of this section we focus on the readout in the context of the LF array.

The LF array has a much smaller number of TESes than AdvACT's HF and

MF arrays but is read out using the same TDM scheme [39, 40, 19, 17]. Each TES in the LF array is voltage-biased and multiplexed through the warm Multi-Channel Electronics (MCE) using a SQUID-based TDM architecture developed at NIST/Boulder [10, 11]. Containing fewer pixels, the LF cold electronics is a simplified adaptation of the HF and MF designs, using the same PCB used in the HF and MF arrays. The LF array has a multiplexing (MUX) factor, or number of detectors per readout channel, of 26:1, whereas HF and MF have MUX factors of 64:1 and 55:1, respectively. The cold readout electronics are similar otherwise to the electronics described in [39, 40].

The LF array readout wiring has been designed such that TESes from polarization pairs at one optical frequency are read out on the same column and thus the same 1 K SQUID series array and 300 K warm amplifier. Unlike in the MF and HF arrays, each column in the LF array has its own dedicated TES bias line and dark TESes are wired to their own column. This is an improvement over the MF and HF readout because each detector type (27 GHz, 39 GHz, and dark), which will have different optimal bias powers, can be independently biased. Deliberate shorts on some unused shunt inputs have also been implemented, providing Johnson noise channels for independently probing detector bias line noise.

2.1.3 Advanced ACTPol Observing Strategy

In addition to the extensive hardware upgrades outlined above the deployment of AdvACT was accompanied by a new observation strategy. The ACTPol observing strategy, largely driven by its small angular scale science goals, focused

on performing deep measurements of several $70\,\mathrm{deg}^2$ patches of the sky. These fields were referred to as deep1, deep2, deep5, and deep6 (typically shortened to D1, D2, D5, and D6). As the observing campaign continued this was expanded to observing larger areas which included these small patches. These large patches were called deep56 (a combination of deep5 and deep6), and BOSS-North (a combination of deep1 and deep2 which overlapped with the BOSS northern observing area in addition to overlapping with KiDS and HSC). Deep56 covered 500 sq. deg. and BOSS-N covered 2000 sq. deg. In the final season with ACTPol fully deployed two additional fields, deep8 and deep9, were added, which were 190 sq. deg. and 700 sq. deg., respectively. The footprint of these fields on the sky is shown on the top of Figure 2.8 [22].

The AdvACT observing strategy expands the ACTPol sky area to cover approximately half the sky. The strategy is separated into nighttime and daytime strategies. The nighttime strategies are named 'wide_01h_n', 'wide_01h_s', and 'wide_12h_n'. The '01h' and '12h' refer to the center right ascension of each field, while the 'n' and 's' refer to the declination of the field. These fields cover areas of $\sim$5700 sq. deg., $\sim$5000 sq. deg., and $\sim$3400 sq. deg., respectively. All fields are observed both while they are rising and setting, which allows for cross-linking in the maps. They are also observed at several different fixed elevations. Twelve different observing strategies are made, four for each elevation, which are then rotated sequentially over every twelve night period throughout the season. Effort is made to optimize for uniformity and cross-linking of each field [22].

The daytime fields, 'day_02h_s' and 'day_14h_n', cover $\sim$1700 sq. deg. and $\sim$870 sq. deg. each, respectively. These fields will be used for measurements of the CMB B-mode polarization, as the larger angular scales required for this mea-

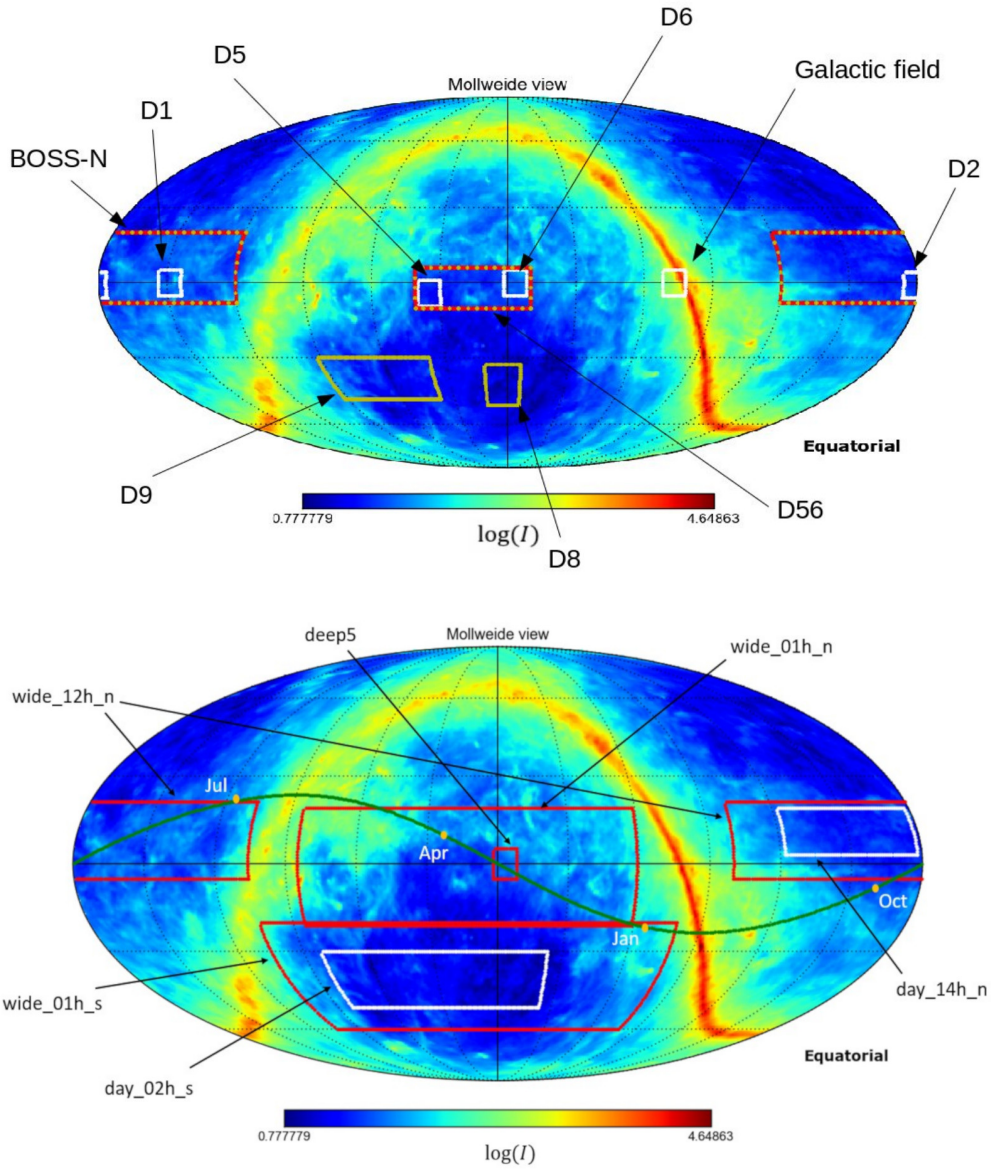

Figure 2.8: (Top): The ACTPol observing coverage. The small patches, D1, D2, D5, and D6 are the original ACTPol fields. These were eventually expanded into the D56 and BOSS-N fields, and D8 and D9 were added as lower priority targets. (Bottom): The AdvACT observing coverage. The observing area was drastically increased for AdvACT, covering nearly half the sky. Red boxes indicate night time fields, while white boxes indicate day time fields. Plots from [22].

surement should be less effected by the diurnal distortion of the beam shape. Together with the night time fields the total AdvACT observing area is $\sim 16,670$ sq. deg. This strategy has less than $\sim 1.3\%$ idle time [22].

2.2 Prototype Detector Characterization

A major change in the fabrication process for AdvACT is the move from working with 75 mm diameter wafers to 150 mm diameter wafers. This means all of the detectors are made on a single wafer and we no longer need to tile wafers to create the focal plane. Having a single, monolithic detector array can reduce polarization systematics due to mechanical alignment precision when tiling the array [23]. The larger the elements of the focal plane are the more obvious a mechanical rotation during installation becomes. A 75 mm wafer rotated by one degree produces a displacement of $\sim 1.3\,\mathrm{mm}$, for instance. [23] suggests a focal plane made from 75 mm wafers can be calibrated to better than 0.1°. This improves with the larger, 150 mm, wafer.

The move to 150 mm wafers, while reducing the complexity of the focal plane assembly process, comes with its own challenges in fabrication. Tools that can handle the larger wafers are required, and achieving uniformity across the entire wafer is important. In order to test the fabrication process prior to fabricating the final detector array the team at NIST makes a series of prototype detectors. These prototype detectors are fabricated on the same size, 150 mm, wafers that the final array will be fabricated on, but are etched into small, single detector test die.

These single detector test die come in two flavors. The first, look much like

a single detector will on the final wafer. They have all the components the final detectors will have, orthomode transducer, frequency selecting stub filters, and the transition edge sensors themselves. The second flavor contains a set of 12 transition edge sensors. These will have varying proprieties and are meant to test a wide range of TES designs in a small package (as they are often smaller and hold more TESes than a "single-pixel".)

The proprieties of these TESes, both on single-pixels and on the TES test die, are measured, and the results are fed back to the fabrication team at NIST, along with recommendations for changes in the next round of fabrication. If necessary, another round of test die fabrication can occur, confirming the changes resulted in the desired outcome. Once the target detector parameters are achieved the final array fabrication can be completed. The final array is then tested after integration and deployed into the field.

2.2.1 Background

Each pixel has four orthomode transducer (OMT) coupling probes, two for each linear polarization, connected to superconducting niobium microstrip lines that transmit radiation to the AlMn TES bolometers [68, 27]. There are four optical TESes per LF pixel, a pair for each linear polarization at both 27 and 39 GHz, as well as two dark TESes. Each TES island is weakly coupled to the cold bath by a set of four SiN legs. During operation, the TES is voltage-biased to keep it on the superconducting transition, T_c. The geometry of the TES legs determines the thermal conductance to the bath, G, which limits how much power the detector can dissipate before saturating.

f [GHz]	Estimated Loading [pW]	P_{sat} Target [pW]
27	0.5	1.5
39	2.6	7.8
90	3.7	11.3
150	4.5	12.5
220	12.5	25

Table 2.1: Loading estimates and associated saturation power targets for each AdvACT band. A factor of 2-3 is given as a safety factor when considering the estimated loading and the design detector saturation powers.

The TES leg geometry is selected to optimize the performance under expected loading conditions at the ACT site. The estimated loading for each AdvACT frequency band is given in Table 2.1. Loading on the detectors comes not only from the CMB, but also the surrounding environment. The dominant source is from the atmosphere. Other sources include emission from the mirrors and refractive optics as well as spillover from inside the optics tube and the telescope itself. The expected loading level at the nominal PWV is multiplied by a safety factor of 2-3 to set the target P_{sat}. P_{sat} combined with the expected T_c and T_{bath} determines the required G.

The following model is used to describe how P_{sat} is determined by the bath temperature, T_{bath}, and the critical temperature of the device, T_c:

$$P_{sat} = K(T_c^n - T_{bath}^n). \tag{2.1}$$

The thermal conductivity, G, is then given by,

$$G = \frac{dP_{sat}}{dT_c} = nKT_c^{n-1}. \tag{2.2}$$

The optimal TES leg geometries are determined by measuring current-voltage (IV) curves at many different bath temperatures, ranging from 50 to

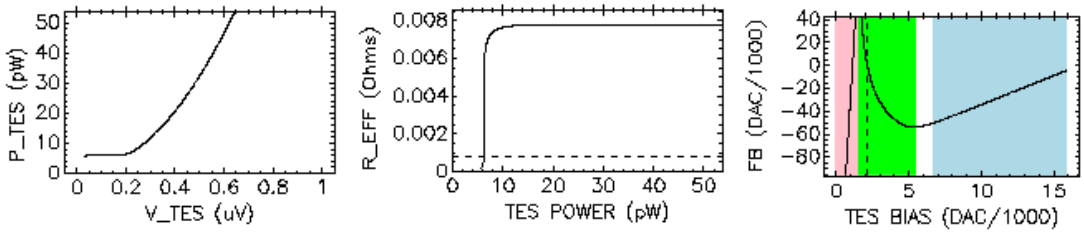

Figure 2.9: Example IV-curve from a single detector. (Left): TES power vs TES voltage bias. (Center): TES resistance vs power. (Right): Raw IV-curve data, feed back current (in DAC units) vs TES bias. Colors in the background identify the superconducting branch (red), transition (green), and normal branch (blue).

180 mK. An example IV-curve is shown in Figure 2.9. These IV curves are used to determine the bias power required to drive the TES to 90% of the normal resistance, R_n. We define this value to be the saturation power, P_{sat}. The bias powers at 90% R_n for each bath temperature are fit to Eq. (2.1), as shown in Fig. 2.10, for K, T_c, and n.

2.2.2 Setting Critical Parameters for AdvACT Detector Arrays

Starting with the HF array single pixels were fabricated on a 150 mm wafer for testing and selecting the final TES leg parameters. Four wafers of single pixel test die were made before choosing final leg parameters. For both the HF and MF arrays the leg lengths were kept constant at $61\,\mu\mathrm{m}$. The leg width was then changed to vary the saturation power. For the HF test die the first leg widths tested were $14.5\,\mu\mathrm{m}$ for the 150 GHz detectors and $28.4\,\mu\mathrm{m}$ for the 220 GHz detectors. The MF test die had leg widths of $13.5\,\mu\mathrm{m}$ for the 90 GHz detectors and $14.5\,\mu\mathrm{m}$ for the 150 GHz detectors. The leg thickness is determined

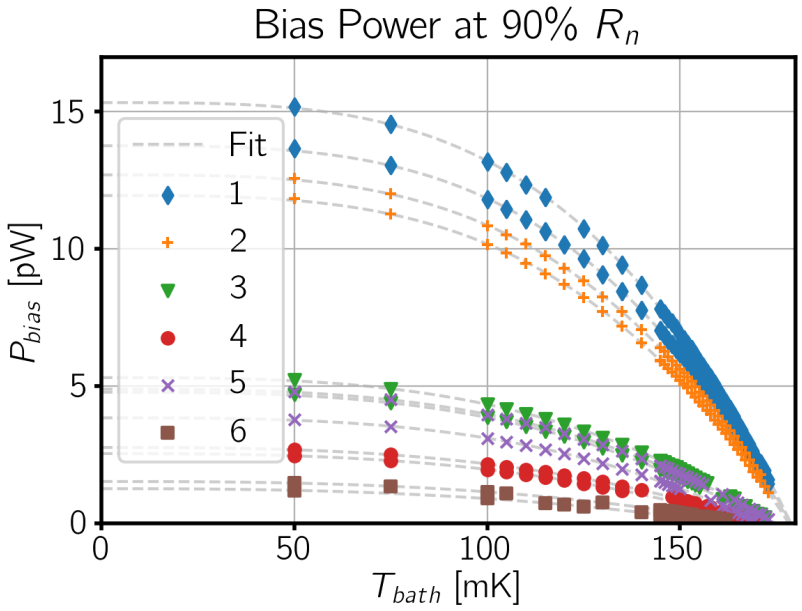

Figure 2.10: Bias power at 90% the normal resistance, R_n, as a function of the bath temperature, T_{bath}, for each of the tested prototype TES devices. The upper group, devices 1 and 2, are the 39 GHz devices while the lower group, devices 3, 4, 5, and 6, are lower saturation power 27 GHz devices. The fit for each individual device is to Eq. (2.1). Similar measurements were performed for the HF and MF prototype devices.

by the SiN thickness, which is kept at $2\,\mu\mathrm{m}$.

We find that the saturation power varies linearly as a function of leg width (with leg length and thickness kept constant). Figure 2.11 shows a plot of the saturation power as a function of leg width for these early HF and MF test die. The average critical temperature, T_c, was measured on these wafers to be higher than the target (160 mK). It was 178 mK for wafer 5 and 182 mK for wafer 6.

We can account for this discrepancy in the T_c by scaling the saturation powers to determine a scaling factor for the leg lengths for the next fab, with the

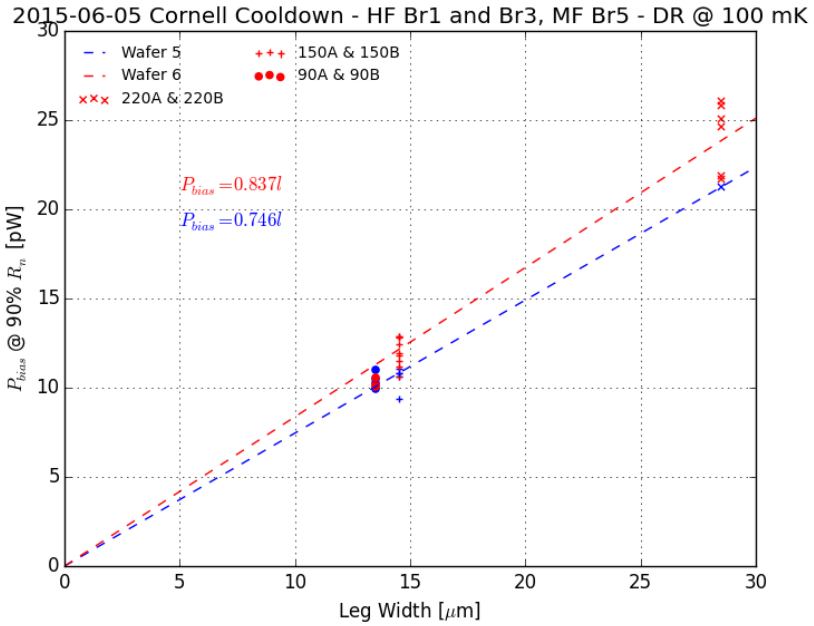

Figure 2.11: Bias power at 90% the normal resistance, R_n, which we take as the saturation power, P_{sat}, as a function of TES leg width for HF and MF test die from test fab wafers 5 and 6. The data are fit to a line with an intercept forced through zero. The blue dashed line corresponds to the fit for wafer 5, while the red dashed line corresponds to the fit for wafer 6. The individual symbols represent different detectors, identified by a label containing the frequency, and which polarization type it is, 'A' or 'B', which are orthogonal to each other.

assumption that the T_c will be corrected in the next fabrication. The T_c is controlled in fab through a heat treatment of the AlMn and varies with how long the wafer is heated [68].

The saturation power is given by Equation (2.1). The scaling factor is then simply given as the ratio of the two saturation powers,

$$\frac{P_{sat1}}{P_{sat2}} = \frac{T_{c1}^n - T_{bath}^n}{T_{c2}^n - T_{bath}^n}, \tag{2.3}$$

where the coefficient K cancels out. Based on scaling each of the test fab wafers'

critical temperatures to the target of 160 mK and averaging the leg length recommendations for each wafer we selected final leg widths of $24\,\mu\mathrm{m}$ for the 150 GHz detectors to achieve a target saturation power of $12.5\,\mathrm{pW}$ and $48\,\mu\mathrm{m}$ for the 220 GHz detectors to achieve a target saturation power of $25\,\mathrm{pW}$.

We followed the same procedure for the MF array, including additional data from new test die. This is summarized by Figure 2.12. The red and blue dashed lines again show a linear fit to the data. The black line is a fit to all the data. The green line shows this fit scaled to a critical temperature of 160 mK. This scaled fit results in recommended leg width of $24\,\mu\mathrm{m}$ for 150 GHz (in agreement with the HF selection), and $21.6\,\mu\mathrm{m}$ for the 90 GHz detectors, which is 90% of the 150 GHz leg width – the same ratio as for ACTPol's PA3.

The remainder of the discussion focuses on the LF array pixel prototypes and follows along with [62]. The target saturation powers for the LF array are 1.5 pW at 27 GHz and 7.8 pW at 39 GHz, which corresponds to three times the estimated loading at each frequency. These are much lower saturation powers than those in the MF (12.5 and 11.3 pW) and HF (25 and 12.5 pW) arrays, driving us to much longer leg lengths. Similarly long legs have been fabricated for SPIDER [29].

The LF detector test die leg parameters were selected by extrapolating a linear fit to the P_{sat} for the MF and HF detectors as a function of the cross-sectional area to the leg length, A/l. Test dies with several leg variants were then fabricated to explore the parameter space near $P_{sat} = 1.5$ and near $P_{sat} = 7.8\,\mathrm{pW}$. These variants, listed in Table 2.2, are shown in Fig. 2.13. Additional devices with different heat capacities (parameters listed in Table 2.3) were fabricated to optimize the temporal response of the detector. The detectors must respond

ID	f [GHz]	w [μm]	l [μm]	T_c[mK]	P_{sat}[pW]	G[pW/K]	R_n[mΩ]	n
1	39	14.4	61	178.9 ± 0.1	12.5 ± 0.7	276.1 ± 15.5	7.9 ± 0.1	3.4 ± 0.1
2	39	12.1	61	178.5 ± 0.2	10.5 ± 0.3	229.3 ± 7.5	7.8 ± 0.1	3.4 ± 0.1
3	27	10.0	220	173.4 ± 1.0	4.1 ± 0.2	88.3 ± 4.5	7.5 ± 0.1	3.0 ± 0.1
4	27	10.0	500	170.5 ± 1.2	2.1 ± 0.1	44.0 ± 1.7	7.5 ± 0.1	2.8 ± 0.1
5	27	15.0	500	172.9 ± 1.9	3.5 ± 0.4	76.5 ± 7.3	7.5 ± 0.1	3.0 ± 0.1
6	27	10.0	1000	164.7 ± 2.5	1.0 ± 0.1	22.6 ± 2.3	7.5 ± 0.1	2.7 ± 0.1

Table 2.2: Fabricated and measured prototype detector properties. ID corresponds to the device design variations shown in Fig. 2.13 (Left), f is the design frequency for the detector, w is the TES leg width, l the TES leg length, T_c is the critical temperature of the TES, P_{sat} is the saturation power of the detector, G is the thermal conductivity, R_n is the normal resistance, and n is the thermal conductivity exponent. Parameters correspond to a bath temperature of 100 mK, which is the temperature of the devices in the field. The mean and standard deviation of each parameter for the measured devices is shown. Uncertainties shown do not account for correlation between parameters.

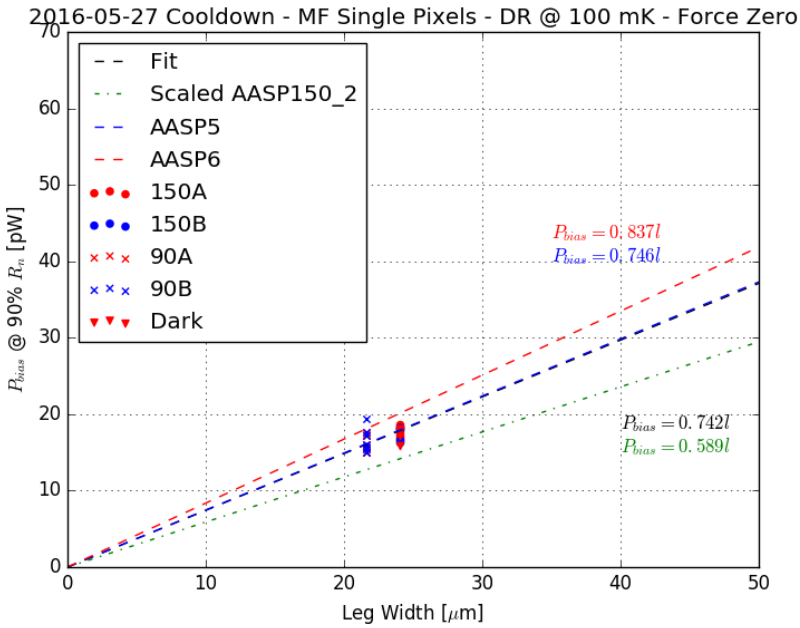

Figure 2.12: Bias power at 90% the normal resistance, R_n, as a function of leg width for MF test die from wafers 5, 6 (AASP5 and AASP6) as well as a third fabrication (AASP150_2). The blue and red lines are fits to wafer 5 and 6 detectors from Figure 2.11, respectively. The black line is a fit to all data, which includes AASP150_2. The green dashed line shows the fit scaled to the target critical temperature of 160 mK and is used to select the final MF leg parameters.

ID	**f** [GHz]	**w** [μm]	**l** [μm]	**AlMn Vol.** [μm^3]	**PdAu Vol.** [μm^3]
A	27	20.0	500	36538	0
B	27	10.0	500	2640	0
C	27	10.0	500	14866	0
D	27	10.0	500	36538	0
E	27	10.0	500	36538	21452
F	27	10.0	500	36538	36113

Table 2.3: Device properties for the six AlMn and PdAu variation devices. A unique ID is given to each design variation, **f** is the design frequency for the detector, **w** is the TES leg width, **l** the TES leg length, the AlMn volume and PdAu volume are the amount of each material on the TES island.

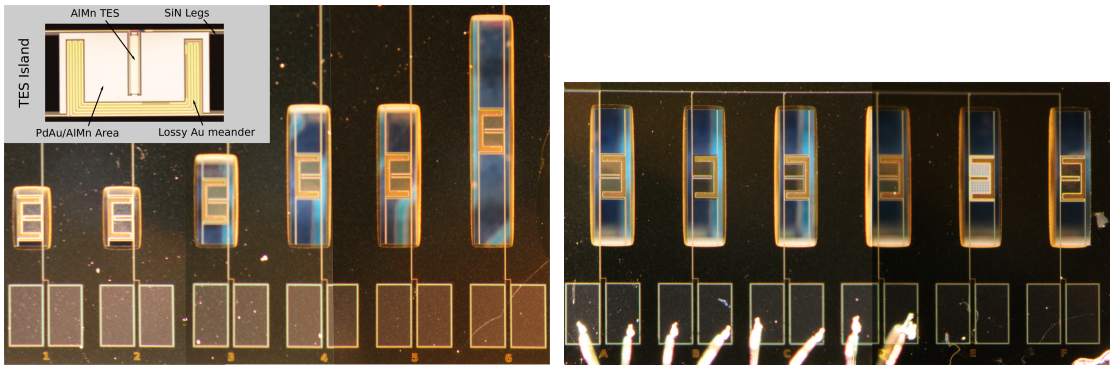

Figure 2.13: (Left): LF prototype transition edge sensors with different leg geometries. The devices are labeled 1 to 6 from left to right. Table 2.2 lists the design frequency and leg parameters for each of the devices. Inset to this figure in the upper left is a close up of a single labeled TES island. (Right): LF prototype TESes with the different PdAu/AlMn volumes listed in Table 2.3. The devices are labeled A to F from left to right. Devices A through D have no PdAu, with devices A and D having the full AlMn volume. Device B only has AlMn in the central region that forms the TES, while device C has a reduced area of AlMn. Devices F has a full volume of PdAu and AlMn and device E has a pattern of holes in the PdAu, referred to as "swiss" as in Swiss cheese.

quickly enough to prevent smearing of the signals from the sky or from the half-wave-plate modulators [39], but this must be balanced against the temporal response becoming so fast that the detectors become unstable [49]. Both types of devices were characterized, and the final leg and heat capacity geometries for use on the LF array were selected based on those results.

Based on previous measurements of the P_{sat} values for the MF and HF detectors, we expect P_{sat} to be proportional to the ratio of A/l [39]. In Fig. 2.14, we show the measured P_{sat} vs the ratio of A/l. The black-dashed line is the best-fit linear relation, which was used to select the leg geometry of the 39 GHz detectors. For these, we choose to keep the leg length the same as the HF and MF

detectors, $l = 61\,\mu\mathrm{m}$, which gave a width, w, of $12.1\,\mu\mathrm{m}$.

The 27 GHz detectors have the lowest target P_{sat} of all the AdvACT detectors at $1.5\,\mathrm{pW}$. While the test die parameters were selected based on the HF and MF linear fit, we find that the low saturation power, longer leg length detectors differ in their behavior with P_{sat} as a function of A/l in that the slope is larger by about a factor of two. This may be due to the phonon transport differing for the much longer legs. This difference is reflected in the 27 GHz devices having a thermal conductance exponent, n, ≤ 3, compared to $n \sim 3.4$ for the 39 GHz devices, as shown in Table 2.2. While we do not account for correlation between fit parameters in our error determination in Table 2.2, we do find there to be a negative correlation between T_c and n, so for a fixed T_c the difference between the 27 and 39 GHz detector n values will persist. We fit the devices with $l > 61\,\mu\mathrm{m}$ independently, leading to the gray dashed line in Fig.2.14, which we used to select the final 27 GHz detector leg parameters of $w = 10\,\mu\mathrm{m}$ and $l = 628\,\mu\mathrm{m}$. Measured prototype device parameters are shown in Table 2.2. The measured critical temperatures for most of the devices were found to be above the LF target of 165 mK. Selection of the final leg geometries for fabricating the LF array was done after scaling these results to a T_c of 165 mK.

The detector responsivity decreases with increasing frequency due to the thermal time constant of the detector, which can be varied by adding heat capacity to the TES island. We tested six different recipes of PdAu and AlMn, in order to explore how the time constant varied as a function of each materials volume. These six test devices were all 27 GHz devices, four with AlMn volumes ranging from $2640\,\mu\mathrm{m}^3$ to $36538\,\mu\mathrm{m}^3$ and no PdAu, two of which had the same AlMn volume but different leg widths, and two with the full $36538\,\mu\mathrm{m}^3$

AlMn volume while having either $21452\,\mu\mathrm{m}^3$ or $36113\,\mu\mathrm{m}^3$ of PdAu. Extrapolations from the previously fabricated MF devices were suitable for the 39 GHz devices.

We report the time constant of the detector as $f_{3dB} = 1/2\pi\tau$, defined as the frequency at which the response of the detector decreases by a factor of two compared to the DC response. The target f_{3dB} for the LF detectors ranges from 81 to 275 Hz for 35%-70% R_n across the range of expected bias powers under loading in the field. This range is set by requiring fast enough detectors to observe with a rapidly rotating half-wave plate modulator, but not too fast that they could become unstable [39].

We test the response time by adding a small square-wave to the voltage bias applied to the detectors with amplitude ranging from $1-5\%$ of the DC bias value. The response is sampled at 250 kHz to measure the exponential fall time of the detector current, or τ. We do this at six different bath temperatures and several different points on the TES transition, measured by the TES resistance relative to normal, $\%R_n$, as shown in Fig. 2.15. These data are then fit to a two-fluid model described by Eq. (2.4), where A and B are a function of measurable parameters specified in [48], and P_{bias} is the bias power,

$$f_{3dB} = A + BP_{bias}^{2/3}. \tag{2.4}$$

This model fits the data well with a fixed natural time constant at zero bias power (Fig. 2.15), though a linear model yields similar results.

From these data, we found that having PdAu on the 27 GHz devices, in addition to the full AlMn volume, decreased the f_{3dB} below our target threshold of 81 Hz. Based on this we chose to have 73% of the full (largest tested) AlMn volume (full being $36538\,\mu\mathrm{m}^3$) and no PdAu on the 27 GHz detectors and 100% of

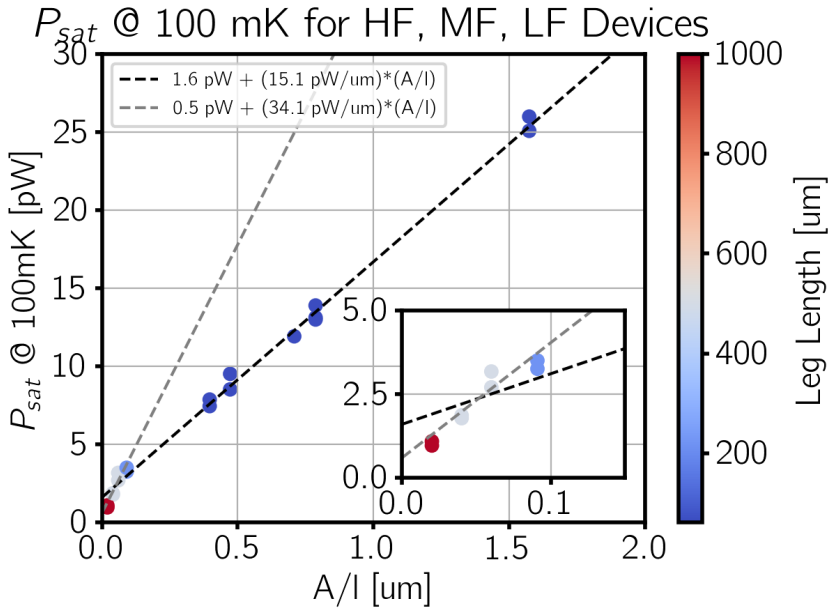

Figure 2.14: Plot of P_{sat} versus A/l, where A is the cross-sectional area of one of the four TES legs and l is its length, for typical HF (230/150 GHz), MF (150/90 GHz), and LF (39/27 GHz) devices. The color scale shows the leg length, with all HF, MF and 39 GHz LF legs being $61\,\mu\mathrm{m}$ long, while the LF 27 GHz test devices have a range of longer leg lengths as indicated in Table 2.2. The black dashed line fit is to the HF, MF, and 39 GHz LF detectors. The gray dashed line is a fit to just the 27 GHz LF detectors, which have the lowest saturation power of all the AdvACT detectors, and differ from the trend exhibited by the $l = 61.0\,\mu\mathrm{m}$ detectors. We allow for a non-zero P_{sat} offset in the fit, which may be present due to residual conductance from the Nb. The inset plot is a zoom in on the low P_{sat} LF detectors.

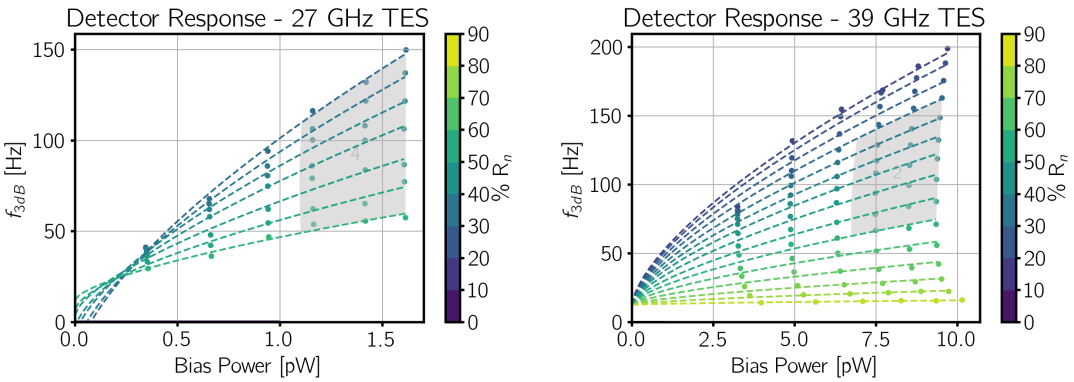

Figure 2.15: Bias step results for a single 27 GHz (left) and 39 GHz (right) prototype detector. The gray region indicates the targeted operating range of the detector in the field. Each vertical grouping of points is at one bath temperature. The bias point in $\%R_n$ is selected and then a square wave is applied. The f_{3dB} is measured from the response to the square wave and this is repeated for a full range of bias points before moving to the next temperature. These data are used to estimate the detector response speed under a range of optical loading and biasing conditions in the field.

the full AlMn volume and 76% of the full volume of PdAu (full being $36113\,\mu\mathrm{m}^3$) for the 39 GHz detectors.

We fully characterized new test dies, which were designed to demonstrate the low P_{sat} values needed to optimize the LF array. The LF cryogenic readout electronics have been assembled and tested. The LF detector array was fabricated at NIST and has undergone testing at Princeton. The detectors on the array have an average saturation power of $1.3 \pm 0.2\,\mathrm{pW}$ for the 27 GHz detectors and $7.8 \pm 1.4\,\mathrm{pW}$ for the 39 GHz detectors [69]. The LF array will be deployed in early 2019, extending the range of AdvACT from 27 GHz to 230 GHz. A summary of the achieved saturation powers for each AdvACT array are shown in Table 2.4.

Array	f [GHz]	l [μm]	w [μm]	P_{sat} Target [pW]	P_{sat} Achieved [pW]	Ref.
HF	220	61	48	25.0	26 ± 1	[90]
HF	150	61	24	12.5	13 ± 1	
MF1	150	61	24	12.5	13.9 ± 0.6	[17]
MF2					15.4 ± 1.2	
MF1	90	61	21.6	11.3	12.4 ± 0.7	
MF2					13.7 ± 1.4	
LF	39	61	12.1	7.8	7.8 ± 1.4	[69]
LF	27	628	10.0	1.5	1.3 ± 0.2	

Table 2.4: Fabrication parameters with target and achieved saturation powers for each device type in the final AdvACT arrays.

This demonstrates our ability to cover a wide range of saturation powers (as low as 1 pW) and detector response speeds through modification of the detector leg length, the leg width, the AlMn volume, and the PdAu volume on a single detector design. This has direct application to detector design for future CMB experiments, such as the Simons Observatory and CMB-S4, which will face similar design challenges.

2.3 The ACTPol Receiver Baffle

Stray light entering the ACT receiver can cause excess thermal loading which will result in decreased sensitivity and may result in the saturation of some detectors depending on their saturation power. I designed and built a baffle to go around the first ACTPol array during my first trip to the ACT site in 2013 (Fig. 2.16).

The effect of adding the baffle, tested by repeatedly performing IV curves with the baffle on and off, was a decrease in the average loading by 0.7 pW.

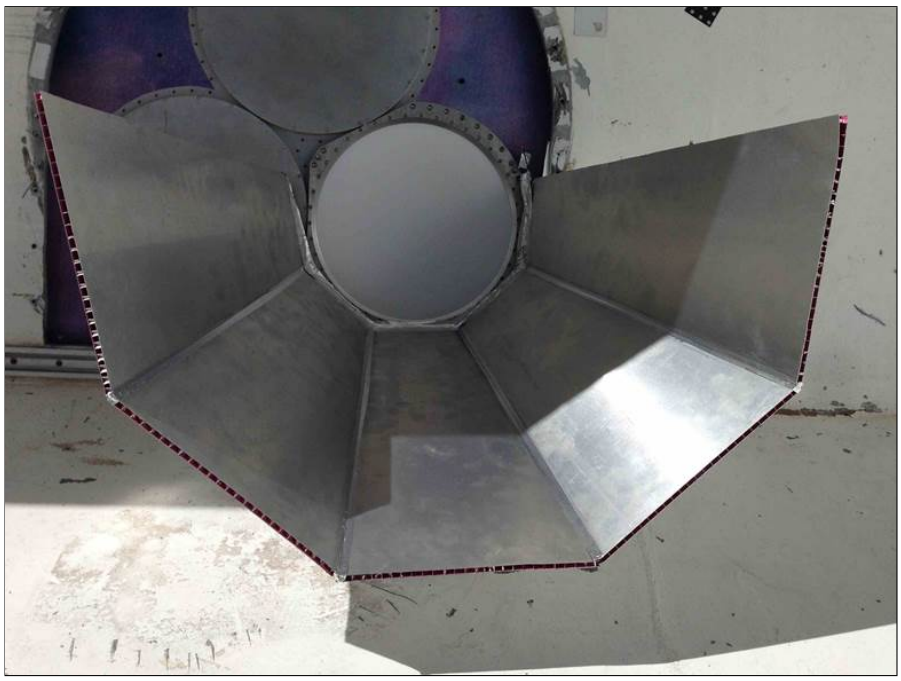

Figure 2.16: The first ACTPol receiver baffle attached in front of the first ACTPol array, ar1. The baffle was designed to have an opening angle of 20 degrees past perpendicular and is meant to reflect to the sky, rather than into the warm telescope body.

With a 100% efficient detector this corresponds to a loading change of $\sim 1.2\,\mathrm{pW}$.

Planets were observed with the baffle on and off to determine the effect of the baffle on the beam shape. Figure 2.17 shows averaged maps of Venus and Saturn with and without the baffle on ar1 taken during September and October 2013. The solid angles of each planet with the baffle on were slightly larger, but overall the beam shape changes were minor enough that we decided to keep the baffle equipped for the season.

The single array baffle for ar1 was adapted to fit around the entire receiver for the 2014 season. With the prospect of the AdvACT upgrade looming we began making plans for mounting three continuously rotating half-wave plates

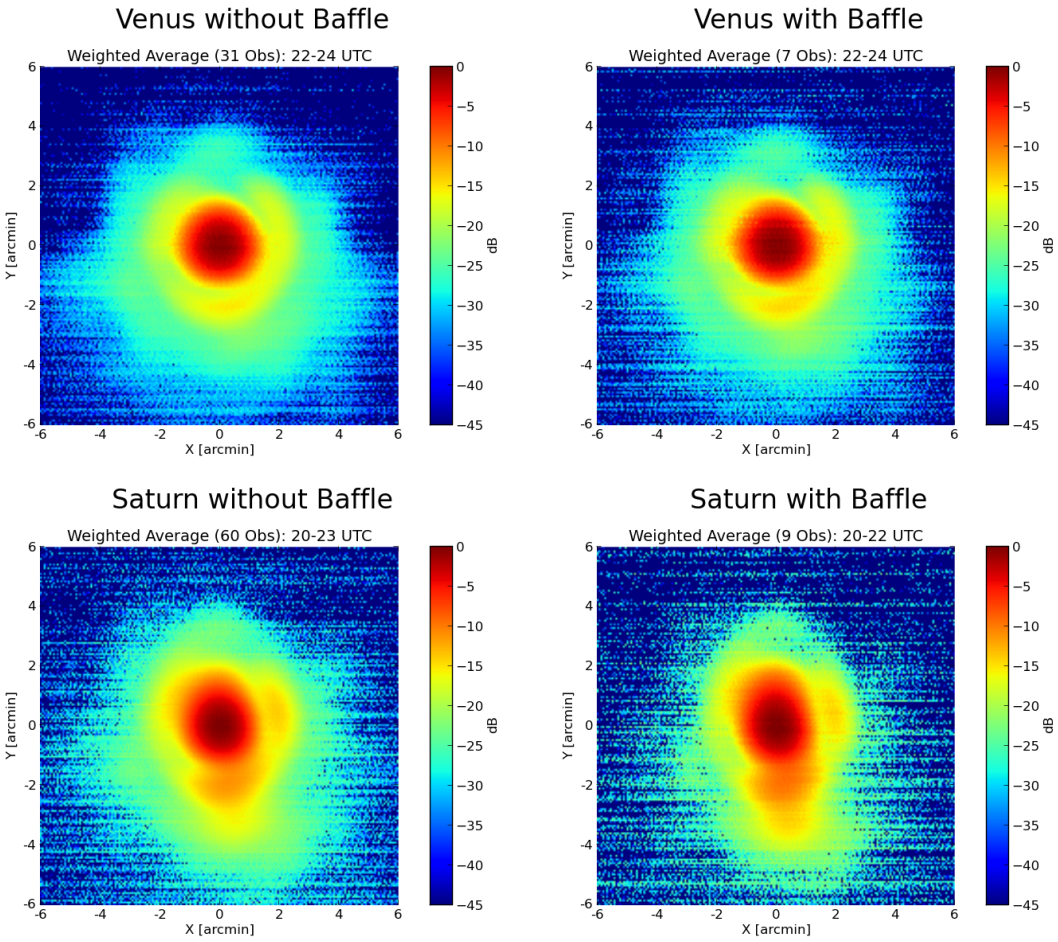

Figure 2.17: Averaged intensity maps of Venus and Saturn, with and without the ar1 baffle. The solid angle for Venus with the baffle was 200 nsr, without the baffle it is 190 nsr. Similarly for Saturn with the baffle the solid angle is 262 nsr and without the baffle, 245 nsr. This slight change in the beam shape was accepted with the decrease in excess thermal loading the baffle provided. Planet maps provided by Marius Lungu.

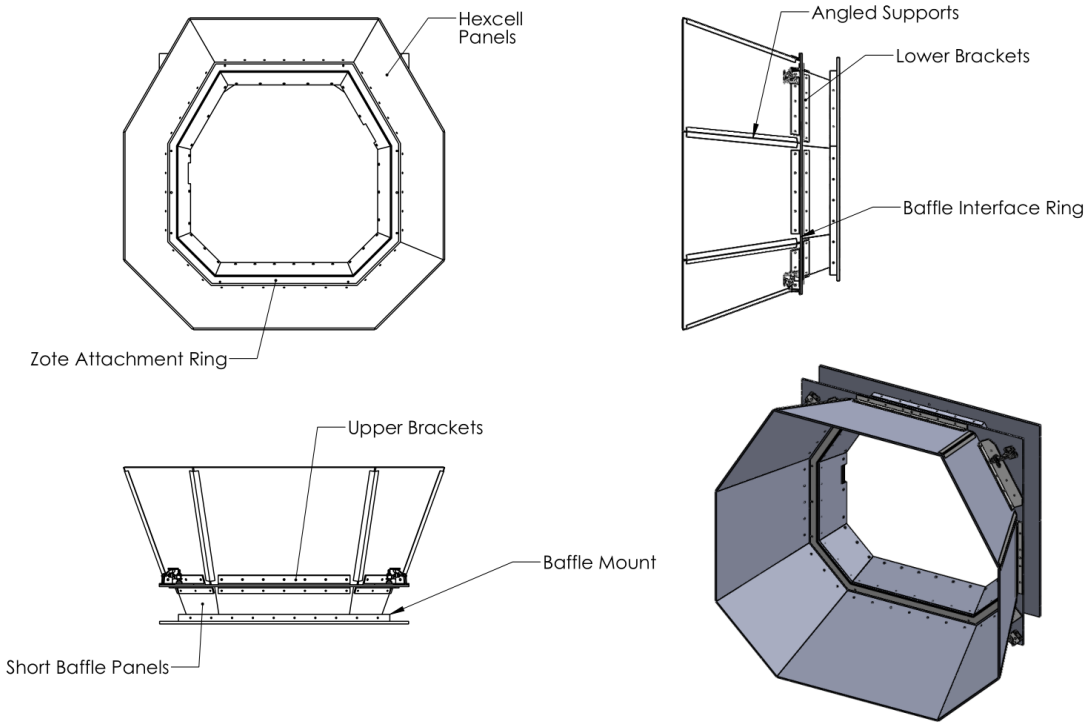

Figure 2.18: Assembly overview for the AdvACT receiver baffle. The design features a short, mechanically robust baffle made from $1/4$ in aluminum, a ledge which forms an attachment point for a sheet of Zotefoam to protect the HWPs from UV radiation from the sun, and a longer, light-weight hexcell aluminum front baffle. Inspired by the original baffle for ar1, this baffle has been installed for the duration of the AdvACT observation campaign.

(HWP) in front of the three ACTPol receiver windows. These HWPs would be made of a silicon meta-material and would float on an air-bearing while being spun by an external motor. The sensitivity of the silicon in the HWPs to UV from the sun, coupled with the fragility of the air bearing/external motor/encoder electronics drove the need to develop a way to protect these components from the harsh elements at the ACT site. This lead to a redesign of the baffle for permanent installation during the 2015 season.

The AdvACT baffle is shown in Figure 2.18. The design features a split baffle, consisting of a short, mechanically robust, base baffle made from 1/4 inch thick aluminum panels. This mounts to a thick baffle mount and is meant to be permanently affixed to the telescope body in front of the receiver. In practice the entire baffle is often unmounted when close access to the receiver is required, during FTS band measurements for instance. The base baffle forms a ledge to which a sheet of Zotefoam can easily be mounted. Zotefoam is a commercial foam that has high transmission in the microwave but low transmission in the UV. This Zotefoam sheet serves two purposes: one, to shield the HWPs from the UV; two, to protect the HWP motor/encoder electronics from the harsh elements of the Atacama. The baffle has been installed for the duration of the AdvACT observation campaign.

2.3.1 Silicon Resistivity Measurements

Careful selection of the materials used to fabricate the ACT silicon lenses and metamaterial HWPs is required. High resistivity (ideally $\sim 10 - 20\,\mathrm{k}\Omega{-}\mathrm{cm}$) silicon has a lower loss tangent, making it preferred for use in the telescope's optical path [5]. While the silicon lenses are kept at 4K behind several filters, the HWPs are the first optical element after the secondary reflector and are outside of the cryostat, at room temperature. This exposes them to UV radiation from the sun.

UV radiation excites electrons in the silicon into the conduction band, decreasing the resistivity and increasing the loss tangent, resulting in increased loss in the ACT science bands. The Zotefoam sheet mounted to the AdvACT

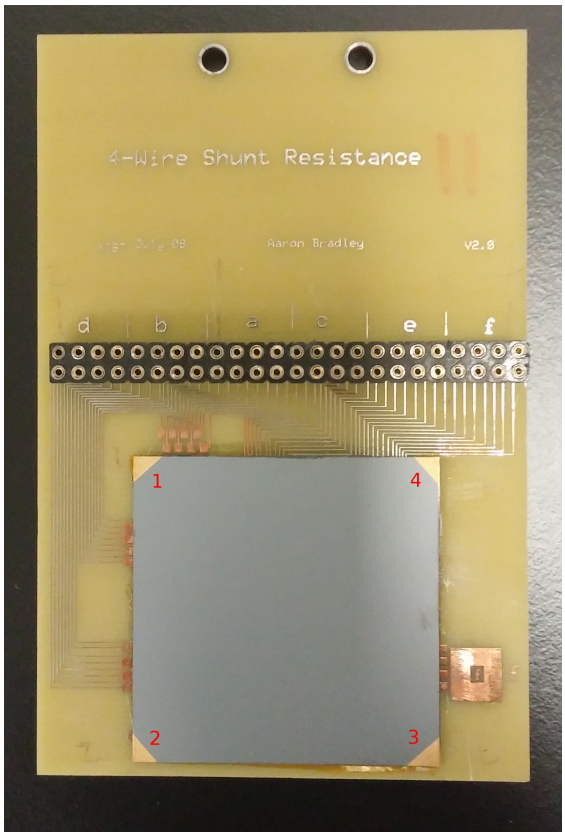

Figure 2.19: Silicon sample mounted to four lead board for resistivity measurements.

baffle should mitigate this effect, but by how much? To answer this question we performed a series of four lead measurements on a sample of silicon from the same bool used to make the ACTPol lenses.

Using the Van der Pauw method we measured the resistivity of a 3.81 cm square sample of silicon [96]. We made measurements of the resistivity in direct sunlight, with the sample covered with Zotefoam of several thicknesses, in the lab, and in the dark, both at Cornell and at the ACT site in Chile. A photo of the silicon sample attached to the four lead board can be seen in Figure 2.19.

With our square sample, numbering counter clockwise from the upper left

corner, 1, 2, 3, 4, a "vertical" measurement is one with the input current from, say, 1 to 2, and the sense from 3 to 4. A "horizontal" measurement would be for instance input from 2 to 3, and sense from 4 to 1. All measurements were made using the four point measurement feature of a bench top multimeter.

Our convention for naming these resistances is as follows, for input current from point 1 to 2 and sense from 3 to 4, we define $R_{12,34}$ as,

$$R_{12,34} = \frac{V_{34}}{I_{12}}. \tag{2.5}$$

The Van der Pauw formula can then be written as,

$$e^{-\pi R_{12,34}/R_s} + e^{-\pi R_{23,41}/R_s} = 1. \tag{2.6}$$

To improve the accuracy of our measurement we make four measurements in each of the "vertical" and "horizontal" configurations, and average the results, obtaining,

$$R_{vertical} = \frac{R_{12,34} + R_{34,12} + R_{21,43} + R_{43,21}}{4}, \tag{2.7}$$

and

$$R_{horizontal} = \frac{R_{23,41} + R_{41,23} + R_{32,14} + R_{14,32}}{4}. \tag{2.8}$$

The Van der Pauw formula then becomes,

$$e^{-\pi R_{vertical}/R_s} + e^{-\pi R_{horizontal}/R_s} = 1. \tag{2.9}$$

If $R_{vertical} \neq R_{horizontal}$, which is sometimes the case, then we solve for R_s numerically. Once we have R_s, the sheet resistance, we can calculate the resistivity, ρ, given the thickness t, which we know to be 0.029 cm, as

$$\rho = R_s t. \tag{2.10}$$

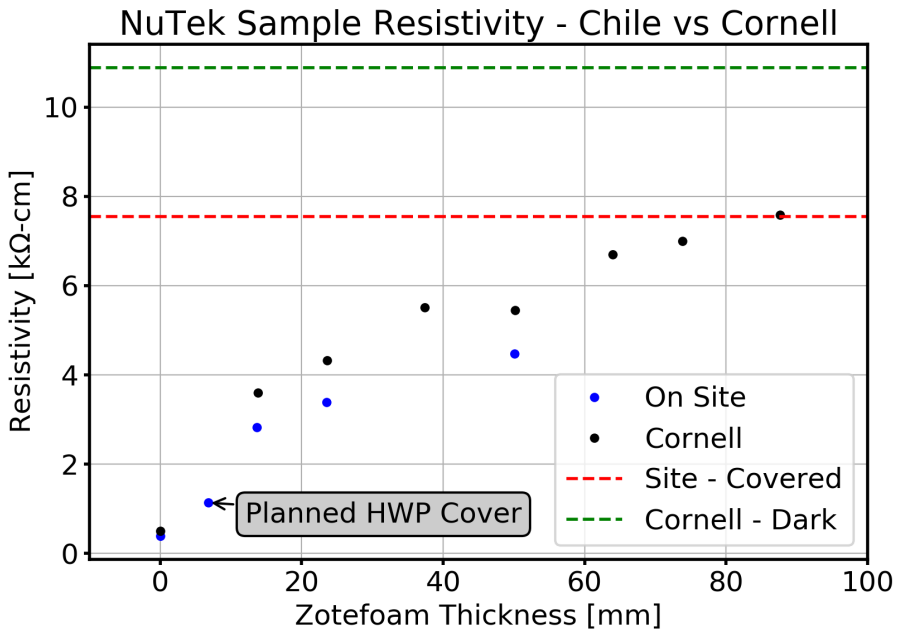

Figure 2.20: Resistivity of sample as a function of Zotefoam thickness. This is in direct sunlight unless otherwise noted. By "Site - Covered" I mean the sample was in direct sunlight, but instead of being covered by Zotefoam it was covered by my lab notebook.

I performed measurements both in North America, at Cornell, and in Chile at the ACT site. Figure 2.20 shows the measured resistivities both at Cornell and at the site. Note the resistivity of the sample with the thickness of Zotefoam planned for the HWP cover is 1.13 kΩ-cm.

During the day, while we scan, the HWPs will sometimes be in direct sunlight, sometimes shaded by part of the telescope and sometimes shaded with reflected light from part of the telescope. I measured the resistivity of our sample in several different configurations to test how the resistivity changes when in the shade or when in the shade with strong reflections hitting the HWPs. The resulting resistivities are shown in Figure 2.21. The Zotefoam thickness here is

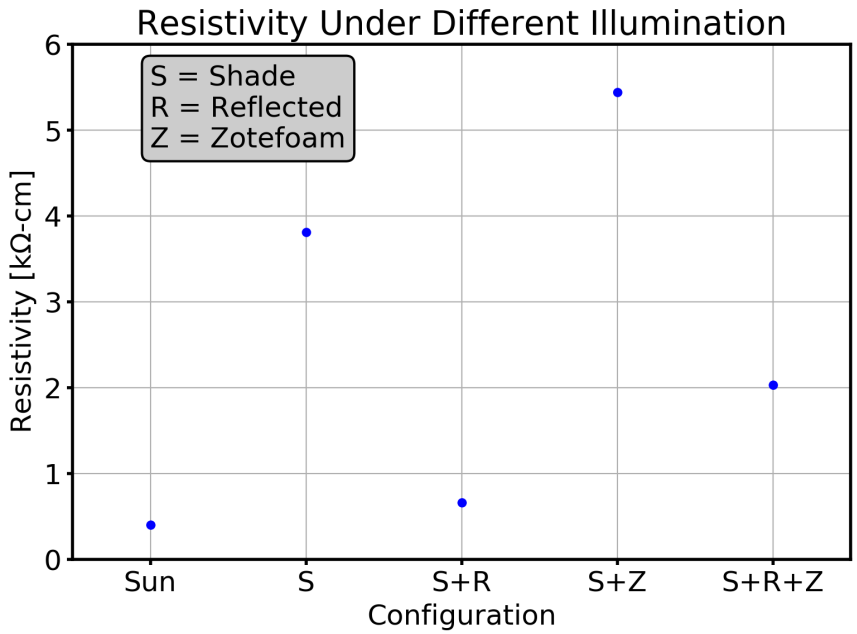

Figure 2.21: Resistivity of the NuTek sample under different illumination conditions. From left to right they are, direct sunlight, shaded, shaded with reflected light, shaded with Zotefoam, and shaded with Zotefoam and reflected light.

the one planned to be used as a HWP cover, which is 6.75 mm thick. Reflected light, even with the Zotefoam cover, reduces the resistivity to $\sim 2\,\mathrm{k\Omega{-}cm}$.

Estimating the dielectric and conductive loss in warm silicon

If we know the resistivity of the metamaterial HWP silicon we can estimate the amount of loss we might expect given conditions at the site. The attenuation factor in a dielectric (assuming negligible magnetic loss), α, can be written,

$$\alpha = \frac{2\pi}{\lambda_0}\left[\frac{1}{2}\kappa'\left(\sqrt{1+\tan^2\delta}-1\right)\right]^{1/2}, \tag{2.11}$$

where λ_0 is the free space wavelength of the incident radiation, κ' is the relative permittivity (or dielectric constant), and $\tan\delta$ is the loss tangent [97]. In the limit

$\tan\delta << 1$ this can be written (with binomial expansion of the inner square root term) as,

$$\alpha \approx \frac{\pi}{\lambda_0}\sqrt{\kappa'}\tan\delta. \tag{2.12}$$

In the presence of a conduction term the loss tangent goes to,

$$\tan\delta \rightarrow \tan\delta_d + \frac{1}{\epsilon_0\kappa'\omega\rho}, \tag{2.13}$$

where $\tan\delta_d$ is the dielectric loss tangent, ϵ_0 is the permittivity of free space, ω is the angular frequency, and ρ is the resistivity [64]. (Note that when cooled below the $\sim$1 eV energy gap the loss tangent can be represented by only the right hand term on the right side of Equation (2.13).) We substitute this into the expression for α,

$$\alpha \approx \frac{\pi}{\lambda_0}\sqrt{\kappa'}\left(\tan\delta_d + \frac{1}{\epsilon_0\kappa'\omega\rho}\right). \tag{2.14}$$

If the thickness of HWP is given by l, we can approximate the loss, L (which goes as $e^{-\alpha l}$) by,

$$L \sim \alpha l. \tag{2.15}$$

Written with the full expression for α we have,

$$L \sim \frac{\pi}{\lambda_0}\sqrt{\kappa'}\left(\tan\delta_d + \frac{1}{\epsilon_0\kappa'\omega\rho}\right) l. \tag{2.16}$$

Rearranging a bit and substituting in for ω and ϵ_0 yields,

$$L \sim \left(\frac{\pi}{\lambda_0}\sqrt{\kappa'}\tan\delta_d + \frac{\mu_0 c}{2\sqrt{\kappa'}\rho}\right) l. \tag{2.17}$$

We know, or can lookup values for all of these variables. For room temperature high resistivity silicon, measured at 150 GHz, $\lambda_0 = 2$ mm, $\kappa' = 11.7$ [5], $\tan\delta_d \sim 8\times10^{-5}$ [80] and we measured ρ for our silicon sample with various illumination and Zotefoam configurations.

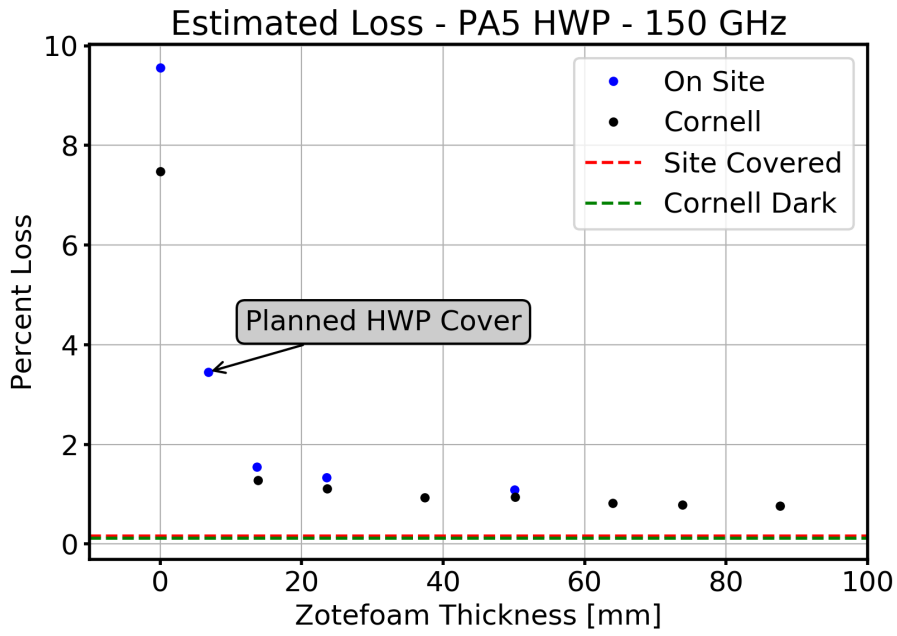

Figure 2.22: Percent loss from the PA5 silicon metamaterial HWP as a function of Zotefoam thickness. Note this assumes a uniform thickness of silicon, which is not true, thus over estimating the loss.

Given the HWP thickness and it's measured resistivity we can estimate the loss. The calculated loss for a solid silicon disk of the PA5 HWP thickness ($6.53\,\mathrm{mm}$) as a function of Zotefoam cover thickness is shown in Figure 2.22. We note that the expected silicon loss is lower due to much of the silicon being removed during the fabrication process, however, the glue used to hold the HWP wafers together may also contribute to the HWP loss and is not accounted for here.

The measured resistivity (in direct sunlight) with the planned HWP cover thickness of $1/4$ inch was $1.13\,\mathrm{k\Omega-cm}$. This corresponds to a loss of 3.45%. We can compare this with the measured loading from the HWPs, measured by performing IV-curves with and without the HWP installed on the telescope, by

multiplying this loss percentage by ambient temperature (270 K). By this calculation we should expect loading of approximately 9.3 K from the HWP.

On/off measurements of with the HWPs show approximately 8 K loading on PA4, 15 K loading on PA5, and 9 K loading on PA6, all at 150 GHz. This is close to the estimated 9.3 K loading. The PA5 and PA6 HWPs are of comparable thicknesses, as they are designed for identical bands (90 and 150 GHz); however, the PA4 HWP is thinner, so we should expect less loading from it. The uncertainty in the measured loading is large due to background loading variations with weather. Additionally, during the day the HWPs are not always in direct sunlight, but either partially shaded or illuminated from reflections off of other parts of the telescope. These loading measurements were performed over a 2 hour time frame during which the PWV was approximately 0.8-0.9 mm. Increasing the Zotefoam thickness should help decrease this loading during the day. The loading is expected to decrease at night when the sun has set. The resistivity was not measured at the site in the dark, but if we consider the covered measurement as equivalent, and if the silicon is the dominant source of loss in the HWPs, then we would expect the loss to reduce to $\sim 0.16\%$, which corresponds to approximately $0.43\,\mathrm{K}$ of loading.

2.4 Summary

In this Chapter we have provided an overview of the Atacama Cosmology Telescope Polarimeter and the Advanced ACTPol upgrade. We have focused on the iterative testing of prototype AdvACT detector test die for selection of the TES leg geometries. These parameters are tuned for each frequency band and

achieve saturation powers as low as 1 pW. We have also discussed the AdvACT receiver baffle and associated measurements of the resistivity of silicon used in the AdvACT rapidly rotating HWPs.

This gives important context for the following chapter, which provides an overview of the detector polarization angle calibration. The geometry of the detector arrays, shown in Figure 2.4, provides the lithographically defined geometry as the starting point for the calibration presented in Chapter 3.

CHAPTER 3

OPTICAL MODELING OF INSTRUMENT POLARIZATION

Instrument polarization refers to any systematic effects which exist within the instrument optical chain that may affect the polarization of light. This may include effects such as intensity to polarization, $I \rightarrow P$, leakage or the rotation of the polarization vectors by off-axis optical elements. The correction of these effects is critical in measurement of the linearly polarized CMB as any offset in the polarization angle of the detector elements will lead to a non-zero EB cross correlation signal as described in Section 1.2.4.

The ACTPol telescope and receiver design was modeled with the optical design software Code V. Using Code V we load the ACTPol telescope model, perform a ray trace to construct a function which transforms focal plane coordinates to coordinates on the sky, and use a polarization sensitive ray trace to calculate polarization rotations caused by the optics. Together, these provide a final polarization angle calibration for each detector on the focal plane, which forms a critical input to the map making process.

Code V is a software package developed by Synopsys[1] used to "model, analyze, optimize, and provide fabrication support for the development of optical systems." While the field is moving towards exclusive use of a competing software, Zemax OpticStudio[2], the work in this thesis uses Code V, which offers some advantages, in addition to the fact that the telescope design and instrument designs were primarily developed using Code V. See Appendix A for a brief comparison between the two programs in the context of modeling the po-

[1] https://www.synopsys.com/optical-solutions/codev.html
[2] https://www.zemax.com/products/opticstudio

larization properties of an optical design.

In this chapter we start by discussing the ACT telescope model in Code V. Then we perform a ray trace through the ACTPol optical chain to model the detector sky positions. In Section 3.2 we activate the polarization sensitive ray tracing capabilities of Code V to model the systematic instrument polarization of the ACTPol optical chain. These two components come together to form the polarization angle calibration for the ACTPol and AdvACT data sets in 3.3.

3.1 Ray Tracing to Model Detector Sky Coordinates

As mentioned in Section 2.1, the starting point for our calibration is the lithographically defined angles for each detector. Tiled into an array (in the case of ACTPol), or fabricated on a single wafer (as in AdvACT), these populate every 15 degrees from 0 to 180 degrees. Table 3.1 shows the distribution of angles for each array. The detectors all lie behind a nanofabricated set of corrugated feedhorns whose positions are known precisely, which establishes a set of focal plane coordinates. These focal plane coordinates, coupled with the detector angles, form our initial parameters. All rotations are applied to these angles to produce our final angle calibration.

The first step in our calibration is to determine the installation angle, which is a global rotation of the detectors as an array is installed into the ACTPol receiver. This installation angle is different for each array and arises due to mechanical constraints within the receiver. Observations of Saturn and Uranus are fit to a 2D Gaussian per detector, which gives us pointing information for each feed and allows us to determine the installation angle. Knowing where each detector

Table 3.1: Number of detectors at each detector angle in focal plane coordinates for all three ACTPol arrays and the first three AdvACT arrays.

Angle	PA1	PA2	PA3	PA4	PA5	PA6
0°	87	80	86	168	140	140
15°	87	87	76	168	144	144
30°	80	87	86	170	144	144
45°	87	79	84	168	144	144
60°	87	87	78	170	144	144
75°	79	87	84	168	142	142
90°	87	80	86	168	140	140
105°	87	87	76	168	144	144
120°	80	87	86	170	144	144
135°	87	79	84	168	144	144
150°	87	87	78	170	144	144
165°	79	87	84	168	142	142

is in sky coordinates allows one to construct a scaling to take the focal plane coordinates to sky coordinates. A global rotation can then be applied to match the observed sky coordinates. This global rotation does not take into account smaller position and rotation angle distortions caused by the optical chain. We recover these optical distortions in the final step of the modeling process.

In the time forward sense, our Code V model propagates a point on the sky to the focal plane. Each point on the sky is referred to as a 'field'. Figure 2.3 shows a single field ray trace. This single field is centered in focal plane coordi-

nates.

Code V allows a user to set up to 25 input fields at a time. The software traces each of the 25 input sky fields through the reflectors and lenses back to the feed horns. The final ray trace provides a mapping between the coordinates on the sky and position on the focal plane. The point spread function (PSF) for each field is then computed, returning the PSF centroid relative to the chief ray coordinates returned by the real ray trace. The locations of each PSF centroid are combined with the real ray trace results to form a final focal plane coordinate per input field. The 25 fields are then fit to a 2D quadratic in x and y, shown as $f(x, y)$ in Equation (3.1), where x and y are in focal plane coordinates. This produces two functions to transform focal plane coordinates to sky coordinates, one for x_{sky} and one for y_{sky}.

$$f(x, y) = A + Bx + Cy + Dx^2 + Exy + Fy^2 \tag{3.1}$$

These fits are then used to propagate each feedhorn location to the sky. The x_{sky} and y_{sky} fit parameters for each array and frequency can be found in Table 3.5. This incorporates any optical distortions on the positions caused by the ACTPol optics to 2nd order and is a clear improvement over a simple scaling. To illustrate the effect of these optical distortions Figure 3.1 shows the "lab coordinates" for the detectors in the first AdvACT mid-frequency array (MF1 or PA5) on the left. Computing the ray trace and using the fit functions of the form in Equation (3.1) brings these coordinates to those shown on the right.

Given the focal plane coordinates for each feedhorn in an array we propagate those coordinates to the sky and perform a least squares minimization, allowing a global translation and rotation but no shear, to match the modeled sky coordinates to those determined for each feedhorn by planet observations.

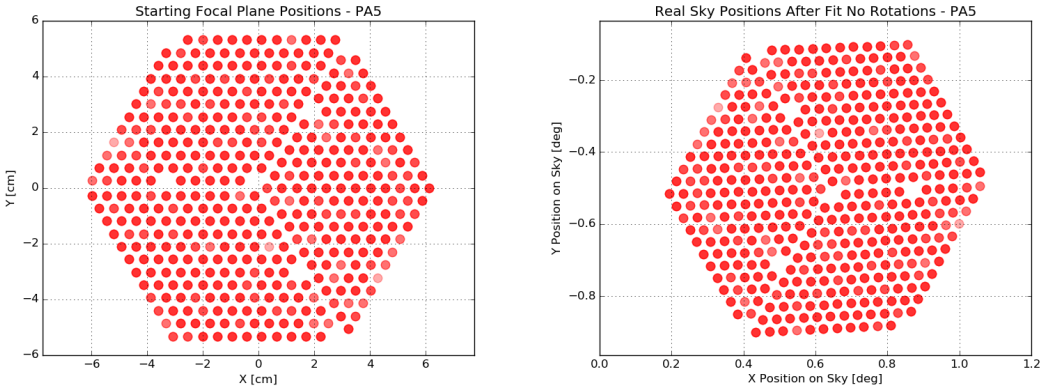

Figure 3.1: (Left): The starting detector focal plane positions for the AdvACT MF1 array (ar5). The coordinate system is referred to as the "lab coordinates" and represents the locations of the feedhorns on the focal plane. Each feedhorn has four optically coupled detectors. Gaps, or lighter colored circles indicate detectors that were not operational during planet observations which were used, among other things, to measure the detector sky position. The four large gaps in the center are due to mounting screws in the feedhorns. (Right): Detector feedhorn positions projected to the sky through the use of the Code V ray trace model. Optical distortions caused by the reflectors and lenses cause the slight rotation and displacements shown here. Also note the vertical and horizontal flip, perhaps most evident in the missing detectors on the outside edge of the focal plane. The vertical flip is by design, the horizontal comes from choice of lab coordinates.

This is done for each season, as differences between seasons such as the position of the secondary mirror, which is moved for focusing, and the position of the receiver, which has to be pulled from the telescope during upgrades, cause the detector positions relative to the boresight to change each season. This also means that they will differ compared to our ideal optical model.

Figure 3.2 shows plots of modeled vs observed sky positions for all six arrays in 2015 (for PA1/2/3) and 2017 (for PA4/5/6), along with their fit determined

installation rotation. Figure 3.3 shows a histogram of the differences in these positions for PA4 during the 2016 observing season. This shows we can model the position angle of each detector to better than $20''$.

Improvements to this might be possible by decentering the secondary mirror slightly, as the secondary position is optimized at the start of each season to produce the best beam. Preliminary studies of this in the model show a β decenter of -0.10 deg may decrease the average distance between the observed and modeled sky positions while maintaining roughly the same standard deviation. Decenters in α, x, y, and z can also produce reduced means, but typically at the cost of higher standard deviation. The effect of multiple simultaneous decenters has not been studied, and while reducing the difference between observed and modeled detector sky positions might be possible through perturbations of the model, we do not expect this to drastically change the resulting polarization angle either through rotation of the installation angle, or positional changes in the polarization model discussed in the next section.

A simple translation from focal plane to the sky can be accomplished using the plate scale, given in Table 3.2 for ACTPol in units of deg per cm. This can simply be multiplied by the detector positions in cm to yield degrees on the sky, and then recentered at the given array centers in the same table. Doing so, we can compare this simple scaling to our optical modeling by performing the same least squares minimization, which rotates the sky positions to match those from planet observations, and again computing the differences with observed and now scaled detector positions on the sky. Figure 3.4 shows a comparison of the scaling given the plate scale vs the detector sky positions determined from modeling for PA2. As can be seen in the figure, the Code V modeled positions

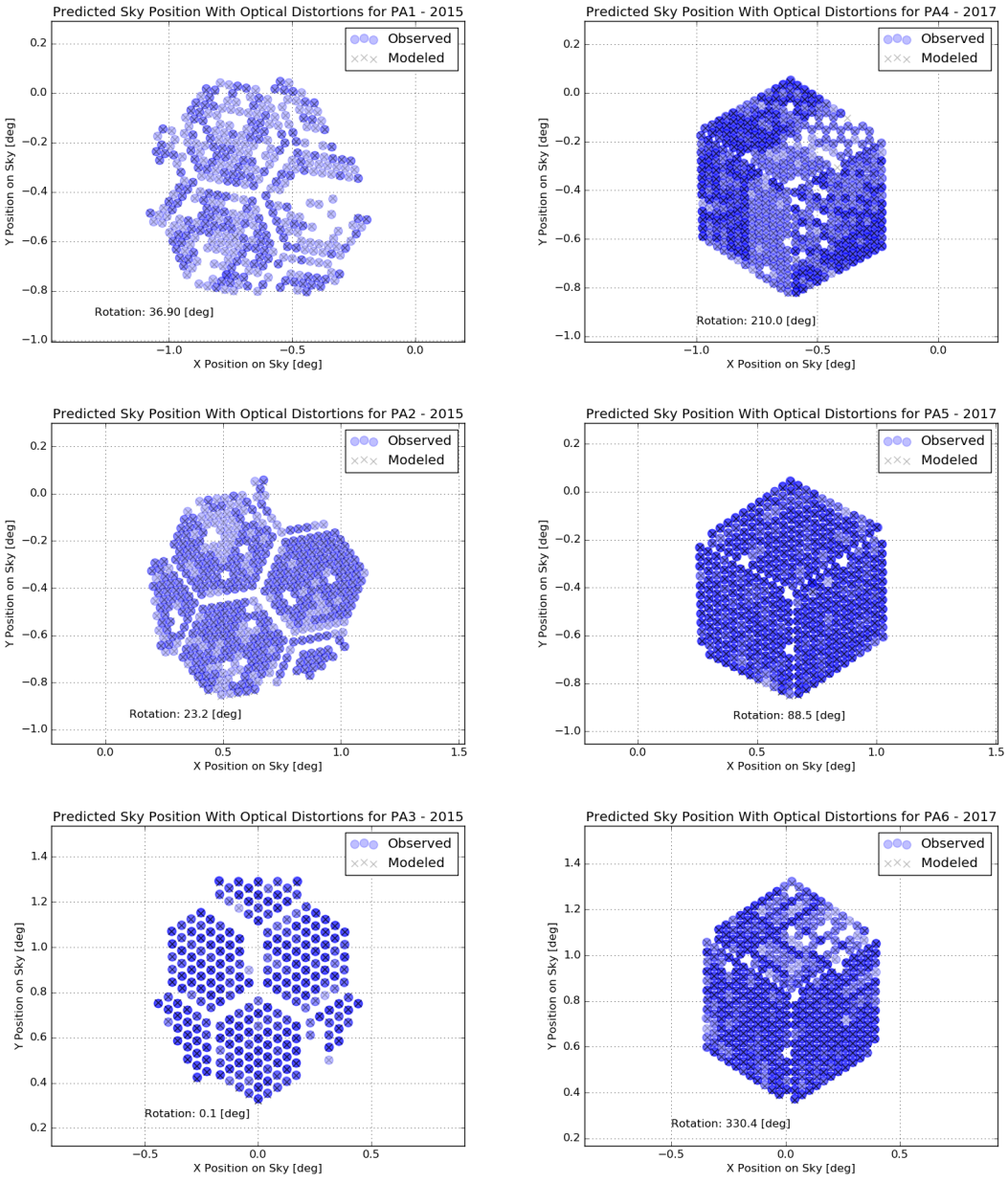

Figure 3.2: Observed vs modeled detector sky positions for PA1/2/3 (left column) and PA4/5/6 (right column), for the 2015 and 2017 seasons, respectively. The observed positions are plotted as circles with 25% alpha, so darker circles represent more live detectors in a given feedhorn. The modeled positions are marked with an 'X'. Ideally these line up with the center of the circles.

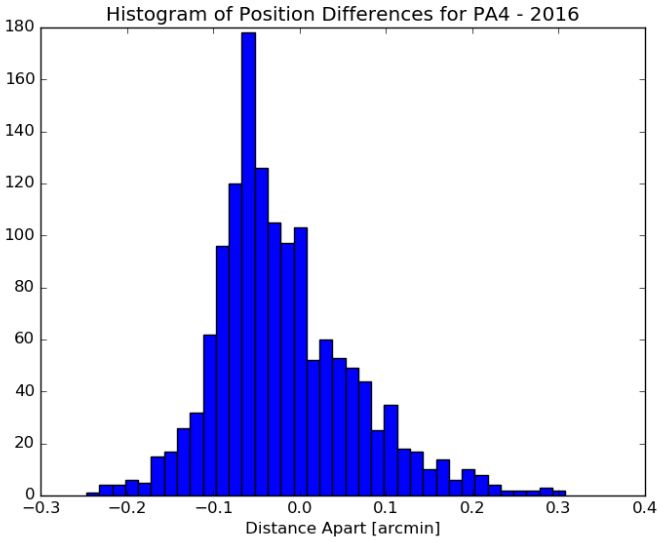

Figure 3.3: Histogram of position differences between observed and modeled sky positions for PA4 in the 2016 season.

Array	Array Center [deg]	X Plate Scale [deg/cm]	Y Plate Scale [deg/cm]
PA1/4	(-0.625, -0.48)	0.0722	0.0744
PA2/5	(0.625, -0.48)	0.0722	0.0744
PA3/6	(0.0, 0.75)	0.0693	0.0784

Table 3.2: Approximate plate scale for the ACTPol optical design. This provides a simple scaling to bring the detector focal plane to the sky. Array centers are given with respect to the telescope boresight.

better match the measured sky positions compared to those given by applying the plate scale, which does not capture the position distortions caused by the optics.

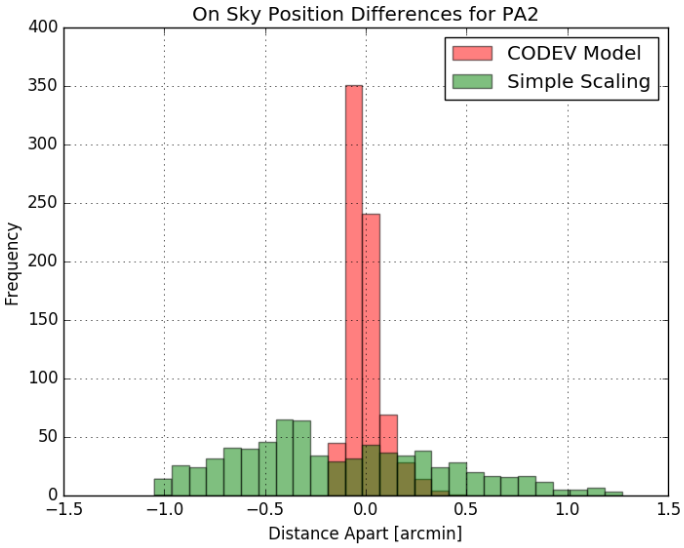

Figure 3.4: Histogram of differences between observed and modeled detector positions on the sky, calculated for a simple scaling based on the plate scale (green) and for the Code V ray trace, capturing optical distortions (red).

3.2 Polarization Sensitive Ray Tracing

Ray tracing is used to determine the installation angle. This combined with the lithographically determined detector angles makes up the bulk of the detector angle calibration. However, one last step is needed. Code V is capable of performing a polarization sensitive ray trace that can compute the transmittance at each surface from the Fresnel equations. We define the input polarization field to be identical for each sky trace and then use the poldsp MACRO[3] to calculate the polarization state for nineteen rays across the entrance pupil diameter. The output from Code V is in the form of the pupil averaged Stokes vector for each input field across the field of view of the telescope. From these we can

[3]poldsp is a user supplied MACRO written by members of the Physics Department at the University of Alabama, Huntsville which supplements the polarization output from Code V.

use Equation (1.14) to compute the polarization angle for each given field. The difference between the output polarization angle and the input angle gives the polarization rotation caused by the optics.[3]

This set of polarization rotations is used in another 2D quadratic fit using Equation (3.1), similar to what was done to transform the focal plane coordinates to sky coordinates. The fit results are then used to calculate the rotation associated with each feedhorn position on the focal plane. This is performed for the entire optical chain, producing the polarization rotations for each feedhorn, which are then combined with the initial angle and installation angle to produce a final calibration angle per detector. The fit parameters for each array and frequency can be found in Table 3.6. Resulting polarization rotations for each array are shown in Figure 3.5.

The left side of Figure 3.6 shows the resulting polarization rotation across the PA2 focal plane plotted in sky coordinates. To show the distribution of rotations due to just the telescope mirrors the right side of Figure 3.6 shows the polarization rotation at the telescope focus for PA2. This is shown as a function of frequency in Figure 3.8, and illustrates the importance of the anti-reflection coatings on the lenses.

3.2.1 Anti-reflection Coatings

Accounting for the anti-reflection coatings on the ACTPol optics is important in properly modeling the polarization rotation. The lenses are off-axis and thus influence the propagation of the polarization vectors through the camera ac-

[3]The same analysis can be performed with unpolarized input to model IP leakage. See Appendix C for a brief look at this calculation for ar2.

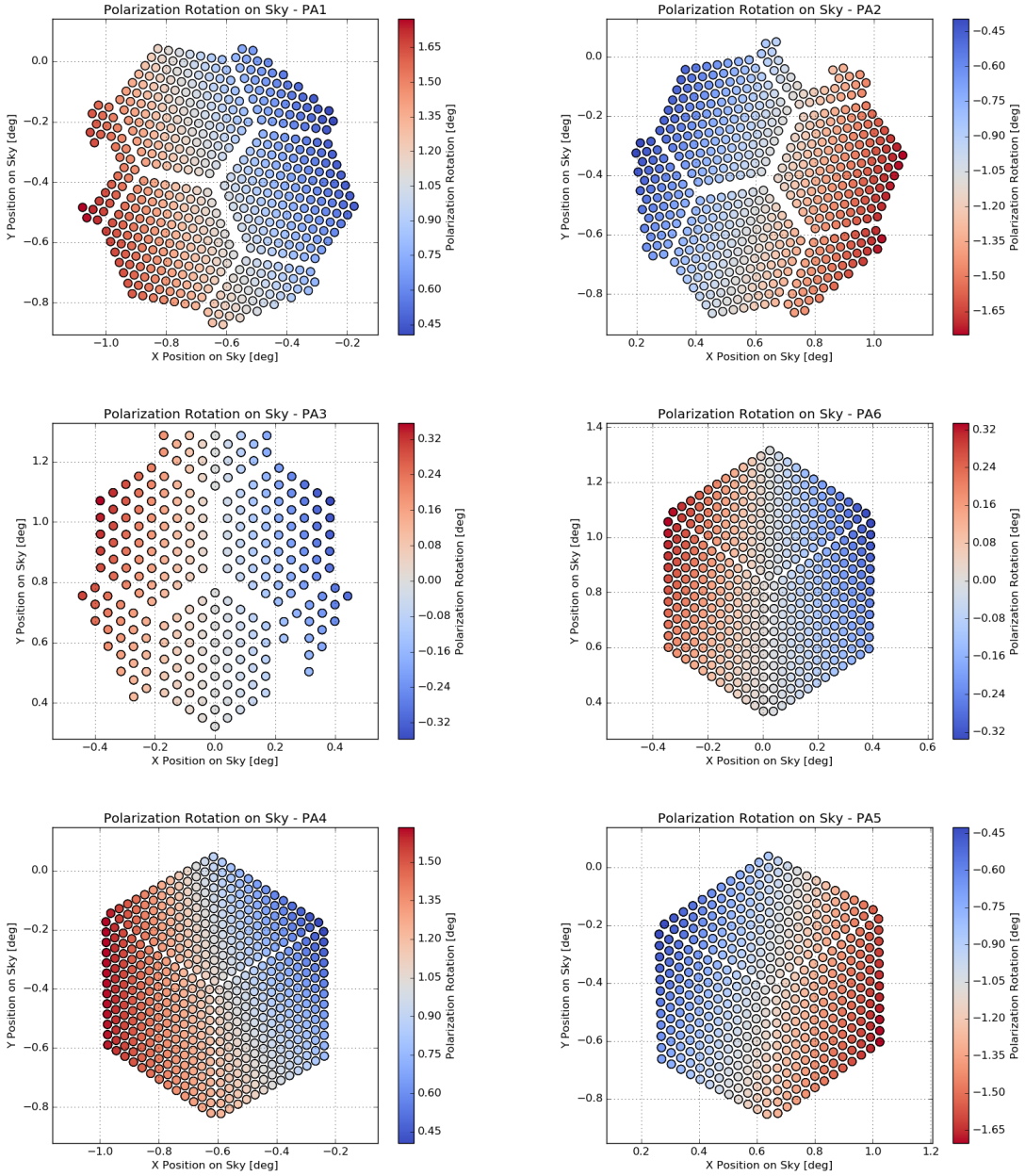

Figure 3.5: Modeled polarization rotation across all arrays. Shown for (left to right, top to bottom) ar1, ar2, ar3, ar6, ar4, and ar5, during the 2015 and 2017 season at 150 GHz.

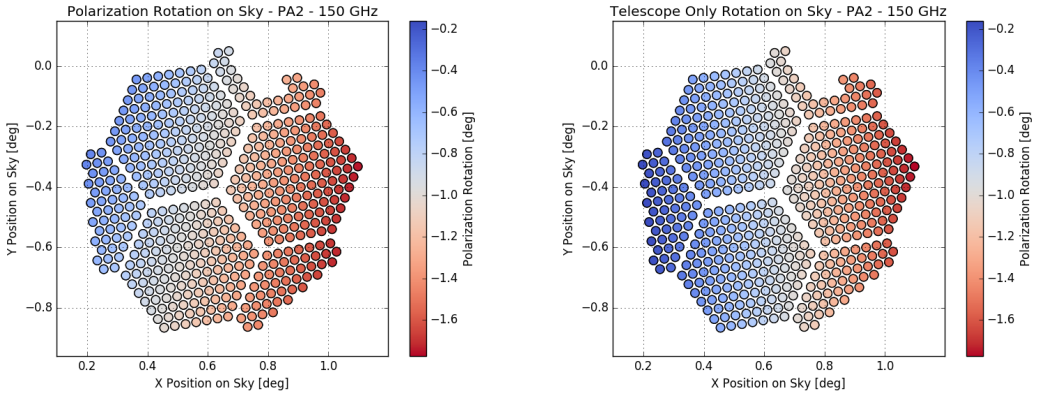

Figure 3.6: (Left): Polarization rotation across the PA2 focal plane for the entire optical chain at 146 GHz as determined by Code V, plotted in sky coordinates. (Right): Polarization rotation from the ACTPol reflectors only. The final surface in this calculation is the focus. Note that the reimaging optics introduce a rotation.

cording to their Fresnel coefficient. ACTPol uses multilayer metamaterial anti-reflection (AR) coatings on each lens in the optical chain [21]. These multi-layer coatings are entered in Code V using a multilayer coating definition file (MUL), defining their thickness and index of refraction. For the ACTPol coatings, we used physically measured thicknesses and HFSS simulated effective indices for the coating parameters. These parameters are shown in Table 3.3. The reflectance of the AR coatings as determined by Code V is shown in Figure 3.7.

Calculating the polarization rotation for many different wavelengths across the ACTPol science band shows the wavelength dependence of the rotations caused by the optics. Figure 3.8 shows this for PA3, the multi-chroic array in ACTPol. The polarization rotation is uniform across frequencies within the highlighted science bands, where the AR coating parameters are tuned for maximum transmission. Figures 3.6 and 3.8 show that the refractive optics reduce

Table 3.3: Coating parameters used to model the 2-layer and 3-layer anti-reflection coatings applied to the ACTPol and AdvACT lenses. The index of refraction for the silicon substrate is modeled to be 3.384 for all lenses [21].

	Thickness [μm]	**Index**
PA1/2	365	1.38
	200	2.50
PA3/6	470	1.28
	315	1.95
	245	2.84
PA4	296	1.23
	183	1.96
	153	2.82
PA5	500	1.29
	310	2.03
	258	2.92

the total range of polarization rotations in band across the focal plane.

3.3 Detector Polarization Angle Calibration

Working from the initial, lithographically defined, detector positions and polarization angles we apply the series of calibration rotations detailed above to form a final polarization angle calibration per detector for making maps of the CMB polarization. The final ACTPol detector angle calibrations are shown in Figure 3.9, with the marker shape indicating the physical detector angle and

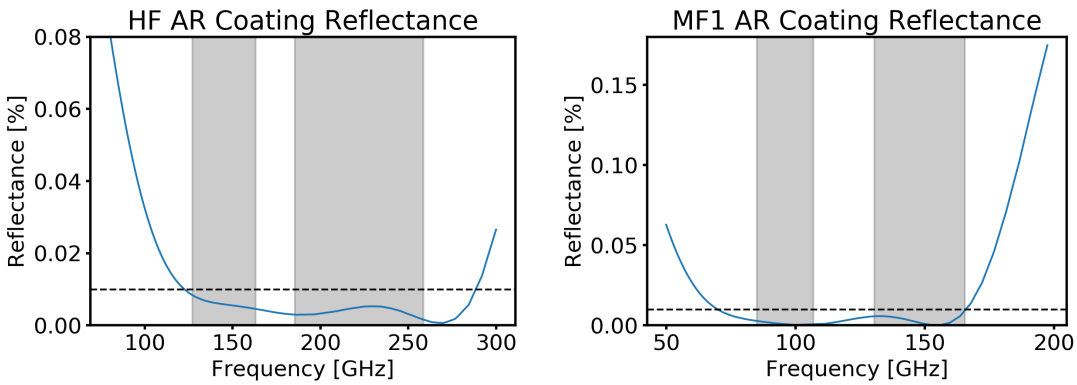

Figure 3.7: Modeled reflectance of the anti-reflection coatings for the HF (PA4) and MF1 (PA5) arrays. The gray bands indicate preliminary measured bandpasses for each array. The horizontal dashed indicate the target 1% reflectance for the coatings over the observation bands. Coatings are modeled with parameters shown in Table 3.3.

colors indicating the optically modeled polarization angle contribution. The final AdvACT detector angle calibrations for the HF and MF arrays are shown in Figure 3.10 in the same style.

This Code V angle, while small, has been critical in calibrating the detectors for ACTPol. Results published from the first season of ACTPol data used polarization angles derived from the prescription outlined in this Chapter, and checked the results by measuring the EB cross-spectrum. The EB nulling angle was found to be consistent with zero, $\delta\gamma_p = -0.2^\circ \pm 0.5^\circ$, implying that the polarization angle calibration by optical modeling works at the 0.5° level or better [76].

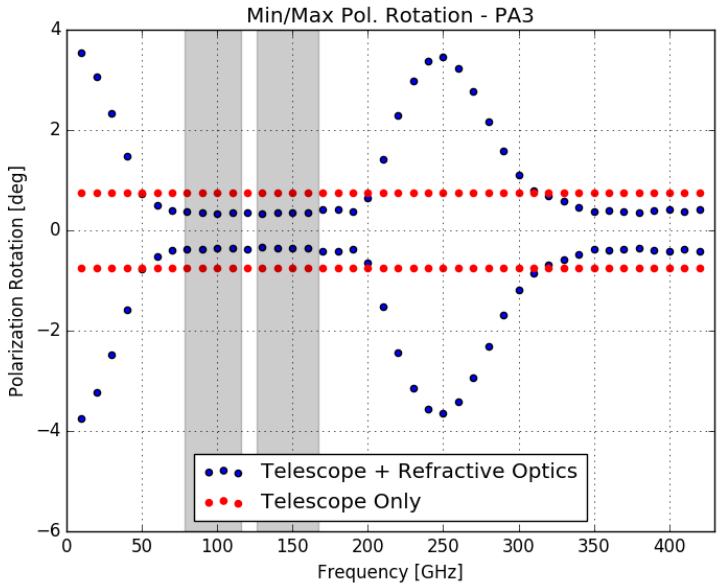

Figure 3.8: Plot of the minimum and maximum polarization rotations caused by the ACTPol optical chain as a function of frequency of the incoming light. Plotted in red are the minimum and maximum polarization rotation contributions from the telescope mirrors only, terminating at the receiver window. Plotted in blue are the minimum and maximum polarization rotations for the entire optical chain, including the anti-reflection coated silicon refractive optics. Highlighted in gray are the upper and lower science bands for CMB observations with PA3. Polarization rotation is similarly uniform across the science bands for PA1 and PA2.

3.3.1 Effect of Cryostat Perturbations on Polarization

Each season the cryostat is removed from the telescope, typically for upgrades to the detector arrays, but also sometimes for fixing cryogenic problems. We use photogrammetry to reposition the cryostat when it is put back into the telescope. This typically places the receiver back into its ideal position within 1 mm. To understand how any resulting decenter might affect the polarization angle calibration we perturbed the position of the cryostat in the optical model and

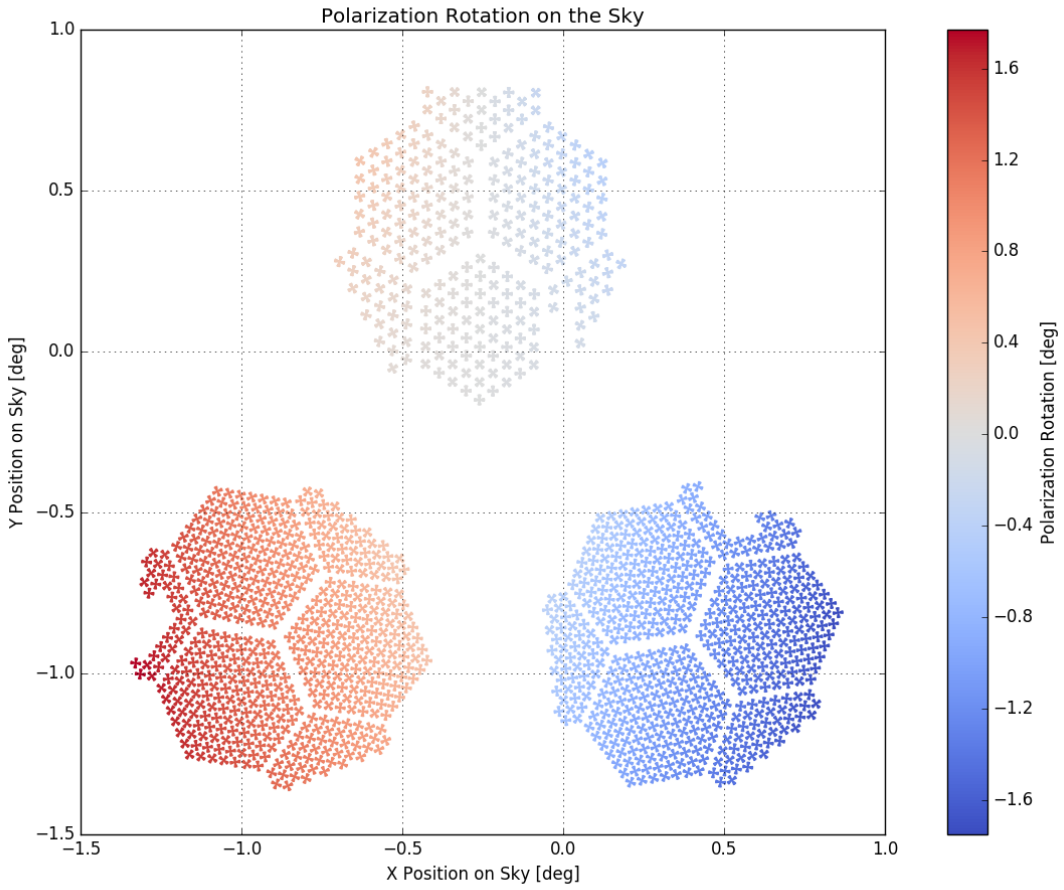

Figure 3.9: Plot of all three ACTPol arrays in sky coordinates. The angles of the plotted points correspond to the physical angle of the detectors in the telescope. The color scale corresponds to the additional polarization rotation caused by the ACTPol optics that is required to complete the angle calibration. This additional -1.7 to 1.7 degree rotation has been an important input to the detector angle calibration in published ACTPol results.

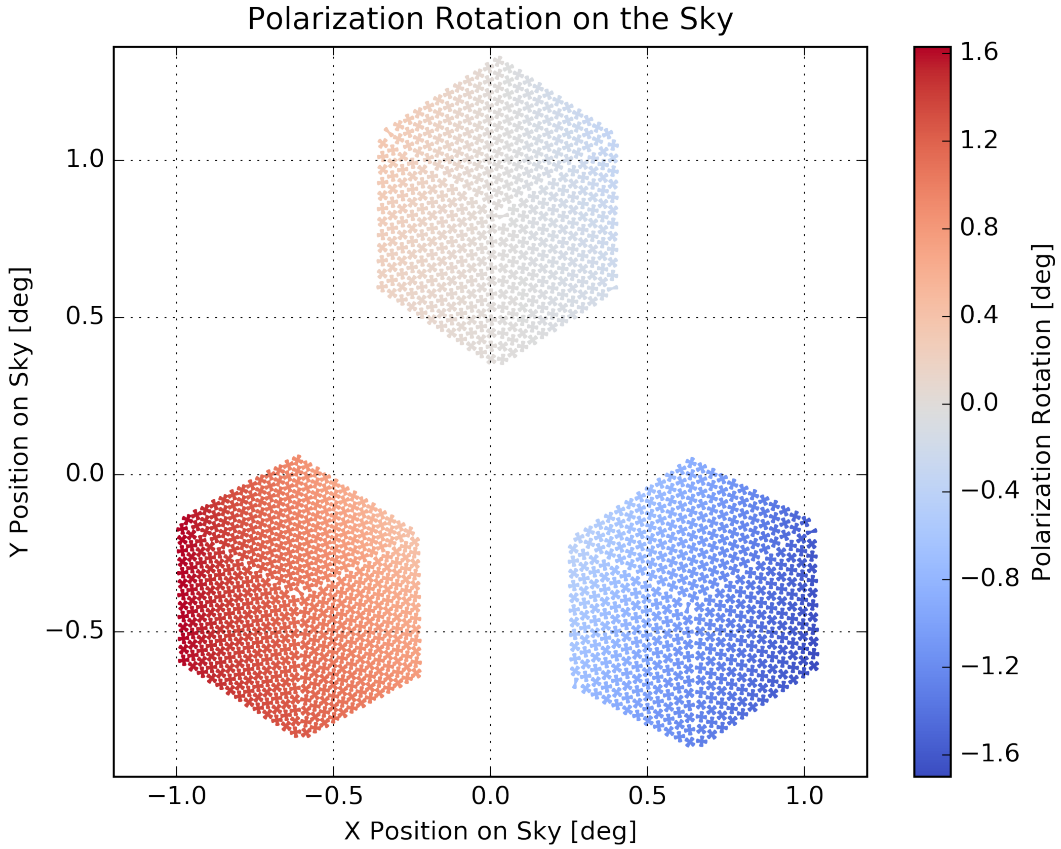

Figure 3.10: Plot of all three AdvACT arrays in sky coordinates. The angles of the plotted points correspond to the physical angle of the detectors in the telescope. The color scale corresponds to the additional polarization rotation caused by the ACTPol optics that is required to complete the angle calibration.

repeated the polarization angle study. We also perturbed the effective index of refraction of the anti-reflection coatings on the optics as well as their thickness in a separate study. The results are summarized in Table 3.4.

Figures 3.11 and 3.12 show the average change in the modeled polarization rotation given a perturbation of each parameter. Given the 1 mm tolerance in positioning the cryostat with the assistance of photogrammetry, the largest average rotation associated with a perturbation of the listed parameters should be

Perturbation	Slope	Units
X_c	-0.0877	deg/cm
Y_c	0.0069	deg/cm
Z_c	0.0051	deg/cm
α_c	-0.0312	deg/deg
β_c	-0.1050	deg/deg
ARC n	0.000289	deg/%
ARC t	0.000103	deg/%

Table 3.4: Average change in polarization rotation for perturbations around original optical design.

negligible (i.e. < 0.01 deg).

3.4 Automating Code V Analyses

Code V is a powerful program for the design and analysis of optical systems. However, use of the graphical interface becomes tedious for more intensive analyses. Code V provides a scripting language called "Macro-PLUS", which allows for expanding the capabilities of Code V. This language contains typical control structures, such as conditional branches, looping constructs, and user definable functions. However, the language is not very easily read, and the documentation is sparse.

The MACRO-Plus language is not interactive, and so needs to be written out into a 'sequence file' prior to execution. This sequence file is error checked before execution. When interacting with the graphical user interface (GUI) in Code V, the commands used by the GUI are output to a command line, allowing one to transcribe analyses easily into a sequence file. Taking this one step further, I wrote a python wrapper for these sequence files, which writes a se-

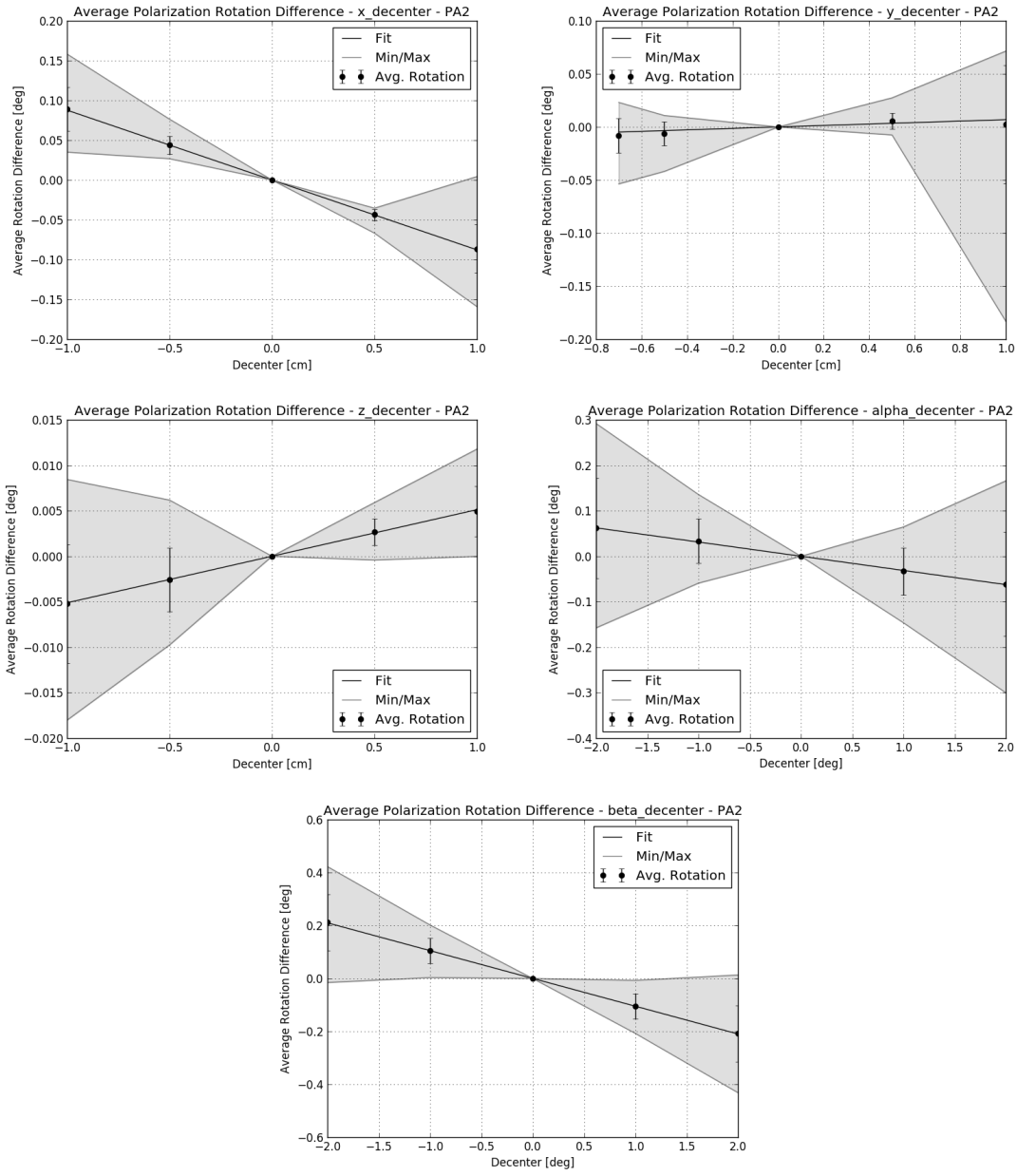

Figure 3.11: Effect of cryostat position decenters on the resulting polarization rotation from the Code V optical model. Data points are the average change in polarization rotation, with error bars showing the standard deviation. The gray outline shows the minimum and maximum change. The slopes for the linear fits are given in Table 3.4.

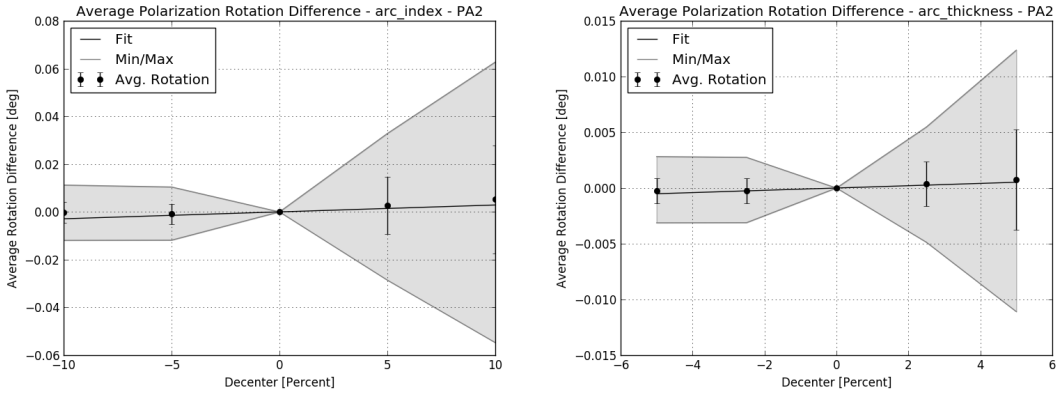

Figure 3.12: Effect of changes in the anti-reflection coating effective index of refraction and thickness on the resulting polarization rotation from the Code V optical model. Data shown in same way as Figure 3.11. Fit parameters given in Table 3.4.

quence file and calls Code V on the file. This allows a user to use features of a more mature programming language, Python, while interacting with Code V via Macro-PLUS.

This Python wrapper is available online [4]. The main Python package consists of a general class and several telescope specific modules, for use with the ACT, Simons Observatory, and CCATp telescope designs. These modules extend the general class, and allow a user to load an optical design and perform systematic studies of certain optical components.

The general class contains many methods that can be commonly used among the telescope specific modules. These include actions such as changing the wavelength of light used, setting the input fields, decentering surfaces, and much more. This class also handles much of the I/O required for using the code.

[4] https://github.com/BrianJKoopman/autov

```
actpol = autoact.AutoACT(ARRAY, descriptors=["calibration",
                                             "pa%s"%(ARRAY)])
actpol.create_header()
actpol.load_clean_len()
actpol.remove_glass()
actpol.apply_ar_coatings()
actpol.set_wavelengths(wavelengths=[int(autov.freq2lambda(int(args.frequency)))],
                                    reference=0)
actpol.set_fields(polarization=1)
actpol.set_vignetting()
actpol.activate_pol_ray_trace()
actpol.set_image_semi_aperture()
actpol.run_psf()
actpol.run_real_ray_trace()
actpol.run_poldsp(input_angle=0, pupil_number=23)
actpol.run_poldsp(input_angle=90, pupil_number=23)
actpol.exit()
actpol.run()
actpol.save_cfg(out_dir="../output/calibration/")
```

Figure 3.13: Example script written with autov. The script loads the ACTPol optical model, prepares several operations, such as applying the ACT anti-reflection coatings, setting the wavelength, performing a ray trace, and modeling the polarization rotation. These actions are saved to a sequence file. The script calls the Code V software and runs the sequence file it has generated, saving the results to text files, and exiting when complete.

The ACT module focuses on the study of polarization systematics in the optics. This allows users to manipulate optical elements, apply ACT specific multilayer coatings to surfaces, and to run ray traces and polarization analyses. This module was used for creating the ACTPol detector angle calibration described in this chapter. This code reduces the calibration procedure for a given array to the short 19 lines shown in Figure 3.13.

The SO and CCATp modules were built to explore tolerances on the position of optical elements, most of the functionality for which is provided by the general class. These modules simply contain commands to load these specific designs, with checks for making sure they are the original designs and for ma-

nipulating specific surfaces within these designs. More details on the tolerancing analysis performed for CCATp can be found in Appendix B.2.

These analyses, particularly the tolerancing, would be difficult to do by hand using the GUI. This automated approach allows for systematic studies, and organized file output. Most importantly it enables reproducibility in an environment where subtle changes can be made in the GUI that affect the outcome of one's analyses. Output file processing is another obstacle to overcome, as the output is often a non-standard format of raw ASCII, which is easily human readable, but can be challenging to parse pragmatically. This analysis is handled in separate code.

Array	Freq	Parameter	A	B	C	D	E	F
PA1	150	x_{sky}	6.3442E-01	7.1243E-02	-7.2364E-04	-1.0426E-04	-7.4634E-05	-2.0395E-05
		y_{sky}	5.0055E-01	-3.4049E-03	7.3495E-02	-1.3933E-04	-8.0223E-05	-2.3765E-04
PA2	150	x_{sky}	-6.3472E-01	7.1244E-02	6.9843E-04	1.0865E-04	-7.5323E-05	2.5732E-05
		y_{sky}	5.0025E-01	3.3708E-03	7.3507E-02	-1.3947E-04	8.5941E-05	-2.3925E-04
PA3	90	x_{sky}	-3.2543E-06	6.9052E-02	-5.5443E-08	1.0779E-07	-1.2223E-04	8.9339E-08
		y_{sky}	-7.3136E-01	4.9990E-07	7.8128E-02	-7.5660E-05	6.1601E-07	-1.8842E-04
PA3	150	x_{sky}	-7.3843E-07	6.9030E-02	1.6248E-07	-6.3292E-09	-1.2210E-04	4.2052E-08
		y_{sky}	-7.3139E-01	1.6846E-06	7.8140E-02	-7.5963E-05	1.5157E-07	-1.8823E-04
PA4	150	x_{sky}	6.3441E-01	7.1239E-02	-7.2214E-04	-1.0430E-04	-7.4248E-05	-2.0301E-05
		y_{sky}	5.0059E-01	-3.4047E-03	7.3482E-02	-1.3934E-04	-8.0455E-05	-2.3695E-04
PA4	220	x_{sky}	6.3439E-01	7.1233E-02	-7.2243E-04	-1.0429E-04	-7.4197E-05	-2.0300E-05
		y_{sky}	5.0057E-01	-3.4034E-03	7.3487E-02	-1.3914E-04	-8.0387E-05	-2.3711E-04
PA5	90	x_{sky}	-6.3451E-01	7.1185E-02	6.9049E-04	1.0903E-04	-7.2034E-05	2.4510E-05
		y_{sky}	5.0052E-01	3.3638E-03	7.3428E-02	-1.3933E-04	8.6838E-05	-2.3498E-04
PA5	150	x_{sky}	-6.3446E-01	7.1172E-02	6.9085E-04	1.0911E-04	-7.2088E-05	2.4441E-05
		y_{sky}	5.0049E-01	3.3626E-03	7.3436E-02	-1.3915E-04	8.6586E-05	-2.3529E-04
PA6	90	x_{sky}	-3.2543E-06	6.9052E-02	-5.5443E-08	1.0779E-07	-1.2223E-04	8.9339E-08
		y_{sky}	-7.3136E-01	4.9990E-07	7.8128E-02	-7.5660E-05	6.1601E-07	-1.8842E-04
PA6	150	x_{sky}	-7.3843E-07	6.9030E-02	1.6248E-07	-6.3292E-09	-1.2210E-04	4.2052E-08
		y_{sky}	-7.3139E-01	1.6846E-06	7.8140E-02	-7.5963E-05	1.5157E-07	-1.8823E-04

Table 3.5: Fit parameters for each array and frequency for propagating the x and y focal plane positions to the sky. Use with Equation (3.1) and plug in the focal plane position to determine sky position for a given feedhorn.

Array	Freq	A	B	C	D	E	F
PA1	150	1.0841E+00	1.0327E-01	3.1218E-02	5.6650E-04	-1.6828E-03	-4.1432E-04
PA2	150	-1.0887E+00	1.0358E-01	-3.1025E-02	-2.0344E-04	-1.5909E-03	4.1047E-04
PA3	90	-2.1139E-06	5.0388E-02	-1.6748E-07	-6.9555E-08	-4.8342E-03	1.6816E-07
PA3	150	-5.8462E-07	5.0758E-02	4.9062E-08	-1.8522E-07	-4.3994E-03	1.0625E-07
PA4	150	1.0902E+00	1.0025E-01	3.0531E-02	6.6612E-04	-6.7781E-03	-5.4268E-04
PA4	220	1.0809E+00	1.0346E-01	3.1681E-02	5.7343E-04	-8.7885E-04	-3.7433E-04
PA5	90	-1.0929E+00	1.0262E-01	-3.0660E-02	-2.3280E-04	-3.1289E-03	4.4687E-04
PA5	150	-1.0912E+00	1.0310E-01	-3.0735E-02	-2.1578E-04	-2.3341E-03	4.2822E-04
PA6	90	-2.1139E-06	5.0388E-02	-1.6748E-07	-6.9555E-08	-4.8342E-03	1.6816E-07
PA6	150	-5.8462E-07	5.0758E-02	4.9062E-08	-1.8522E-07	-4.3994E-03	1.0625E-07

Table 3.6: Fit parameters for each array and frequency for the polarization rotation in a given array. Use with Equation (3.1) and plug in the focal plane position to the amount of polarization rotation for a given feedhorn.

CHAPTER 4

DIRECT MEASUREMENT OF INSTRUMENT POLARIZATION

In Chapter 3, we showed our optical modeling based approach for calibrating the polarization angles of the ACTPol detectors. As a cross check to this model we attempted several direct measurements using a rapidly rotating polarizer. The idea is that a rapidly rotating polarizer can be used to put a sinusoidal signal onto the detectors. This sine wave can then be fit for its phase. The phase can then be used to determine the angle of each detector. This can be used for relative angle calibration. If the position and orientation of the polarizer is known well, this can also be used for absolute angle calibration, or, thought of in another way, for direct measurement of the polarization systematics present between the polarizer and the detectors.

Several iterations of polarizers were used for this measurement. The first iteration used an existing thin film polarizer from the Atacama B-mode Search (ABS) experiment. This provided enough motivation to improve on the design by making a new polarizer. This greatly improved our results, however was still not precise enough to use for calibration purposes. A third iteration was performed, moving from the use of thin film polarizers to free standing wire grids in collaboration with the University of California, San Diego.

The polarizers were placed near the entrance to the receiver. The input polarization is a combination of sky emission and reflected light from the receiver. The polarizers were rotated at a fixed frequency, modulating the signal on the detectors. This modulation can be fit, and a phase extracted. This phase can then be used to extract a polarization angle for each detector. This procedure is used to extract a per detector polarization angle and a consistency check be-

tween pairs of orthogonal detectors is performed. The per detector angle is then compared to the optics only polarization rotation as determined in CODE V.

In this chapter we discuss each iteration of these polarizers, their design, construction, and the resulting measurements, with Section 4.1.2 following along closely with [61].

4.1 Thin Film Polarizers

We used two different thin film polarization grids to directly measure the polarization angles of the detectors. These thin film polarizers consisted of a metalized film, laser ablated to form a grid of 'wires'.

4.1.1 ABS Aluminized Mylar Polarizer

The first thin film polarizer was a Mylar based thin film polarizer that originally was built for use on the Atacama B-mode Search (ABS) experiment [65]. This polarizer, fabricated on $6\,\mu\mathrm{m}$ thick Aluminized Mylar, had a pattern of $50\,\mu\mathrm{m}$ wide aluminum traces, on a $100\,\mu\mathrm{m}$ pitch. It was cut down to fit the $\sim$12 in diameter of the HWP mounts and glued, while held taut, to a thin piece of Zotefoam. The Zotefoam served as a substitute mounting point to be held within the half wave-plate (HWP) rotor, allowing the rotation of the Mylar polarizer with the HWP hardware. However, the Zotefoam, being quite flexible, was unable to retain the tautness of the grid that was applied in gluing. The result was that once mounted in the HWP rotor, the grid became loose and wrinkled. The gluing process and final mounting of the grid are shown in Figure 4.1.

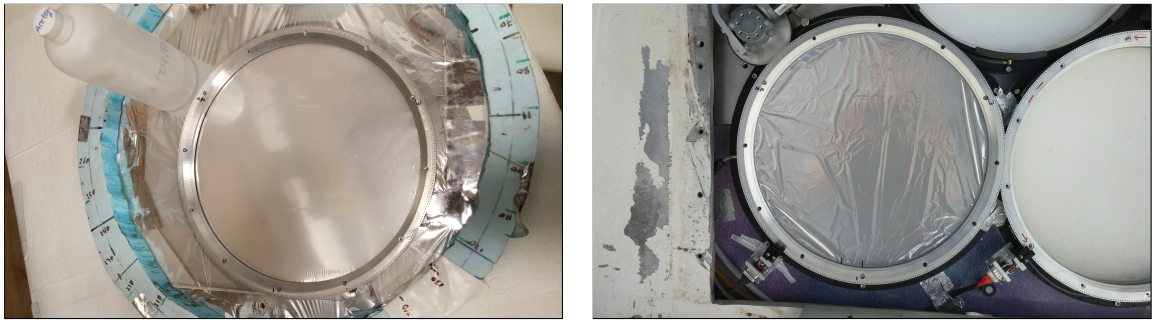

Figure 4.1: (Left): The ABS Mylar thin film polarizer mounted on a piece of Zotefoam with the ACT HWP rotor on top during the gluing process. Note the tautness of the polarizer, making a uniform surface. (Right): The thin film polarizer mounted on the face of the ACT receiver. The polarizer has lost tension after being cut from the original film, producing wrinkles across the film.

The HWP air bearing hardware was brand new in early 2015, when we first used the ABS thin film polarizer. The associated software for the encoder readout was not quite ready yet, so we ran without it, spinning the polarizer at 0.48 Hz without position readout during data acquisition. An attempt was made to align the grid with the home hole on the HWP encoder ring, however, since the optical encoder was not functional at the time of measurement we do not know the orientation of the polarizer during data collection.

We assess the quality of the data by comparing the relative offset between colocated, orthogonal detectors. Since these detectors are orthogonal, we expect them to be perfectly out of phase. Figure 4.2 shows an example segment of a pair of detector timestreams from orthogonal detectors. Qualitatively the timestream looks noisy, but out of phase. Subtracting the two phases for each pair of detectors we then plot a histogram of the phase differences, shown in Figure 4.3.

We then fit a Gaussian to the histogram, and find a mean phase difference

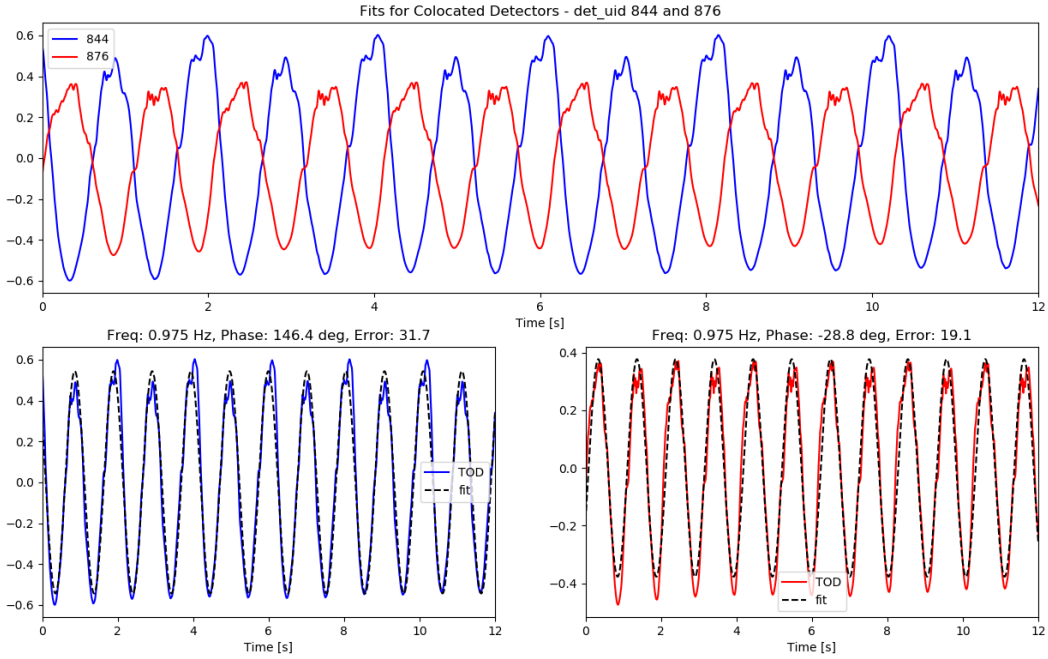

Figure 4.2: Example 12 second long segment of two timestreams from a pair of orthogonal detectors in PA2. The top panel shows the raw timestreams. They look approximately out of phase. The bottom two panels show the two timestreams separately, with a fit to a simple sine wave as a function of time shown as a dashed line.

of 183 degrees, with a standard deviation of 22 degrees. While this indicates the detectors are out of phase, there is clearly room for improvements. A primary goal in fabricating a new grid was making the grid uniform across the full aperture of the window.

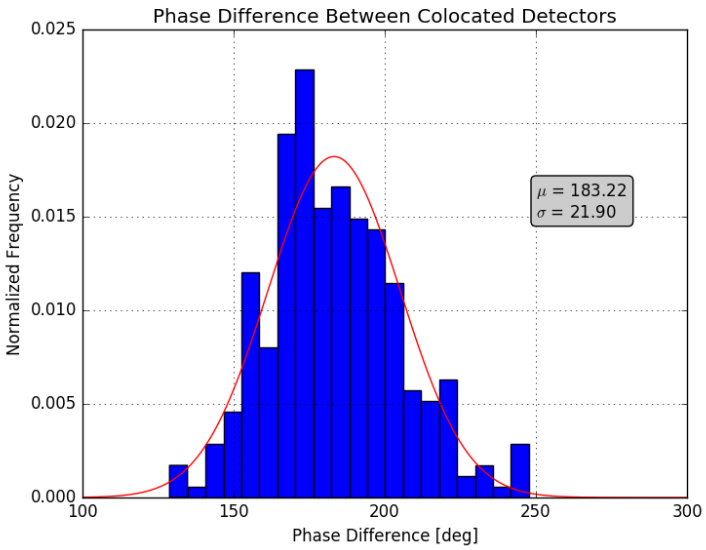

Figure 4.3: Histogram of the phase differences between colocated, orthogonal detector pairs in a timestream taken with the polarizer rotating at 0.48 Hz while installed on PA2. We expect this to be centered on 180 degrees, as the detectors should appear out of phase. We find a mean phase difference of 183 degrees, with a standard deviation of 22 degrees.

4.1.2 ACT Aluminized PET Thin Film Polarizer

While designing a new polarizer we considered the geometry of the ablated metal pattern and the resulting reflection and transmission properties of the film. A large, rapidly modulating, polarized signal on the detectors would drive the detectors into a nonlinear regime. With this in mind we explored different polarization grid geometries using CST Microwave Studio[4], varying the wire pitch and width for a given material thickness to produce a mostly reflective grid. This would produce a small polarized signal on the detectors so that they remain stable during measurements. Figure 4.4 shows the simulated reflectance of five different grid geometries, including the final fabricated geometry.

[4]https://www.cst.com/products/cstmws

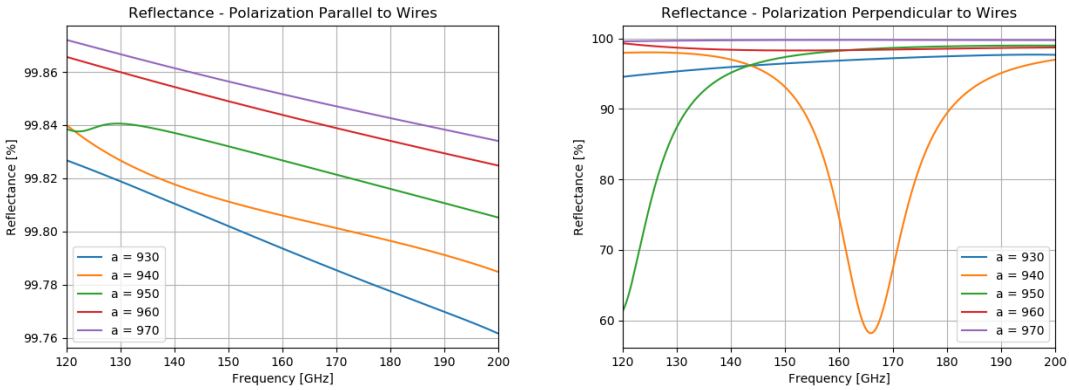

Figure 4.4: CST Microwave Studio simulations of the reflectance of polarized light parallel (left) and perpendicular (right) to the direction of the wires in the wire grid. These simulations motivated the design parameters for fabricating the thin film polarization grid. a here is the width of the wire on in microns on a $1000\,\mu\mathrm{m}$ pitch. The chosen design used $a = 950\,\mu\mathrm{m}$ which, according to the simulations, produces 97% reflection in one orientation and 99.8% in the other at $2\,\mathrm{mm}$ wavelength. The thickness of the wires is 30 nm.

The grid is a thin metal film on a PolyEthylene Terephthalate (PET) substrate, $12\,\mu\mathrm{m}$ thick (48 gauge), sourced from Dunmore Corporation[2]. The PET is fully metalized on one side with $30\,\mathrm{nm}$ of aluminum. The desired geometry is then made through laser ablation of the aluminum layer by PhotoMachining Inc.[1] Based on simulations in CST Microwave Studio, we chose a geometry of straight, parallel wires, $950\,\mu\mathrm{m}$ wide, on a $1000\,\mu\mathrm{m}$ pitch.

This produces a grid with 97% reflection in one polarization and 99.8% in the other polarization at $150\,\mathrm{GHz}$, as determined by CST Microwave Studio. We measured the reflectance of the grids to be $95 \pm 5\%$ reflective in one polarization, $90 \pm 7\%$ in the other polarization at 150 GHz using a custom reflectometer setup

[2]http://www.dunmore.com
[1]http://photomachining.com

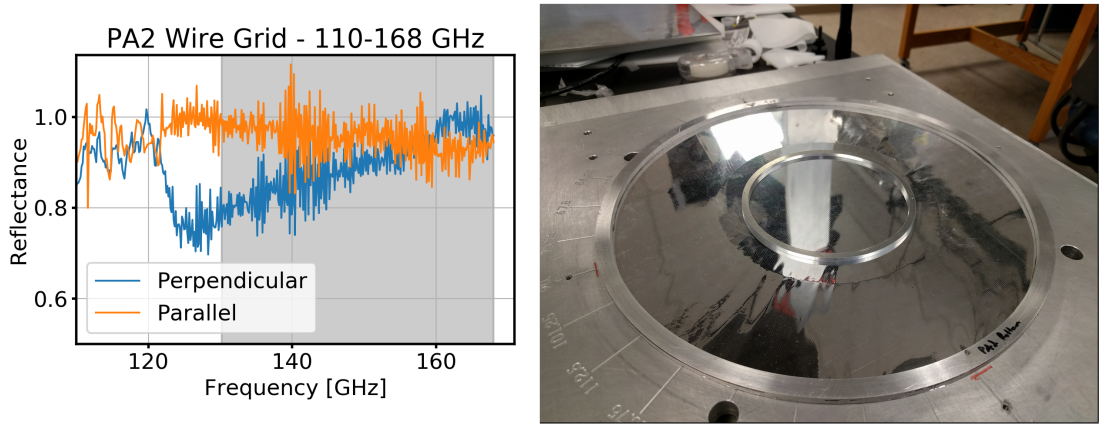

Figure 4.5: (Left): Measured reflectance of the PA2 thin film polarization grid from 110 to 168 GHz for two orthogonal polarizations, aligned parallel and perpendicular to the polarization of the source and receiver horns. The average reflectance across a $\pm 18\,\mathrm{GHz}$ band centered at 150 GHz is $95 \pm 5\%$ in one polarization and $90 \pm 7\%$ in the other. (Right): Photo of the thin film polarization grid during measurements in the lab at the University of Michigan, Ann Arbor.

at the University of Michigan. The measured reflectance and a photo of the setup at Michigan are shown in Figure 4.5.

The polarization grid was attached to a simple aluminum ring, the same thickness as the planned Advanced ACTPol half-wave plates, to fit into the half-wave plate mounting hardware. We built a simple mounting stand to attach the grid to the aluminum ring. Figure 4.6 (left) shows the polarization grid stand; the grid was securely attached to an aluminum panel with a circular cutout. The aluminum ring was then epoxied and raised into the PET side of the polarization grid (the aluminized side did not adhere well to the epoxy), providing tension while the epoxy set. Two polarization grids were successfully mounted using the test stand, one for each of the two 150 GHz optics tubes on ACTPol.

On Telescope Performance

The polarization grids were individually installed into the Advanced ACTPol half-wave plate mounts on the front of the telescope receiver. The half-wave plate mounting hardware contains an air bearing, allowing the mounted polarization grids to spin friction free. Coupled with an external motor the polarization grids were spun at 0.5, 1 and 2 Hz during measurements. Several sets of measurements were performed at these three constant rotational rates, rotating both clockwise and counter clockwise. During measurements the telescope remained stationary.

The right panel of Figure 4.6 shows one of the polarization grids installed on PA2, the second ACTPol array. With the grid rotating at a constant rate, the detectors see a sinusoidal signal. On short time scales the amplitude of the sinusoidal appears constant. Over the length of a single five minute measurement the amplitude varies with changes in the atmosphere. We only need to extract the phase from the sine wave in order to determine the polarization angles of the detectors. Before performing a fit to extract the phase we normalize and then band-pass filter the raw detector time streams with a 0.5 Hz wide Butterworth filter centered on twice the grid rotation frequency. The filtering damps low frequency atmospheric oscillations as well as high frequency harmonics.

We use the phase determined from the time stream fits to calculate the angle of each detector. Two detectors that are 180° out of phase are orthogonal, so the detector angles are calculated as their phase angle divided by two. The coordinate system for the measured detector angles is set by the angular position of the polarization grid at the start of a time stream. Without knowledge of the angular position of the grid, we globally rotate the determined angles rela-

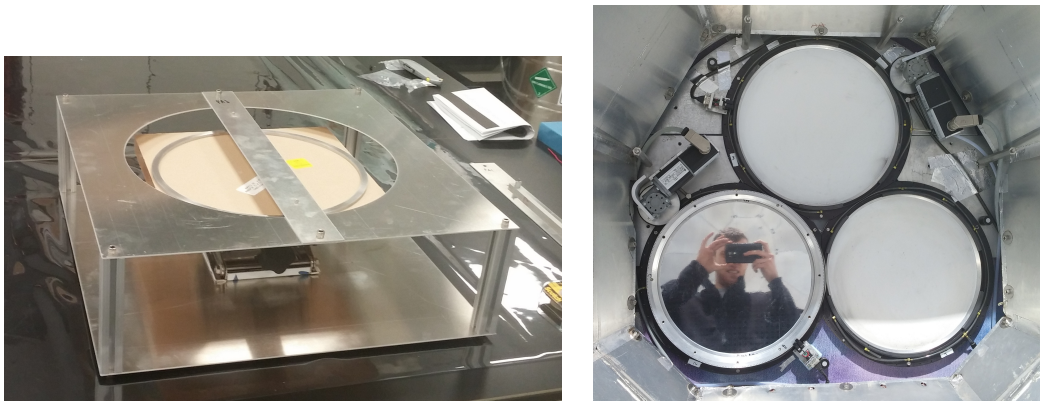

Figure 4.6: (Left): Polarization grid mounting and alignment stand. The polarization grid is taped taut across the round opening and aligned using the pictured cross bar using alignment marks on the grid to alignment holes on the aluminum mounting ring. The aluminum ring is epoxied and raised into the grid, making it taut and smooth. The epoxy is allowed to set and then excess material is removed. (Right): Photo of the front of the ACTPol receiver. The arrays are numbered 1-3 starting with the bottom right and moving clockwise. As pictured here PA1 and PA3 have nothing installed in front of them, PA2 has the thin film polarizing grid installed. The motor seen up and to the left of the polarization grid on PA2 rotates the grid which is floating on an air bearing. The encoder, in the bottom right, and the associated readout electronics (not pictured) record the angular position of the grid during rotation.

tive to a single reference detector's physical coordinate system determined by the optical modeling calibration without additional rotations due to the optics from CODE V. This zeros the measured angle for that single detector and makes all other measured angles relative to the chosen detector's local coordinate system. Figure 4.7 shows the physical angles of the detectors on the sky and the measured angles from the time stream fits.

We then subtract the measured relative angles from the physical angles of the detectors in the receiver. This produces a measurement of polarization rotation

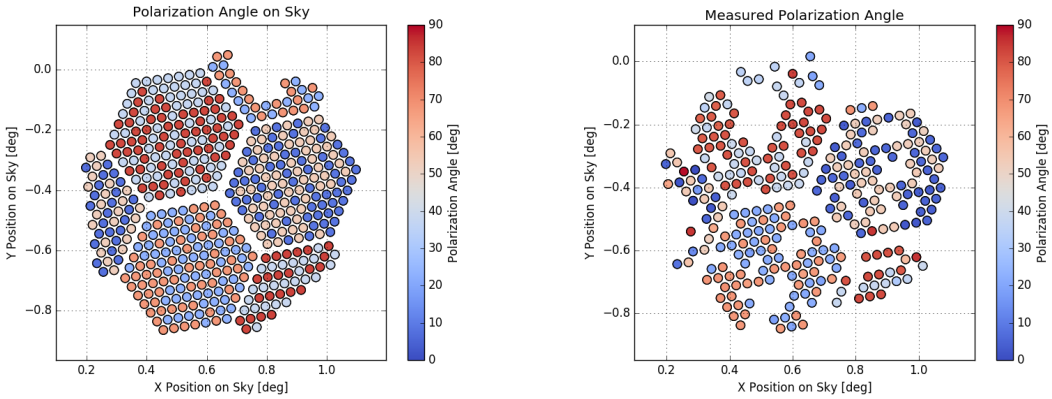

Figure 4.7: (Left): Physical detector angles for each detector pair projected on the sky. The color bar describes the angles of one of the detectors in each feedhorn, the other detector being orthogonal to the one plotted. (Right): Measured polarization angles from the polarization grid data sets. Like in the left panel, each circle represents a feedhorn which contains a pair of detectors orthogonal to one another. The color bar describes the angle of a single detector in the feed. Feeds are missing here, causing gaps when compared to the left panel, if they are missing a single detector in the pair due to less than 100% yield in the array.

due to the optics. This can be illustrated by subtracting the two plots in Figure 4.7, which results in the left plot of Figure 4.8. Based on modeling in CODE V, the polarization rotation appears to be independent of input polarization angle, so we then average the measured polarization rotation determined for colocated detectors, which gives a measured polarization rotation per feedhorn. We again rezero by removing the averaged phase for our selected feedhorn from all feeds. The polarization angles can then be explored by selecting different zeroing detectors across the focal plane.

The results relative to one reference detector are shown in Figure 4.8. For the selected reference detector coordinate system the average difference from the

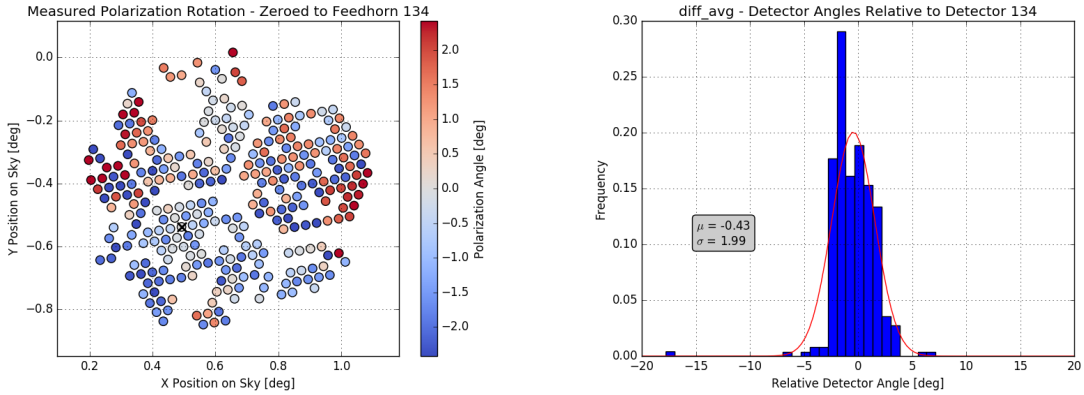

Figure 4.8: (Left): Measured polarization rotations relative to detector 134, marked with an 'X' on this plot. (Right): Histogram of average detector angles relative to detector 134 and its colocated partner, which are used as a reference.

physical angles for all the detectors across the focal plane is -0.4 ± 2 degrees. The mean is dependent on which detector we choose as a reference, while the standard deviation, which we report as the measurement uncertainty for each detector, is independent of the choice of reference.

This new polarizer was a dramatic improvement over the ABS polarizer, however there were several potential improvements that were identified on this first set of polarization grids. When fabricated, the grid was ablated in small, roughly 1" by 1" square sections. While many sections are aligned, some are misaligned by as much as $\sim 25\,\mu\mathrm{m}$. This means the wires are not uniformly straight across all areas of the grid. This may contribute to the differences between the modeled vs measured behavior in Figures 4.4 and 4.5. It is evident that the uniformity of the grid greatly affects our ability to determine the detector angles. Defects in the wire alignment at a constant radius but rotated by 90° may lead to the observed differences in the measured relative angles of colocated detectors, which show minimal differences in modeling.

Defects in the grid can also arise in mounting. Imperfections in mounting manifest themselves as wrinkles across the grid. Coupled with small vibrations from the surroundings (i.e. wind, the HWP motor) these wrinkles affect the signal propagating to the detectors, limiting our ability to determine the polarization angles. Efforts to improve the uniformity of the grid fabrication led to the use of free standing wire grids.

4.2 Free Standing Wire Grids

After the publication of [61] a discussion began with our Simons Observatory Collaborators at the University of California San Diego (UCSD), the product of which was collaboration on the production of several large diameter free standing wire grids for use in repeating the polarization measurements done with the aluminized PET thin film polarizer.

The group at UCSD already possessed an automated machine for winding wire grids, shown in Figure 4.9, which was designed to make wire grids with a circular 11.4 cm diameter. It was also capable of winding grids on a elliptical frame with a 20 cm minor axis. I worked with the UCSD group to modify their grid winding equipment to accommodate winding a circular wire grid with an outer diameter of up to 26.1 cm.

The wire grids are made from $25\,\mu\mathrm{m}$ diameter Tungsten wire, wound on an aluminum frame which clamps around the grid winder motor. This frame has a 26.7 cm clear aperture. The winder applies a constant 15 gram-force of tension to the Tungsten wire while the frame rotates. The wire feed moves along the frame, spacing the wire on a $100\,\mu\mathrm{m}$ pitch. Once the winding is complete, the

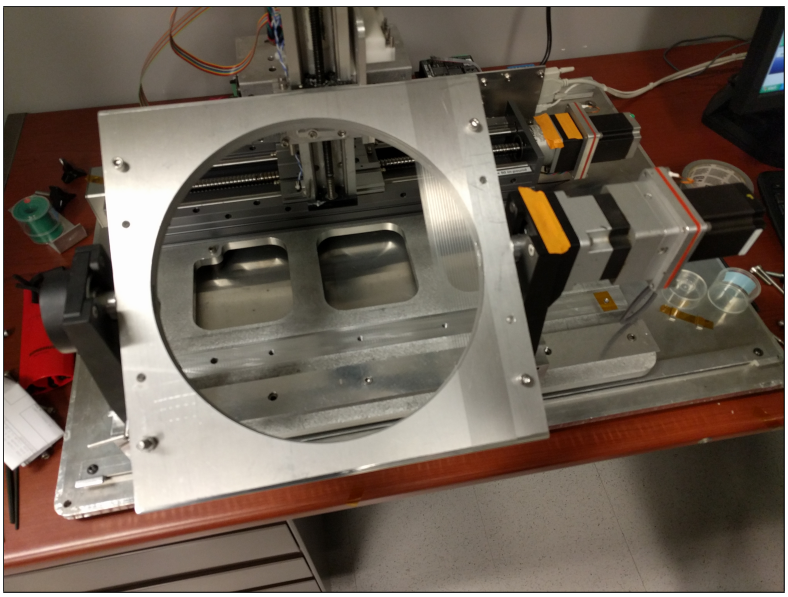

Figure 4.9: A photograph of the wire grid winding machine at UCSD with a large frame for winding the 26.1 cm outer diameter wire grids mounted. A wire grid pair is starting to be wound as can be seen near the right end of the frame.

wire grid is transferred to a circular ring by epoxying the grid to the ring and cutting off the excess wire. This permanently affixes the wire to the circular ring. The circular ring can then be mounted to an adapter plate, which fits in the HWP rotor in place of an actual HWP. This adapter plate can be seen in the right photo of Figure 4.10.

The first circular ring we used was made from Aluminum 6061. The ring was a quarter inch thick and had an outer diameter of 26.1 cm. The inner diameter was 23.5 cm. There is a small groove running along the ring for the epoxy, and 8 mounting holes equally spaced around the ring. This aluminum frame was thought to be sufficient for holding the wires, however, due to the 15 gram-force per wire, totaling 40 kilogram-force on the frame, the frame deformed enough to cause the wires to loose tension. This tension loss is small, but enough to cause

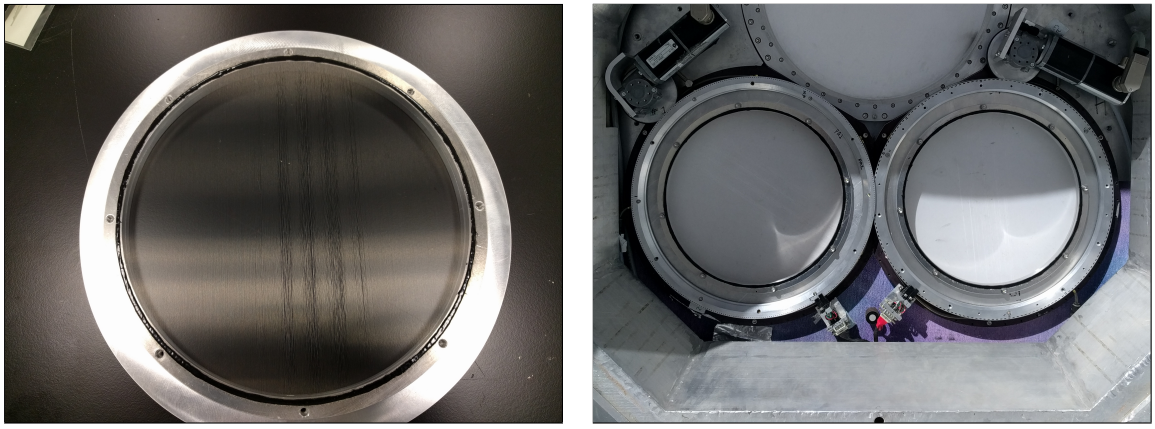

Figure 4.10: (Left): Photo of one of the first 26.1 cm diameter wire grids on an Aluminum 6061 frame. The non-uniformities in the center of the grid are caused by the frame deforming enough that the wires lose tension. (Right): Photo of the two wire grids mounted on aluminum frames deployed on the telescope. The tension loss can be seen in both grids.

the center wires to sag, changing their spacing to between zero and a factor of five times larger. This defect is evident in photos shown in Figure 4.10.

This factor of five wire spacing increase in the center of the wire grid is not ideal. The reflectance of the grids will be affected by this defect. Figure 4.11 shows the reflectance and transmittance as a function of frequency for various configurations of wire spacing with a fixed wire diameter of $12.5\,\mu\mathrm{m}$. The $100\,\mu\mathrm{m}$ case has nearly perfect reflection across the frequency range from 50-300 GHz. With increasing wire spacing, the reflection drops to as much as 52% at 150 GHz for a wire spacing of $500\,\mu\mathrm{m}$. In addition, without tension on the wires the spacing may vary during the measurements, which could significantly degrade the data quality.

While we still performed the wire grid measurements with the defective wire grids on aluminum frames, we sought to improve the grid uniformity, as non-

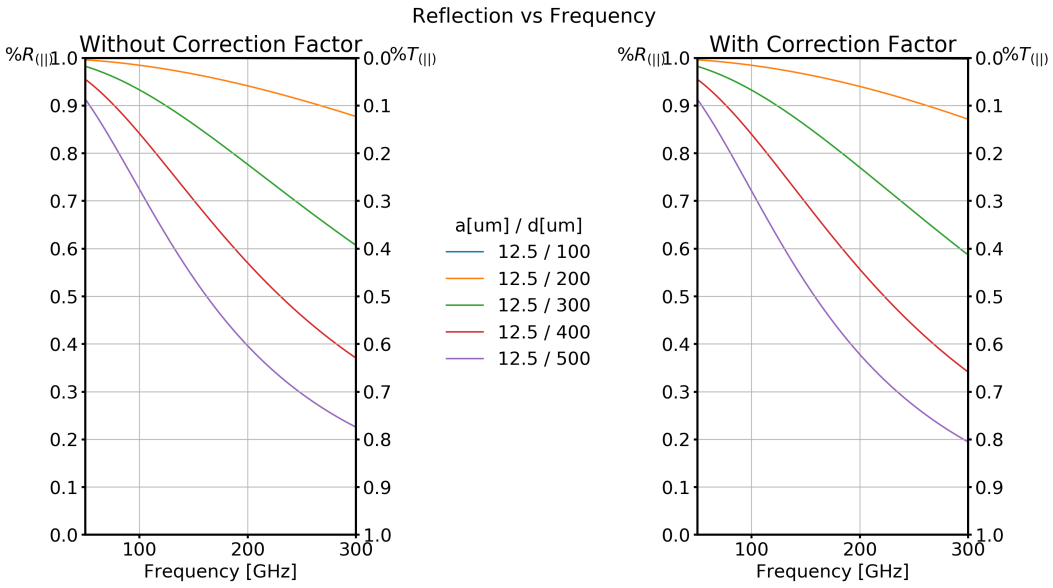

Figure 4.11: Plot of reflection and transmission model as a function of frequency for wire grids made from a wire with radius, a ($12.5\,\mu$m), and a pitch of d ($100 - 500\,\mu$m) [98]. The plot is reproduced twice, once with, and once without a correction factor to the current induced in the wire, also given by [98] and originally derived in [73]. This figure was generated using code written by Paul Corlies.

uniformities in the original thin film polarization grid were the primary motivation for moving to a free standing wire grid. We explored using different materials for the wire grid frame as well as modifying the original frame's dimensions to improve its strength. Using the SOLIDWORKS SimulationXpress basic finite element analysis (FAE) tool, the strength of these modified frames was studied. We explored the following configurations:

- the original design, but with Steel 304,
- increasing the frame thickness to 0.4 in, both in Al 6061 and Steel 304,
- decreasing the inner diameter to 9.0 in, both in Al 6061 and Steel 304,

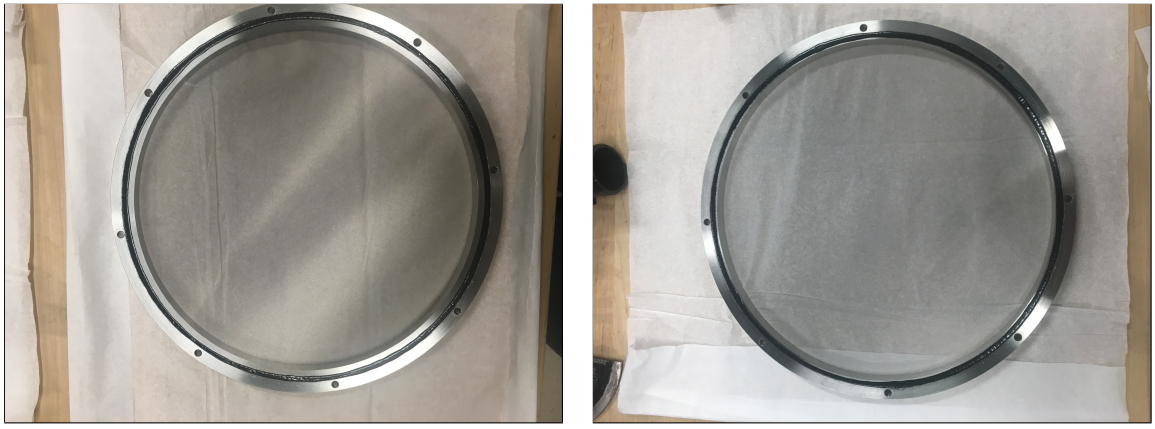

Figure 4.12: (Left): Photo of a 9 in clear aperture wire grid mounted on a 304 Stainless Steel ring with no tension loss. The grid frame has an outer diameter of 26.1 cm and a thickness of 0.4 in. (Right): Photo of a 23.5 cm clear aperture wire grid mounted on a 304 Stainless Steel ring with no tension loss. The grid frame has an outer diameter of 26.1 cm and a thickness of 0.4 in.

- simultaneously increasing the frame thickness while decreasing the inner diameter, both in Al 6061 and in Steel 304.

Of these configurations the FEA showed the strongest to be, unsurprisingly, the frame with both dimension modifications made from Steel 304, showing an ~ 8.4 reduction in displacement from a force exerted on the frame in the direction of the taught wires. However, this weighed six times more than the original aluminum frame, weighting a little over 2 lbs. Since weight was a concern for the air bearings that support the grids, we chose to make two different frames (since grids are always made in pairs). The second frame only increased the thickness to 0.4 in, keeping the original inner diameter of 23.5 cm. This cut a quarter of a pound, and was still ~ 4.7 times stronger than the original frame according to the FEA.

Winding a new set of grids and transferring to the new grid frames, made from 304 Stainless Steel (which is slightly weaker than 304 Steel), the grid frames held tension. Figure 4.12 shows both variations of the 304 Stainless Steel grid frames which show no loss of tension in the wires. These grids were brought to the ACT site and measurements repeated.

4.2.1 Wire Grid Timestream Analysis

Throughout the time we used the thin film polarizers we did not have the encoder readout working, primarily due to software problems. The encoder readout electronics were upgraded at one point as well. Typically these measurements were done at the start or end of a season, which tends to be when other upgrades/changes happened, often resulting in non-working HWP encoders. We proceeded with measurements without encoder readout because we thought we could at least get a reasonable relative calibration, as we were fitting the timestreams to a sine wave as a function of time,

$$y(t) = a\sin(2\pi f t + \phi). \tag{4.1}$$

This, we eventually found, led to difficulties with extracting the phase.

The data looked promising, especially when compared to early measurements, a raw timestream segment is shown in Figure 4.13. We determined the phase for each detector by first removing the mean of each timestream and normalizing the data. This prevented the fitting routines from running away with their parameter estimation algorithms. We fit simultaneously for amplitude, frequency, and phase in Equation (4.1). Initial parameters were set to one for amplitude, since we normalized the timestreams, the peak frequency found in a

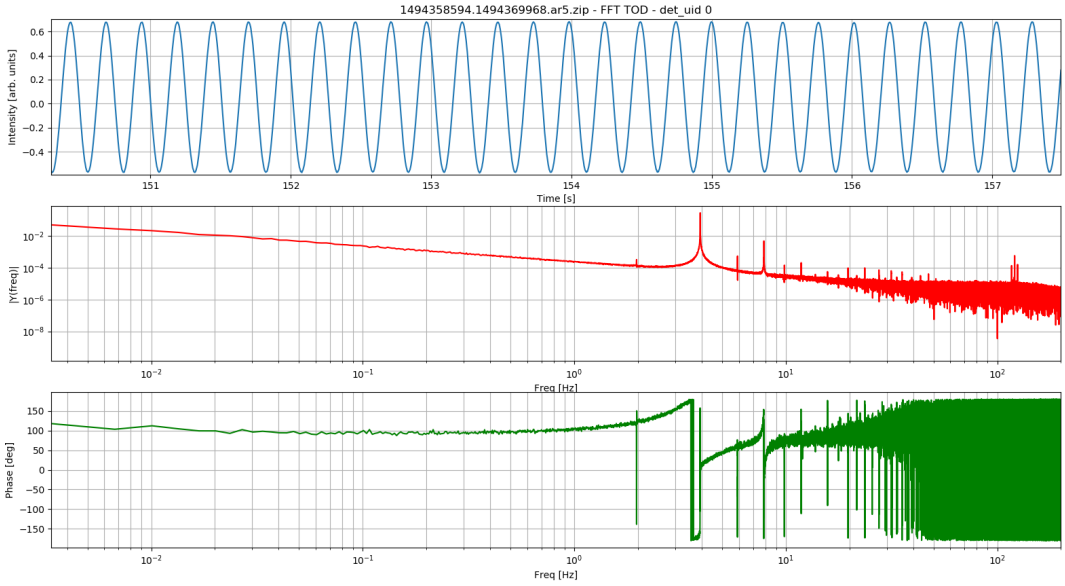

Figure 4.13: Example timestream segment from a steel ring mounted free standing wire grid. The timestream is unfiltered. The entire timestream lasts five minutes, though the top panel only shows about 8 seconds. The middle panel shows the Fourier transform of the entire timestream, and the bottom panel shows the phase as determined by the FFT.

Fourier transform of the timestream, and a phase offset based on the zero crossings in the timestream. We found that fitting for all three parameters, amplitude, frequency, and phase in Equation (4.1) worked well for some timestreams, but not all. It soon became apparent that there was some frequency offset resulting from the fit that was getting absorbed into the phase determination, as indicated by the $\delta(t)$ term in Equation (4.2):

$$y(t) = a\sin(2\pi ft + [\phi + 2\pi\delta(t)ft]). \tag{4.2}$$

We tried reducing the number of free parameters, keeping the amplitude fixed at one and (at times) the frequency fixed to the peak frequency in the FFT.

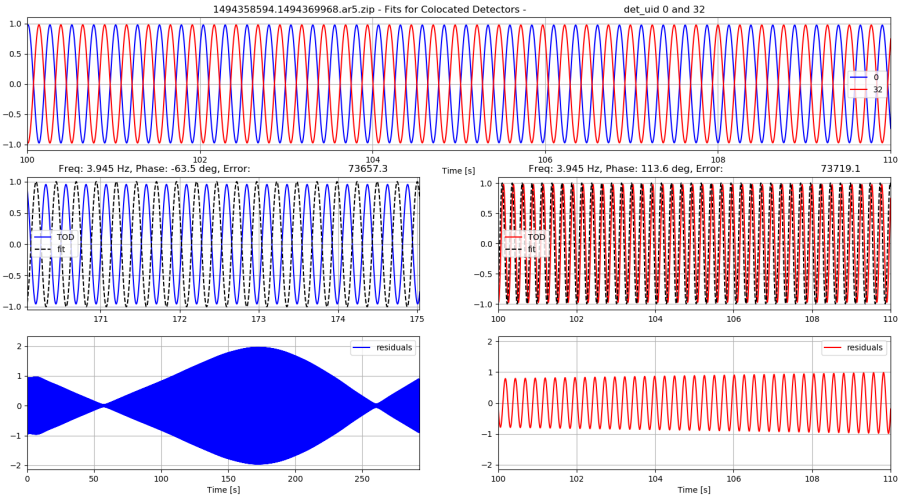

Figure 4.14: Example of pair of timestreams from colocated, orthogonal detectors with their associated fits. In these fits to Equation (4.1) the frequency and phase were allowed to vary. The top panel shows a 10 second segment of both timestreams, The middle two panels show the two timestreams with their fit plotted as a black dashed line. The bottom panels show the residual differences between the timestreams and their fits. The left panel showing the entire timestream.

However, we found that the fit would look good in one part of the timestream, but not in other parts, eventually moving perfectly out of phase. This is illustrated in Figure 4.14. The bottom left panel shows the residuals between the timestream and fit for one of the detectors. This shows the entire timestream. The amplitude of this residual shows how the fit moves out of phase with the timestream. The point where it is at a minimum, at approximately 50 seconds, the fit and timestream line up well, much like is shown in the red middle panel. However, where the amplitude is a maximum, around 170 seconds, the fit is completely out of phase with the timestream.

We believe this is due to the HWP drive motor not maintaining a constant

frequency and the failure of the fit model to capture this behavior. If we consider the actual timestream and the fit, given two sine waves, y_1 and y_2 with two similar frequencies, ω_1 and ω_2,

$$y_1(t) = \sin(\omega_1 t), y_2(t) = \sin(\omega_2 t) \tag{4.3}$$

If,

$$\Delta\omega = \omega_2 - \omega_1. \tag{4.4}$$

Then,

$$y_2(t) = \sin(\omega_1 t + \Delta\omega t). \tag{4.5}$$

The two waves become perfectly out of phase first when $\Delta\omega t = \pi$. This means our fit could be off in frequency by roughly,

$$\Delta\omega = \frac{\pi}{t} = \frac{\pi}{115[\text{sec}]} \sim 0.0273\,\text{Hz} \tag{4.6}$$

This is roughly 0.5% of the modulation frequency, and an even smaller percentage of the motor rotation speed (the motor being a much smaller diameter than the HWP rotor.) The fact that the motor/encoder hardware does not include a PID loop for maintaining a constant frequency coupled with the difficulty experienced fitting the data to Equation (4.1) motivated repeating the measurements with a working encoder readout.

With a working encoder readout we know the position of the wire grid. Instead of fitting Equation (4.1) we can now fit to Equation (4.7), which is fit as a function of angular position, θ, rather than time, avoiding the issue of a modulating frequency.

$$y(\theta) = a\sin(2\theta + \phi) \tag{4.7}$$

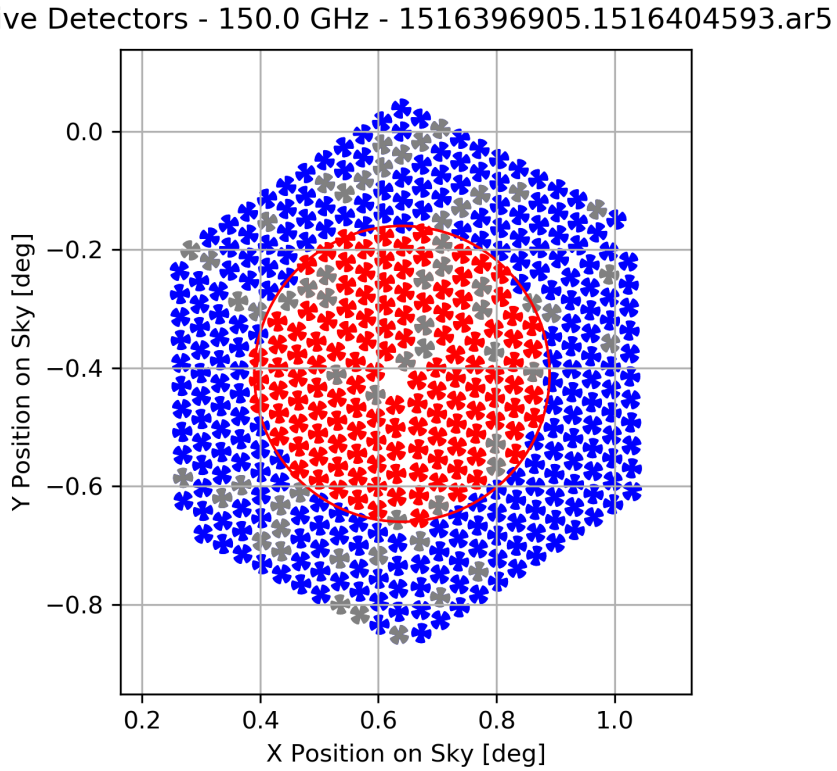

Figure 4.15: Operational detectors in ar5 during wire grid measurements. Red detectors are working detectors within a 0.25 degree radius, which we consider in the analysis, blue detectors are working detectors outside this radius, which we ignore. This plot shows the 150 GHz detectors.

Since the wire grid is a smaller diameter than the window, we restrict our view of the detectors to a circle of 0.25 degree radius, as shown in Figure 4.15. Before fitting we normalize the timestream and bandpass filter with a 0.5 Hz wide Butterworth filter centered at the $2f$ frequency. A filtered timestream is shown in Figure 4.16.

Fitting to Equation (4.7) we determine the phase of each detector. Figure 4.17 shows a 2 second segment of a pair of detectors from the timestream with their fits overplotted. This timestream had the wire grid rotating at 0.5 Hz, which

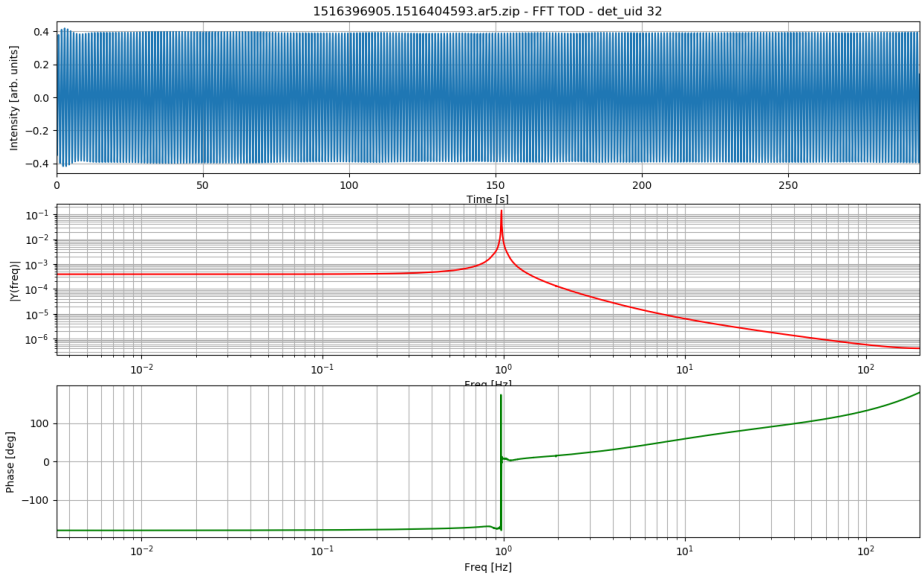

Figure 4.16: Example of a filtered timestream from ar5. The top panel shows the entire 5 minute timestream after filtering. The middle panel shows the frequency, note the lack of harmonics like those in Figure 4.13. The bottom panel shows the phase information from the FFT. This particular timestream is from detector 32.

shows up as approximately 1 Hz due to the symmetry in the grid.

Following the same procedure used for the thin film polarizer, we take half the phase determined from the fit as the detector angle. Since the start of the timestream is arbitrary, there is an arbitrary phase offset applied to all the detectors. To account for this we rotate the determined angles to match the angle of one of the detectors in the array for the comparison shown in Figure 4.18.

Zeroing to the selected detector, we can take the difference between focal plane angle and the measured angles, allowing us to map the polarization systematics in the receiver. The differences are mapped and plotted as a histogram

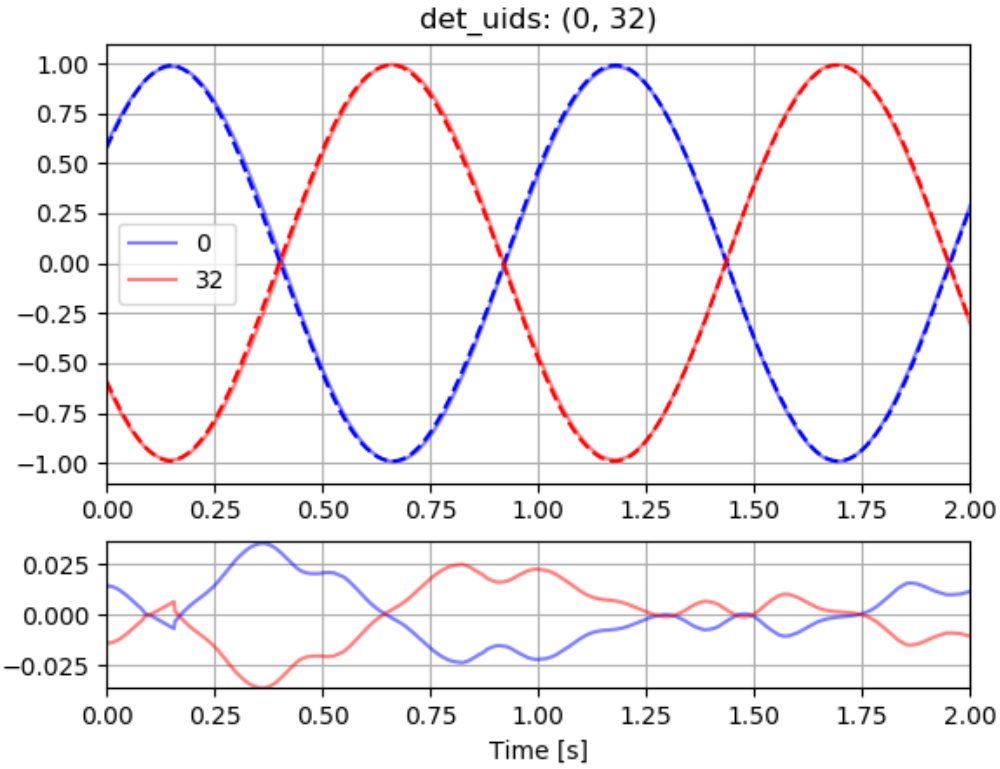

Figure 4.17: Pair of detector timestreams from colocated, orthogonal detectors from the same timestream shown in Figure 4.16. The timestreams are plotted in solid red and blue lines, with the associated fit to Equation (4.7) shown as an overplotted dashed line of the same color. The bottom panel shows the residual difference between the timestream and the fit.

in Figure 4.19. This yields an average of -0.53 degrees, with a standard deviation of 0.60 degrees. Note, qualitatively, the slight gradient going from left to right, as expected based on Figure 3.5.

This is an improvement over the thin film polarizer by almost a factor of four, and approaches some of the lowest uncertainties reported for hardware calibrators. This result may be improved with repeated, independent measurements. It may also be improved if the detector angle measurements of colocated detec-

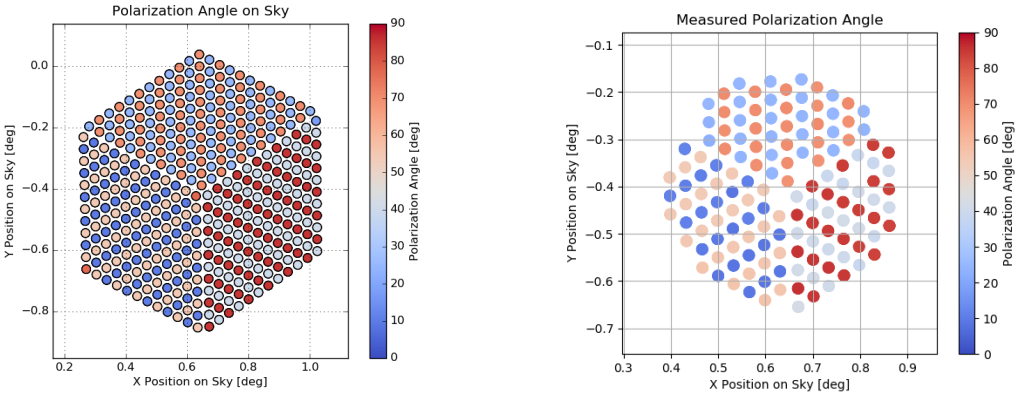

Figure 4.18: (Left): Physical detector angles for each detector pair projected on the sky. The color bar describes the angles of one of the detectors in each feedhorn, the other detector being orthogonal to the one plotted. (Right): Measured polarization angles from a wire grid data sets. Like in the left panel, each circle represents a feedhorn which contains a pair of detectors orthogonal to one another. The color bar describes the angle of a single detector in the feed. The measured angles are only shown for detectors within a 0.25 degree radius of the center of the array.

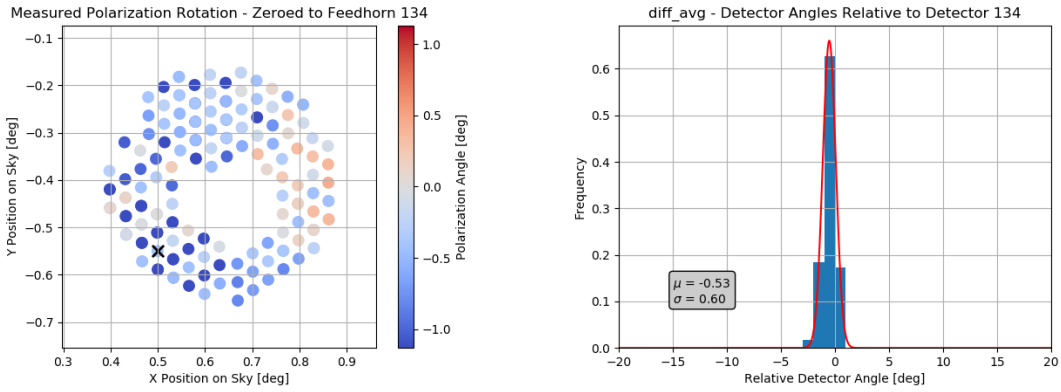

Figure 4.19: (Left): Measured polarization rotations in ar5 relative to detector 134, marked with an 'X' on this plot. Missing points near the center of the array do not have all four TESes working for this test. (Right): Histogram of average detector angles relative to detector 134 and its colocated partner, which are used as a reference.

tors of different frequencies are averaged together as well. This may be feasible as an independent measurement, as the optical modeling shows the frequency dependence of the polarization rotation caused by the optics only differs at the 0.02 degree level.

The next step, in terms of hardware development, would be an absolute angle measurement, achievable if the wiregrid can be keyed to the home hole of the encoder ring. As this was performed with the thin film polarizer, it should be possible, though might require an alignment pin hole be drilled in the wire grid frame. This development is strongly motivated, as the agreement shown here with the calculations presented in Chapter 3 continues to support our use of the calculated polarization angles for all astrophysical analyses, including those in Chapter 5.

CHAPTER 5

POLARIZATION OF A CELESTIAL SOURCE

In Chapter 3, we described a combination of optical modeling and planet observations to produce the detector angle calibration for ACTPol and Advanced ACT. In Chapter 4, we presented polarizing wire grids to measure the polarization rotation caused by the optics tube. This, however, neglects any polarization systematics from the reflectors. Ideally, we would place a polarized source in the far field, which for ACT means placing the source several kilometers away. The fixed ground screen, coupled with the fact that ACT is on top of a mountain, make it nearly impossible to do so with any ground based source. There have been proposals to fly a source on a satellite [54, 50], a drone, or a balloon [77] for calibration, however these platforms present their own difficulties.

As an alternative to placing a source in the far field we can use a well known polarized celestial source. Tau A, more commonly known as the Crab Nebula, is one such source. In this Chapter we review the current state of the field for millimeter observations of Tau A then present new Tau A maps from ACTPol observations. Finally, we see how the maps are affected when we remove the optical modeling component of our calibration from Chapter 3.

5.1 A History of Tau A Observations

Perhaps the most observed object outside of our own solar system, Tau A has been observed extensively across the electromagnetic spectrum. Tau A is the remnant of supernova SN1054, a supernova that was witnessed by Chinese astronomers on July 4, 1054 AD [41]. Tau A has several distinct components to it.

At its center is the Crab pulsar, located at (J2000) $R.A. = 5^h34^m31.9383014^s$ and $Dec. = 22°0'52.17577''$ [70]. Kinetic energy from electrons supplied by the pulsar is efficiently converted into synchrotron emission in the surrounding nebula. Around the nebula is a bright, expanding, shell of thermal gas, which, in turn, is surrounded by a faint freely expanding supernova remnant [41]. An image from NASA's Hubble Space Telescope [1] is shown in Figure 5.1.

Measurement of Tau A was proposed for use as a calibrator for CMB experiments in Aumont (2010), with the goal of providing measurements precise enough for an experiment targeting a tensor-to-scalar ratio measurement of $r = 0.01$ [8]. This lead to the constraint of needing to know one's polarization orientation to better than $0.9°$. Aumont (2010) reports measurements made with the IRAM 30 m telescope, using the XPOL instrument at 90 GHz [8]. Recently, this result has been updated with measurements using the NIKA camera at 150 GHz on the same IRAM 30 m telescope with angles that seem to differ from other reported results by several degrees [87]. Other experiments which have measured the intensity and polarization of Tau A include Planck, WMAP, Polarbear, ABS, and ACTPol. A list of reported angles is compiled in Table 5.1

Tau A is the most intense polarized source in the microwave sky at angular scales of a few arcminutes. This makes it an ideal target for cross checking polarization calibration on CMB experiments like ACTPol, which has beams on similar scales [95]. Studies of the spectral energy distribution (SED) of Tau A from 1 to 10^6 GHz suggest that the emission is dominated by the synchrotron source and varies negligibly in polarization fraction and angle in the millimeter [74]. Naess et al. reported the polarization fraction and angle based on the first season of ACTPol observations with a single array. Since then we have

[1] https://www.nasa.gov/feature/goddard/2017/messier-1-the-crab-nebula

Experiment	Frequency (GHz)	Pol. angle (deg)	Coord. Sys.	Citation
Planck	100	$-88.53 \pm 0.11 \pm 0.62$	G	[83]
Planck	143	$-84.85 \pm 0.13 \pm 0.62$	G	[83]
Planck	217	$-87.33 \pm 0.12 \pm 0.62$	G	[83]
Planck + NIKA	100	-87.52 ± 0.16	G	[87]
Planck + NIKA	143	-86.61 ± 0.21	G	[87]
Planck + NIKA	217	-87.93 ± 0.52	G	[87]
WMAP	93	$-88.70 \pm 0.70 \pm 1.5$	G	[83]
WMAP	93	$148.9 \pm 0.70 \pm 1.5$	E	[100]
IRAM	89	$-88.20 \pm 0.20 \pm 0.50$	G	[83]
NIKA/IRAM	150	$142.0 \pm 0.2 \pm 0.5 \pm 1.8$	E	[87]
NIKA/IRAM	150	$-84.3 \pm 0.7 \pm 0.5 \pm 1.8$	G	[87]
NIKA + Other	20-353	-87.5 ± 0.3	G	[87]
ABS	145	150.7 ± 1.4	E	[65]
ACTPol	146	150.7 ± 0.6	E	[76]

Table 5.1: Summary of reported Tau A measurements from CMB experiments. Reported measurements are typically integrated over an area containing the source, though for the ACT paper it is reported at the peak of the intensity map of Tau A. Measurements are commonly reported in Galactic (G) or Equatorial (E) coordinates.

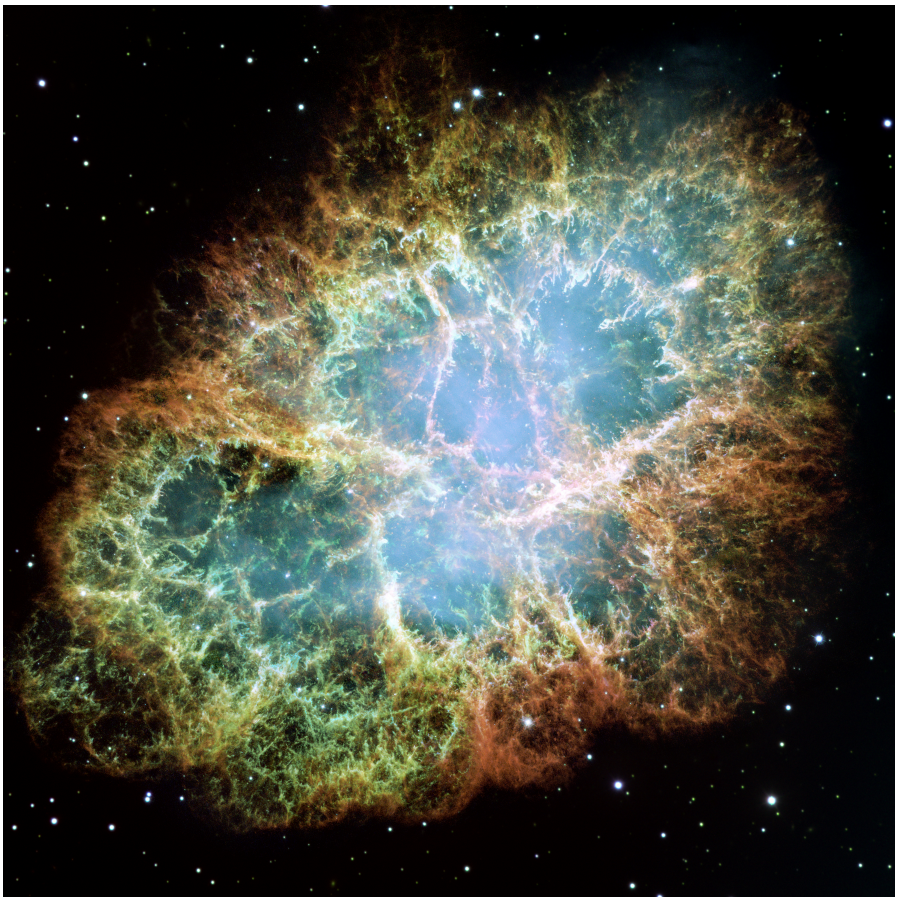

Figure 5.1: A composite image taken by NASA's Hubble Space Telescope. Composed of 24 individual Wide Field and Planetary Camera 2 exposures from 1999 and 2000, the color indicates different elements expelled during the supernova explosion. Blue represents neutral oxygen, green is singly-ionized sulfur, and red shows doubly-ionized oxygen. Image Credit NASA, ESA, J. Hester and A. Loll.

taken 405 new observations of the nebula and have used it internally for cross checking our calibration angles by mapping it and comparing it to values in the literature. We are also using it to characterize the performance of the AdvACT HWPs, but we will not present that here. Here we will examine the observations performed in 2013, 2014, and 2015, made without any HWPs installed.

5.2 Map Making

The map making process follows the preconditioned conjugate gradient (PCG) method. The conjugate gradient method is a technique for solving systems of linear equations whose matrix is symmetric and positive-definite. This technique is commonly employed in CMB experiments (see for instance the introduction to [47].) We will follow along with the notation used in the ACT description given in [25].

A model for the data is given by,

$$\mathbf{d} = \mathbf{M}\mathbf{x} + \mathbf{n}, \tag{5.1}$$

where $\mathbf{d}$ is a vector of all the measured data, $\mathbf{M}$ is the pointing matrix, which projects the map domain into the time domain, $\mathbf{x}$ is a vector we are solving for, our sky map, and $\mathbf{n}$ is a representation of the instrument noise. $\mathbf{M}$ also describes the weighting of each observation. In a simple example, each row of M corresponds to a single data point and is very sparse, containing one non-zero element per row (if considering an intensity map, three if considering polarization [78].)

The noise covariance is estimated by the inner product, $\mathbf{N} = \langle \mathbf{n}^T \mathbf{n} \rangle$. To solve for the sky signal we need to find a model which maximizes the likelihood function, which goes as,

$$\mathcal{L} \propto \exp(-\chi^2(\mathbf{x})/2). \tag{5.2}$$

This means we need to minimize χ^2, given by,

$$\chi^2(\mathbf{x}) = (\mathbf{d} - \mathbf{M}\mathbf{x})^T \mathbf{N}^{-1} (\mathbf{d} - \mathbf{M}\mathbf{x}). \tag{5.3}$$

This requires solving the map making equation [47],

$$\mathbf{M}^T\mathbf{N}^{-1}\mathbf{M}\mathbf{x} = \mathbf{M}^T\mathbf{N}^{-1}\mathbf{d}. \tag{5.4}$$

Doing this requires taking the inverse of $\mathbf{M}^T\mathbf{N}^{-1}\mathbf{M}$. However, with on order 10^7 map pixels, inverting $\mathbf{M}^T\mathbf{N}^{-1}\mathbf{M}$ is impractical. We avoid needing to invert this matrix by use of preconditioning [25].

The preconditioned conjugate gradient method (PCG) is an iterative method which is designed to ensure the conjugate gradient method converges quickly. The preconditioner, $\mathbf{P}$, is multiplied on the left of each side in Equation 5.4, and is approximately the inverse of $\mathbf{M}^T\mathbf{N}^{-1}\mathbf{M}$,

$$\mathbf{P}\mathbf{M}^T\mathbf{N}^{-1}\mathbf{M}\mathbf{x} = \mathbf{P}\mathbf{M}^T\mathbf{N}^{-1}\mathbf{d}. \tag{5.5}$$

The map maker used for mapping Tau A in this chapter is part of an internally developed Python package called moby2, which is a set of code built for producing ACT planet maps that is separate from the primary CMB map making code. When mapping Tau A, 20 PCG iterations are used, by which the solution converges.

5.2.1 Tau A Maps

In practice, map making requires compilation of the observations themselves as well as extensive sets of metadata. This metadata includes the cuts and calibration, which describe what parts of the timestreams are good to use for map making. Detectors that are behaving abnormally are cut at this stage, and segments of timestreams that contain glitches are cut here. The weather is also considered at this point and if the precipitable water vapor (PWV) is too high

(above 3 mm) the entire observation is not used. Once all data and metadata are compiled, simply running the moby2 map maker produces a collection of fits files for intensity (I) and polarization (Q and U), along with weights files.

The maps are made to be centered on the pulsar position, however the pointing moves around slightly during the season, so there is a pointing offset that can be unique to each map. This results in Tau A showing up in slightly different spots within each map. In order to stack the maps we must first align them. To do so, we choose a 'master' map, to which we will align. This is done by hand for each array and season combination, choosing a good looking map that is approximately centered. We then use the scikit-image 'register translation' function, which performs a cross-correlation in Fourier space, following [37], to identify the shift which would bring each map in line with the 'master' map. We then apply the shift in Fourier space to align the images. An example is shown in Figure 5.2.

Once the maps are all aligned they may be stacked, by which I mean simple summing of each map. This is done both with the entire set of maps, which we will use to further center our maps, and also with groups of maps, from which we will extract statistics about the map properties. The maps are split into three groups, constructed such that every third observation gets grouped together, i.e. ((1, 4, 7), (2, 5, 8), (3, 6, 9)). The stacks of each of the three groups in I, Q, and U are shown in Figure 5.3.

One might note that the 'master' map is not necessarily centered, as can be seen in Figure 5.2 or 5.3. Certain operations, such as trimming the maps and applying aperture photometry techniques, become slightly more convenient to perform with a map that is centered, so in order to facilitate these operations we

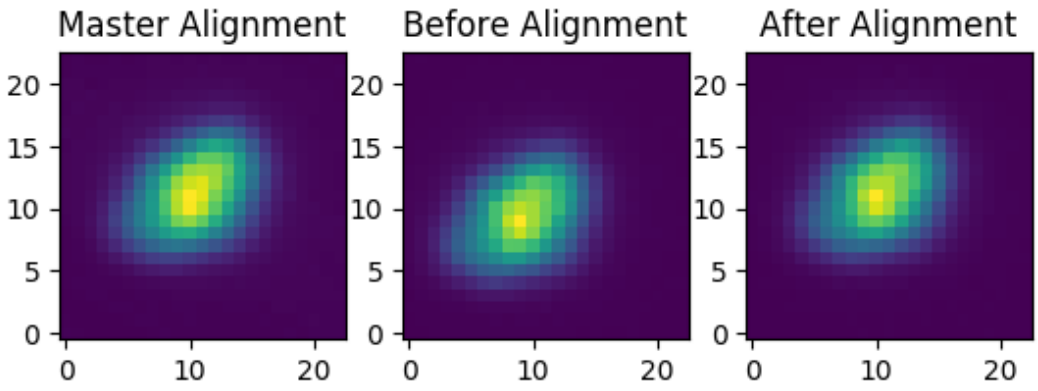

Figure 5.2: Aligning individual intensity maps of Tau A. On the left is the selected master map to which we align all other maps. In the center is the map we are aligning prior to alignment. On the right is the selected map after alignment, matching the location of the master map. This process is done for each map in intensity and the same shift is then applied to both the Q and U polarization maps. Units here are half arcminute pixels in all maps. This particular map is 1385539048.1385543292.ar1 from s13.

will further center our maps on the brightest point in the full stack of maps in intensity.

Differential aperture photometry is applied in all of the stacked maps for calibration. The mean level of the intensity maps is not constrained by the data, and so is forced to have a total flux of zero in the map-making algorithm. To calibrate this we draw an annulus around Tau A of inner radius 4.5 arcmin and outer radius 5.5 arcmin, take the mean within the annulus, and subtract it from everywhere in the map, similar to what is done in [87]. In the case of the Q and U maps, the mean level is constrained by the data, and so the mean within the annulus ends up being small. The flux within the inner diameter of the

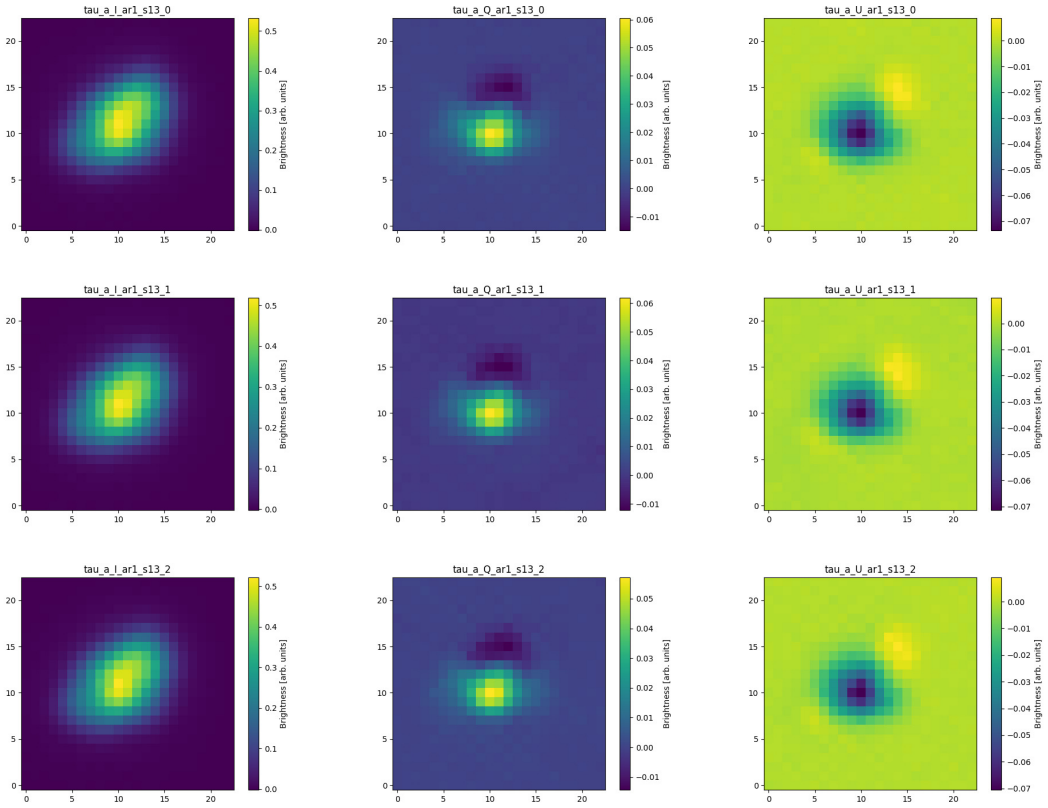

Figure 5.3: Stacked maps from the three groups, each with 22 observations (the first with 23) for a total of 67 observations. The left column contains each of the I maps, the center column contains the Q maps, and the right column contains the U maps. These maps are all from ar1, s13. Qualitatively the I, Q, and U maps from each group look similar. Note the polarization maps are about a factor of 10 less bright than the intensity map, as expected. The sign flip between the Q and U maps is a result of using the IAU polarization sign convention.

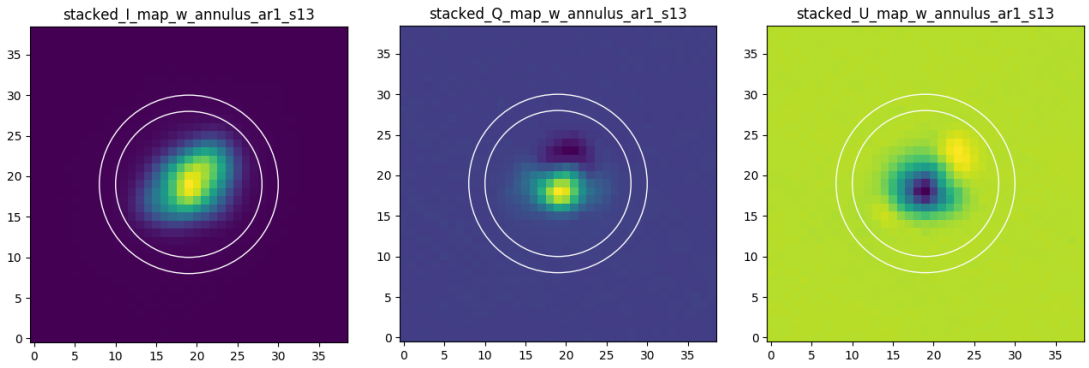

Figure 5.4: Stacked maps of 67 observations from ar1, s13 in I, Q, and U with the annulus used for differential aperture photometry shown in white.

annulus is the desired signal, from which we compute the polarization angle and polarization fraction of the source.

An example set of maps from a full stack of all 67 observations from ar1 s13, centered on the brightest pixel in the intensity map stack, with the aperture used for the differential photometry is shown in Figure 5.4.

The integrated signal over the inner diameter of the annulus is then used for computing the polarization angle and polarization fraction across the whole source. The polarization angle is given by Equation (1.14) and the polarization fraction by Equation (1.15). The measured polarization angle and polarization fraction for each array and season from s13 through s15 are shown in Table 5.2. Note these results for s13 ar1 use 46 observations, not 67 due to a more aggressive selection of 'good' maps.

Comparison with reported values is challenging, as different collaborations report the angle of Tau A using different methods. In Naess et al. the reported values are given at either the pulsar position, or the brightest location in the

Season	Array	Freq (GHz)	Pol. angle (deg)	Pol. frac (%)	Num. Obs.
s13	ar1	150	153.78 ± 1.71	7.63 ± 1.27	46
s14	ar1	150	149.96 ± 0.32	7.12 ± 0.74	20
	ar2	150	150.14 ± 0.36	7.26 ± 0.31	33
s15	ar1	150	153.70 ± 1.07	6.92 ± 0.51	7
	ar2	150	150.51 ± 0.92	7.06 ± 0.30	11
	ar3	150	152.60 ± 1.54	7.21 ± 0.88	13
	ar3	90	149.49 ± 0.73	7.53 ± 0.60	13

Table 5.2: Summary of reported Tau A measurements from the first three seasons of ACTPol. Reported measurements are integrated over a 4.5 arcmin radius around Tau A, as shown in Figure 5.4. The number of observations is dependent on how many observations of Tau A were made in that season for the given array, the weather at the time of the observation, and whether the maps looked reasonable. Values for the polarization angle are the mean and standard deviation computed from separating the maps into three different groups and stacking those groups. Values and uncertainties for the polarization fraction do not use these stacked maps and instead are the mean and standard deviation of the values computed from individual maps.

intensity map, while most other papers report the perhaps more valuable integrated signal, much like we do here. But even comparing the integrated values is prone to differ, as different apertures are used, which can vary the result significantly.

Comparing the results shown in Table 5.2 to those reported in [76] they mostly agree within 1σ except for the measurement from ar1 s15, which only contains 7 observations, and s13. This small number of observations in s15 is likely the cause of the discrepancy. A more accurate comparison could be made by considering the angle at the pulsar position or the peak intensity point. The pulsar position itself is difficult to determine due to our pointing offsets (which we avoid by using the Fourier space convolution for aligning). Our maps are also not smoothed like those in the literature. In investigating the value of the

polarization angle at the brightest pixel in the intensity maps we found that the angles were systematically higher than those integrated over the aperture. This may be due to the fact that the bright spot in intensity is close to the gradient in Q, which may be lowered if smoothed. This was found to be the case in the original analysis of the ar1 s13 data, though is not reported in [76].

Maps of the intensity of Tau A for ar1 and ar2 from s14 at 150 GHz and for ar3 s15 at both 90 and 150 GHz are shown in Figure 5.5. Qualitatively these maps agree with the one reported for ar1 s13 in [76]. This is one of the first 90 GHz maps of Tau A measured by ACTPol. The measured polarization angle is consistent with that reported by WMAP at 94 GHz [100].

5.3 The Effect of Detector Calibration on Tau A Maps

The detector angle calibration is critical in mapping any object's polarization. This is as true for mapping Tau A as it is for mapping the CMB. In the context of the ACTPol calibration procedure this leads to the question, if we remove the contribution of the polarization angle from the Code V modeling, as described in Chapter 3, how does this affect our measured properties of Tau A?

The moby2 mapper allows us to specify our own polarization calibration inputs separately when making maps. Using this feature we replaced the polarization angle calibration for the detectors with one that consists only of the lithographically defined polarization angles plus the installation angle determined from planet observations, excluding the contribution from the optically modeled polarization rotation from Code V. We then remapped Tau A for s13-s15 with all available arrays. The results are shown in Table 5.3.

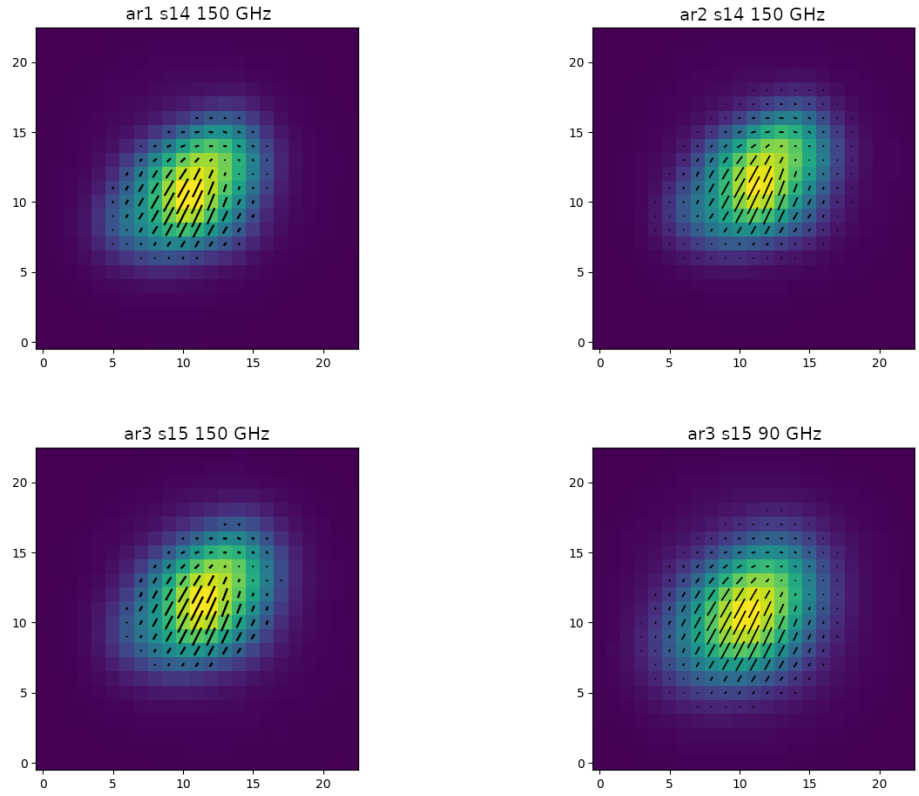

Figure 5.5: Intensity maps of Tau A with overplotted polarization angles. The top row contains maps from ar1 and ar2, respectively, from s14. The bottom row contains maps from ar3 s15 at 150 and 90 GHz, respectively. Each map is made from a full stack of all the observations from the given array/season and shows the polarization angle for points above a low threshold in intensity, with length of the polarization angle lines being proportional to the linear polarization intensity, $\sqrt{Q^2 + U^2}$. Position units are in half arcminute pixels.

Season	Array	Freq (GHz)	Pol. angle (deg)	Pol. frac (%)	Num. Obs.
s13	ar1	150	155.44 ± 2.13	6.72 ± 1.11	46
s14	ar1	150	151.05 ± 0.35	7.12 ± 0.76	20
	ar2	150	149.07 ± 0.36	7.26 ± 0.30	33
s15	ar1	150	152.01 ± 2.36	6.83 ± 0.72	7
	ar2	150	149.42 ± 0.89	7.06 ± 0.32	11
	ar3	150	152.63 ± 1.66	7.20 ± 0.87	13
	ar3	90	149.46 ± 0.74	7.53 ± 0.59	13

Table 5.3: Summary of reported Tau A measurements from the first three seasons of ACTPol with polarization angle calibrations that exclude the optical modeling portion of the calibration. Reported measurements are integrated over a 4.5 arcmin radius around Tau A, as shown in Figure 5.4. Values for the polarization angle are the mean and standard deviation computed from separating the maps into three different groups and stacking those groups. Values and uncertainties for the polarization fraction do not use these stacked maps and instead are the mean and standard deviation of the values computed from individual maps.

The changes in the polarization angles and polarization fraction between using the full calibration and excluding the Code V component, for the most part, follow expectation. They also illustrate the importance of an accurate polarization calibration. The results from both scenarios, presented in Tables 5.2 and 5.3, are plotted in Figure 5.6. The filled circles show the values from the full calibration, while the X marks show the values from the calibration without the optical modeling component.

The polarization angles shift to higher values by about a degree for ar1, and to lower values by about a degree for ar2. This makes sense, as the average rotation for ar1 from the optical modeling is 1.07 degrees and -1.09 degrees for ar2. For ar3 the angles do not change appreciably. This again makes sense, the average rotation across ar3, which is on axis with the boresight, is less than a hundredth of a degree, so we would expect little to no change in the maps.

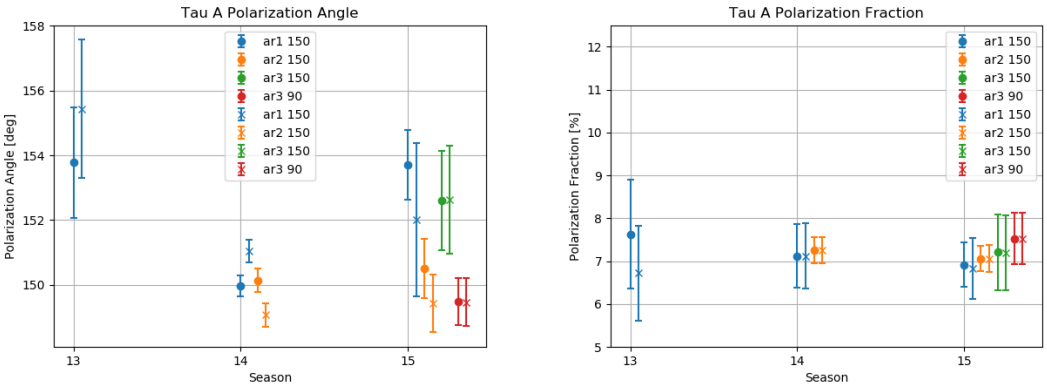

Figure 5.6: (Left): Polarization angle measurements of Tau A integrated over a 4.5′ radius centered on the peak intensity point as a function of season for all ACTPol arrays. The filled circles correspond to values in Table 5.2. The X marks correspond to the values in Table 5.3, which are the angles measured with a polarization calibration that excludes the optical modeling contributions. (Right): The polarization fraction of Tau A for each array as a function of season. The filled circles and X marks follow the same representation as the polarization angle plot at left. Both plots have points offset from their corresponding season for clarity.

The season 15, ar1 mean values do not obviously follow the expected trend, but these measurements only have seven observations, resulting in large uncertainties.

The polarization fraction should remain the same with a global rotation. The polarization fraction is given in Equation (1.15). From the definitions of Q and U we know they transform under rotation α as,

$$Q' = Q\cos(2\alpha) + U\sin(2\alpha), \tag{5.6}$$

$$U' = -Q\sin(2\alpha) + U\cos(2\alpha). \tag{5.7}$$

Plugging Q' and U' into Equation (1.15) shows we should expect the same polarization fraction with any rotation α. The polarization fraction, shown in Figure 5.6, does not change appreciably with the different calibrations to within 1σ.

The change in measured polarization angle resulting from omitting the optical modeling component of the ACTPol detector angle calibration illustrates the importance of this calibration. Without this calibration procedure the measured polarization angle of Tau A from ACTPol would be in tension with those reported by other experiments like WMAP. Calibrating to the reported values from IRAM might provide an accurate detector angle calibration, however there are still several obstacles to doing so.

Having an internally consistent calibration system is valuable in its own right, especially if the same techniques can be applied to future, more sensitive, CMB polarization experiments, such as CCAT-prime, the Simons Observatory, and CMB-S4. This enables us to report our own independent measurements of Tau A's polarization properties which can used to further study of this interesting microwave source. In addition, the Tau A measurements and internally consistent calibration can lead to improved constraints on cosmic polarization rotation.

CHAPTER 6

REMOTE OBSERVATIONS AND SITE COMPUTING INFRASTRUCTURE

Smooth operation of a telescope system requires coordination between many different people and systems. Computer systems on site include the systems which readout the detectors, log housekeeping data such as pointing information, and process the data into a compressed, easily consumable, file format for storage. These are complicated systems that need to be running with maximum uptime. Keeping these systems running may begin as the task of an expert who perhaps created the system, however must eventually be usable by others. This usability enables a team of remote observers to assist in running day to day telescope operations.

ACT has adopted this philosophy. Interfaces for the ACT computer systems and their recovery methods have been built for consumption via a simple to use web interface. This includes interfaces for generating and loading observation schedules, monitoring the state of equipment such as cryogenics, computers, and housekeeping, checking the overall state of the detectors, live viewing of housekeeping data, and remotely recovering on site hardware.

These interfaces are used by a team of remote observers, consisting of students, postdocs, and faculty within the collaboration. These remote observing coordinators (ROCs) keep the telescope scanning during the season. This is a critical part of operation of the telescope where maximizing uptime increases the data volume collected.

In this chapter I outline the ACT control systems, how we remotely observe

with the telescope, and the state of live data quality monitors.

6.1 ACT Control Systems, Monitoring, and Data Management

6.1.1 Control Systems

The ACT control system as a whole is a complicated amalgam of software and hardware. These systems need to allow for remote control of the telescope, on site computation, data collection, data storage, housekeeping data collection, cryogenic readout, data merging, and much more. Figure 6.1 shows an overview of the ACT control systems.

ACT, for the most part, is controlled through a single web interface. The ROCs connect to an Apache web server located in San Pedro de Atacama. This server also serves as an ssh gateway for more direct access. From here it is possible to connect to the rest of the ACT network. A RAID server, currently with 15 TB of capacity, and a computational node, which also serves as a backup for the RAID system, are also housed in San Pedro. The RAID system uses the native Linux 'mdadm' software RAID in a raid6 configuration. A key feature for the selection of 'mdadm' is the ability to send alert emails upon device failure which has a proven track record of alerting us of a degrading array.

The San Pedro computers connect with computers on the mountain via a line of sight (LOS) microwave link, which provides internet to the site computers. In the equipment room at the site is the interface server (internally named 'bors') which acts as an intermediary for most of the other systems at the site. This computer runs amcp (ACT master control program) which commands the

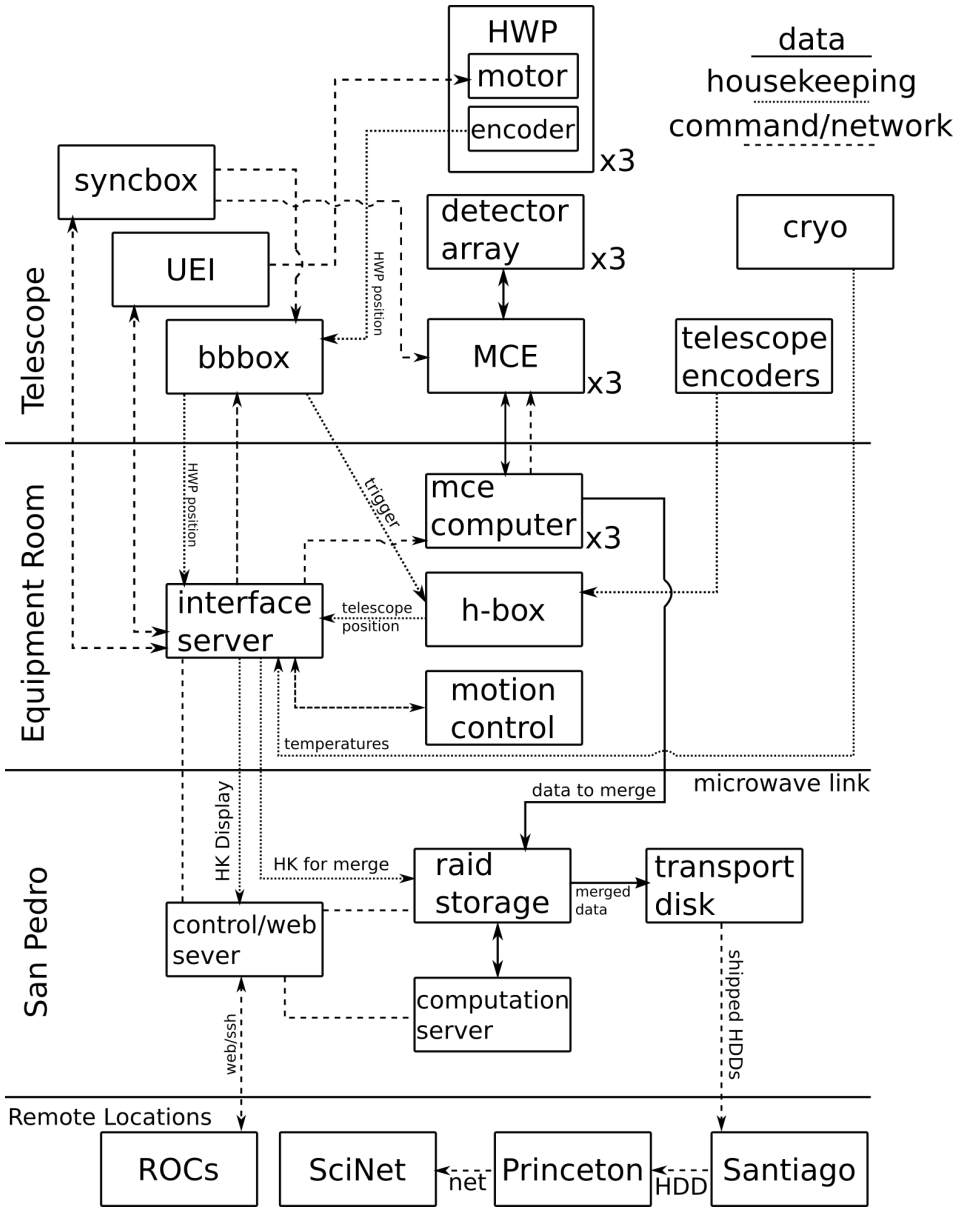

Figure 6.1: Network diagram of the ACT site control systems. Starting at the bottom of the diagram is any "Remote Location", from which a remote observing coordinator (ROC) can connect to the control server located in San Pedro de Atacama. In addition to the control and web server we house our RAID storage and a computational node. Moving up the mountain via line of sight microwave link we reach the Equipment Room. There we have an interface server which connects to most of the housekeeping and data acquisition systems, such as the MCE computers. Finally the Telescope itself houses the detector arrays, MCE crates, and housekeeping equipment.

telescope and tracks all housekeeping systems [42].

Motion control is handled by a proprietary controller provided by KUKA[1], a German robotics manufacturer, referred to as the pendant. amcp sends commands to the KUKA pendant, which houses an embedded Windows XP machine housed in the equipment room. The pointing information is provided by the telescope encoders, read out with a Heidenhain encoder box (h-box). The user only typically moves the telescope during CMB observations. Observing schedules are generated and loaded via a web interface to a program called 'sisyphus'. Parts of 'sisyphus' are installed on the MCE computers and command the MCEs, performing all required MCE actions such as tuning the detectors, performing bias steps, and collecting data timestreams.

In addition to the detectors and MCE crates the telescope houses many housekeeping systems. The dilution refrigerator has an associated computer for control of the fridge which runs an instance of kst [2], displaying fridge temperatures and pressures. Separately a custom built thermometry system reads out temperatures for the optics tubes and focal plane which are recorded in the housekeeping datastream.

For half wave plate control and angular encoder readout there are two pieces of equipment, the 'bbbox', a beaglebone green board [3], which provides the analog to digital conversion of the HWP encoders. Additionally it provides the $\sim$400 Hz RS-485 trigger to the h-box and decodes the sync word provided by the UBC sync box. This sync word allows us to synchronize the data and housekeeping timestreams.

[1] https://www.kuka.com/en-us
[2] https://kst-plot.kde.org/
[3] https://beagleboard.org/green

6.1.2 Monitoring

The schedule execution program, 'sisyphus', will display any warnings and errors that occur related to telescope control or MCE commanding. A large yellow alert box appears on the web interface and an email is sent to an operator specific mailing list with details on each error. Additionally an external service is triggered that will send a phone call, SMS message, and/or email to any configured user. This external service makes use of a paid telephony API called Twilio [4]. A web interface allows users to configure their username, phone number, and email address. The same interface can enable or disable a given user. This alert systems is in place in order to get the attention of the remote observer when critical errors occur that require manual intervention in order for observations to continue. This is perhaps most useful for waking the remote observer if a crash occurs over night.

In addition to telescope pointing and MCE command there are many more things that require monitoring. A distributed alarms system has been constructed for these things. This set of alarms consists of python scripts which run on or monitor various telescope systems. Alarms exist for tracking the site crew's travel up and down the mountain, making sure an observation schedule is loaded, monitoring the temperature of the cryogenics, monitoring each piece of housekeeping equipment/process (such as 'amcp'), and monitoring the computers themselves for such things as full discs and connectivity. Critical alarms can also trigger the same external phone call/SMS/email alerter as 'sisyphus', alerting the configured users of time sensitive errors such as cryogenic failure. There is a web interface for enabling/disabling these alarms and monitoring

[4] https://www.twilio.com/

Figure 6.2: A screenshot of the ACT alarms page.

their status, shown in part in Figure 6.2.

6.1.3 Data Management

Once the data is collected on the MCE computers it is copied down the mountain over the microwave link in its raw format along with the housekeeping datastream to the RAID (Redundant Array of Independent Disks) computer (aptly named 'raid'). There it is merged by a process called 'morgaine' [5]. This merges and compresses the data into the final "TOD" (time ordered data) file

[5] https://github.com/ACTCollaboration/ACTpol-site/tree/master/src/actmergelib

using the slim data compression library [6]. This compressed data along with most of the raw data (except for the large observation data files) are copied to a 'transport disk', which is simply a large HDD plugged into raid. This is done using a program called 'colossus', which tracks the location of all data copies in a MySQL database and ensures sufficient copies are kept while trying to free space from systems where the data is temporarily kept, like the MCE computers and raid.

Once copied to the transport disk the data is either hand carried or shipped first to Pontificia Universidad Católica de Chile in Santiago where a third copy is made, at which point the copy on raid is allowed to be deleted to free space. The transport disk is then hand carried or shipped to Princeton where another copy is made. Finally, a copy is made on Scinet over the internet from Princeton. When all copying is complete we end up with three live copies of the data, one each in Santiago, Princeton, and Scinet. There is a fourth copy on the transport disks, which sit at Princeton, but may be reused in future seasons.

In the most data dense configuration of AdvACT, with the HF, MF1, and MF2 detectors, we generate approximately 1 TB of data every 2.5 days, filling a 4 TB transport disk in 10 days. This allows us to buffer approximately 37 days of data at the site while waiting for the transport disks to be shipped to and copied in Santiago.

Data Volume

Figures 6.3 and 6.4 show how much data we have collected with ACTPol and Advanced ACTPol in units of array hours. Figure 6.3 shows the data from s13-

[6] https://sourceforge.net/projects/slimdata/

s15. In s13 we had only the first ACTPol array, ar1, and so the maximum possible number of array hours is 24. In s14 we deployed ar2, allowing a maximum of 48 array hours. In s15 we had all three ACTPol arrays deployed, increasing the maximum to 72 array hours. In practice this maximum is never achieved as the site crew stops observations for maintenance daily. Additionally the observing schedule has had downtime dependent on which fields are in the sky. In recent years, with changes to the observing strategy made for AdvACT, this downtime has decreased to $\sim$1%.

The observing efficiency greatly increased in s15, as shown in Figure 6.3. During this season we also tested the deployment of several HWPs in preparation for the Advanced ACT deployment. These times are indicated by the hatched regions, some of which are pointed out by the 'HWP' label. Figure 6.4 shows the first two seasons of Advanced ACTPol. In s16 the first AdvACT array, the HF array, was deployed starting in mid-June. This replaced ar1. Then in s17 the two MF arrays were installed in place of ar2 and ar3.

Large gaps throughout the year can be due to various reasons. At the start of the year, January into April, the weather is bad enough that we often stop observations all together. This is when we aim to perform upgrades to the telescope. Other large gaps have been caused by cryogenic failures within the cryostat sometimes coupled with site inaccessibility due to large mid-season storms. Results from s13 were reported in [76]. Updated results from s13-14 were reported in [71]. Data from the ACTPol arrays used in s15 and s16 are currently being analyzed.

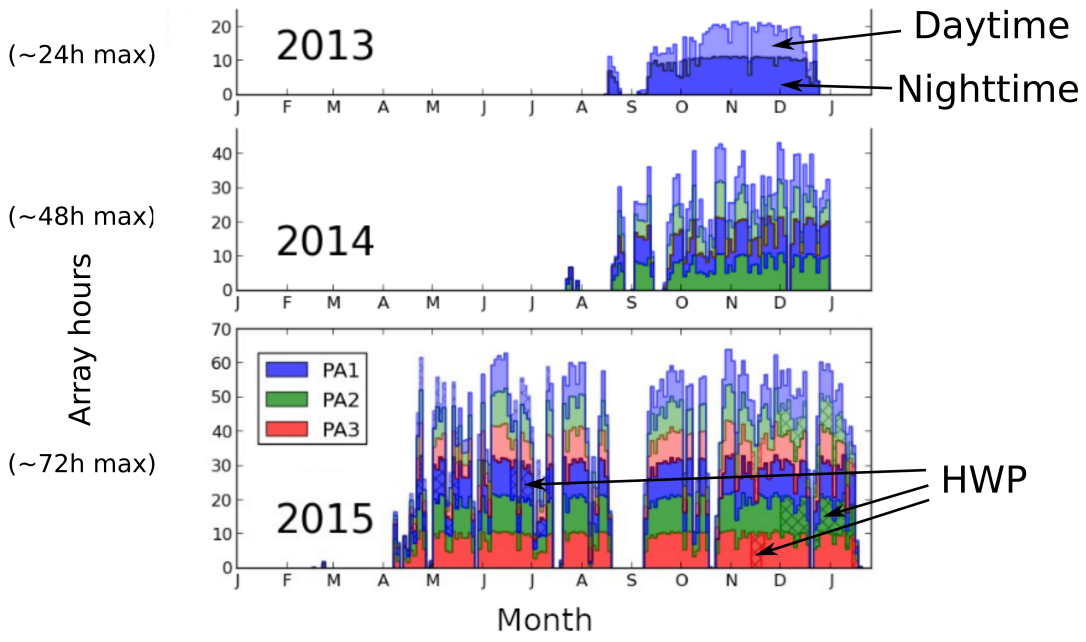

Figure 6.3: Data collected represented in array hours as a function of time for ACTPol. Each panel represents one season of data from s13-s15. The three ACTPol arrays, ar1, ar2, and ar3, are represented by three colors, blue, green, and red, respectively. Daytime data is shown in a slightly lighter shade of the given array color. Hatch marks indicate the presence of a rapidly rotation HWP during observations. Note that season observations often extend into January of the following year, before the start of the Altiplanic Winter. To accommodate this, the x-axis extends from January 1st of the specified year to January 31st of the subsequent year.

6.2 Remote Observing Coordination

ACTPol has always been operated by remote observer. This is the preferred mode of operation (over, for instance, the crew on site always commanding the telescope) as it allows for total observer attention to be given to telescope operations. The site crew must travel for around two hours per day to and from the telescope, during which they do not have the ability to fix any telescope

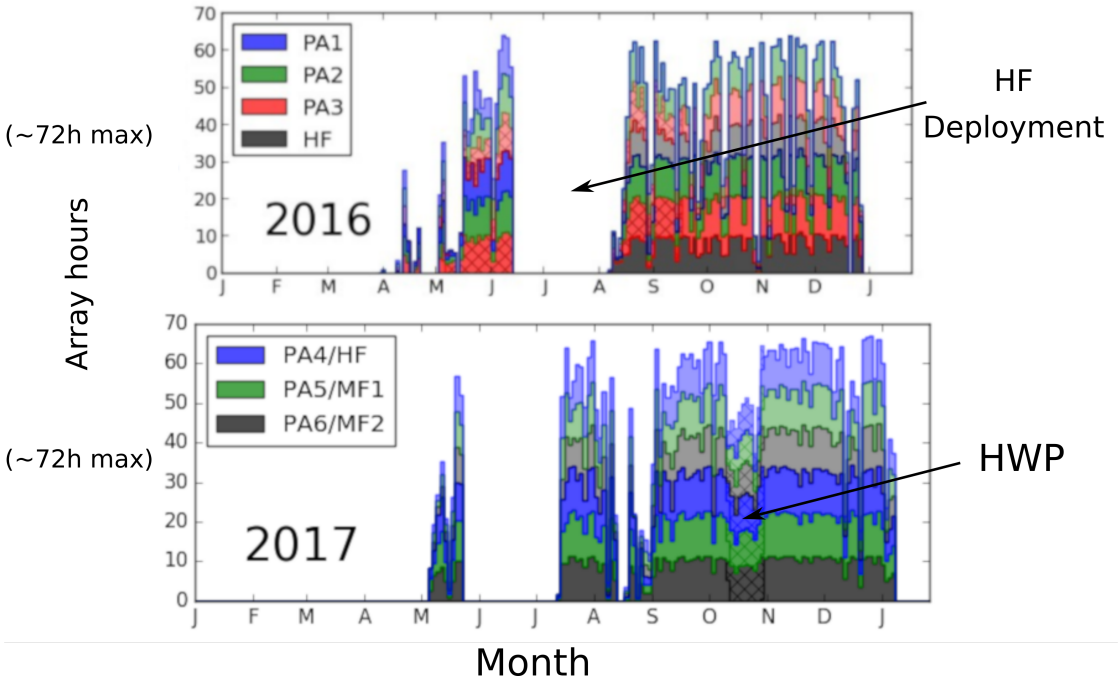

Figure 6.4: Data volume represented in array hours as a function of time for the Advanced ACTPol observing seasons, s16 and s17.

errors. Also, the high altitude environment makes it especially important that they are well rested. Telescope errors waking the site crew should be minimized.

The team started with only a handful of observers taking 24 hour shifts. The need for more members quickly became apparent and so we expanded to approximately seven observers for a season. Each year more and more observers have been trained to control and recover the telescope. The team currently stands at 31 members strong. This means each member has approximately one shift per month. New ROCs are assigned shifts more often, since there is no substitution for experience in handling telescope errors when it comes to learning about the telescope systems.

Scheduling a team of people for shifts with hard and soft constraints is

known to be an NP-hard problem, often referred to as the "Nurse Scheduling Problem" [13]. Managing this team (which I have done since August 2015) requires scheduling with constraints not unlike the nurse scheduling problem. To automate the process I have developed a script which assigns shifts and uploads the schedule to a shared Google Calendar. This has greatly reduced time required for the schedule manager to assign shifts. This code is referred to as 'rosp', the 'Remote Observer Scheduling Problem' [7].

Duties of the ROCs include coordinating with the site crew, starting telescope scans, recovering the telescope if and when it crashes, and monitoring the state of the telescope systems and data quality monitors. This can almost all be done exclusively through a cohesive web interface.

6.3 Live Data Monitoring

The analysis of entire seasons of data is a time intensive task. As pointed out in Section 6.1.3, this results in the data sitting on disk for potentially years before being fully understood. This leads to the need for having some sort of live data quality monitoring to ensure that the data collected is 'good' while it is being collected. This is all to avoid finding out that the data is 'not good' months or years after it is collected.

At the end of the s16 season a problem was identified with the HF detectors that motivated the creation of a framework for monitoring the data as it is collected. To understand the problem we need to understand the steps taken during observations. After moving the telescope into position we take an IV-

[7] https://github.com/ACTCollaboration/rosp

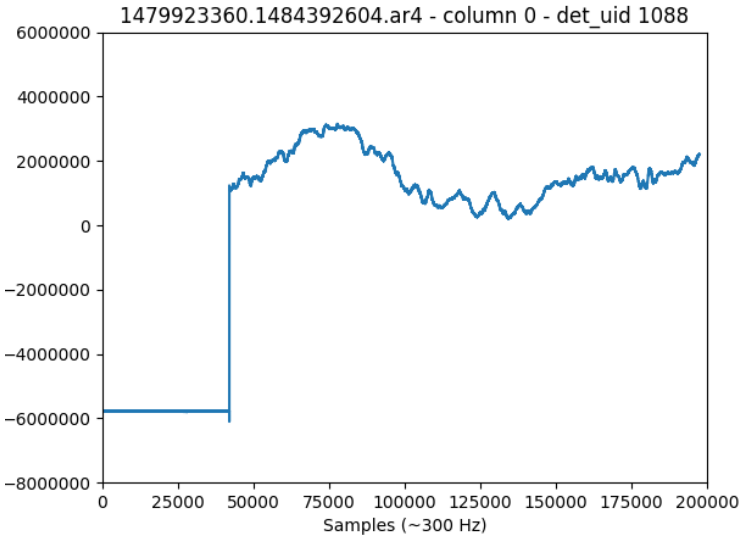

Figure 6.5: Example of a single detector starting off superconducting and then returning to normal operation part way through the timestream.

curve, which drives the detectors normal, then decreases the detector bias to sweep out the transition response. This ends with the detectors superconducting. This data is then analyzed and the best bias value for each bias line is selected. The detectors should then be driven normal again and the biases set. After some data collection that typically lasts less than an hour an 'autoconf' would be done, which reasserts the SQUID biases and then drives the detectors normal and reasserts the detector biases.

The problem was that the first IV-curve would leave some of the detectors superconducting. For some of these detectors, fluctuations in the atmosphere would kick them back onto the transition, allowing them to be useful again, but for only part of the timestream. This behavior is shown in Figure 6.5. After the first autoconf the detector biases would be reasserted, fixing the problem, but only after having the detectors in a bad state for at most an hour. The result was

that an estimated one third of the HF data from s16 was taken with the detectors superconducting. This greatly motivated the creation of a real time data monitor, focused on generating statistics related to the quality of the detectors. The developed system is referred to as 'actdm' or the ACT Data Monitor.

'actdm' allows any user to create a python script and add it to the monitor. The monitor then runs the script on every collected and merged TOD and saves the results to an HDF5 file. An associated plotting script will then be run, plotting the associated detector statistics. So far two monitors have been implemented. One simply plots the resulting number of live detectors from the output of an IV-curve. An example of an output summary plot is shown in Figure 6.6. This plot demonstrates our sensitivity to the weather. The detector count is stable as the precipitable water vapor (PWV) remains below $\sim$3mm (as measured at the APEX telescope on the slightly lower elevation ALMA plateau.) As it rises above 3mm, almost to 4mm on this particular day, the detector count on the high frequency array drops, shown as the blue line. The MF arrays are particularly robust, only losing detectors if the PWV rises well above 4mm. Figure 6.7 provides an overview of the average PWV during CMB observations for s15.

Each ACTPol array responded to changes in loading differently. Figure 6.8 shows the number of detectors which pass the IV-curve cuts as a function of loading (given by the PWV over $\sin(alt)$) for each array in 2015. Array 1 (ar1) shows the number of detectors dropping as loading increases (as expected) with a trend that is concave up. Array 2 shows a sharp drop off in the number of good detectors around a loading of 4 mm, with the number of detectors on either side of this steep drop off decreasing fairly linearly. Array 3 shows a concave

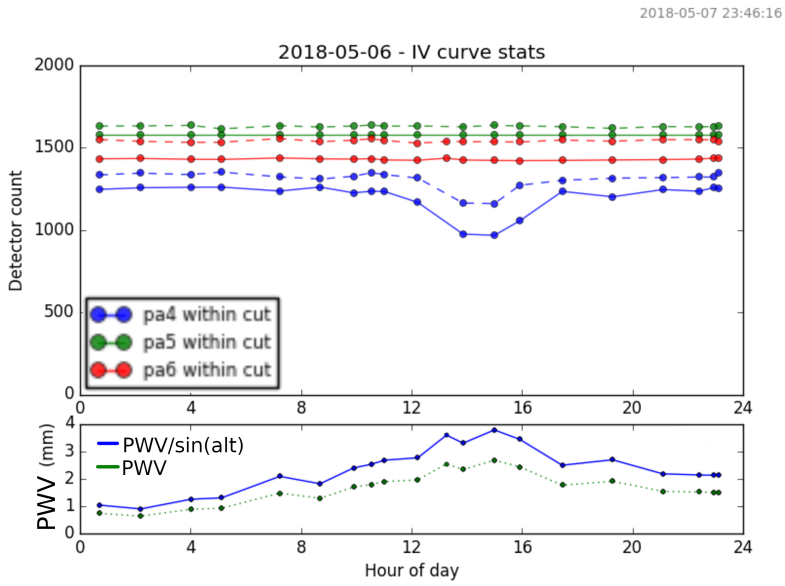

Figure 6.6: Example output plot from IV-curve statistics monitor. The top plot shows the number of live detectors. The solid line showing the number of detectors within cuts and the dashed line showing the number of IV-curves found. This represents the number of working detectors. The bottom plot shows the PWV, or precipitable water vapor, in millimeters. This is the total amount of water in the atmosphere. Good weather is 1mm or below.

down trend in the number of detectors with increased loading, with the 90 GHz detectors being particularly robust to changes in atmosphere.

The total number of detectors in HF is approximately 2,000, while each MF array contains approximately 1,700. One might ask what the behavior of the non-working detectors is, particularly if you would like to identify problems such as the superconducting detector problem we had in s16. The second monitor in place was created to categorize these non-working detectors. Currently it separates the non-working detectors into four categories, 'null response', 'low amplitude', 'ramping', and 'other'.

'null response' detectors are those who have had their feedback line turned

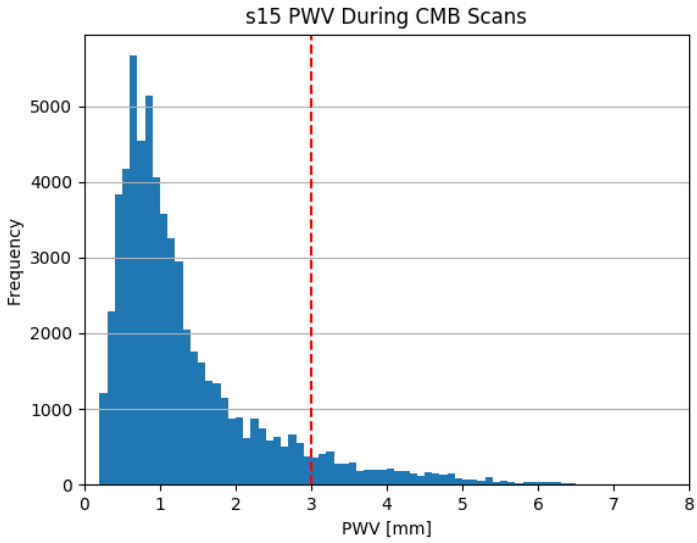

Figure 6.7: Average PWVs during all CMB scans (at most 10 minutes in length, the way the files are stored) in s15. A threshold of $3\,\mathrm{mm}$ is set when analyzing the data from CMB observations, this is shown by the red dashed line. Bins are every tenth of a mm in PWV. The first, second, and third quartiles for s15 are 0.67, 1.0, and 1.64 mm, respectively.

off deliberately, resulting in no response in the timestream. This number should remain constant throughout the season unless we turn off more feedback lines. 'low amplitude' detectors are those with an unusually low detector timestream amplitude. Figure 6.9 shows a histogram of detector timestream amplitudes for a single TOD. There are three distinct populations of detectors shown, one at low amplitudes, around or less than 10^4 DAC counts, one at high amplitudes, above 2×10^7, and one in between, around amplitudes of 10^6. 'low amplitude' detectors are those within the low amplitude population, specifically those with amplitude less than 10^4.

'ramping' detectors are the detectors in the high amplitude population. These typically have amplitudes that cover the entire available DAC range of

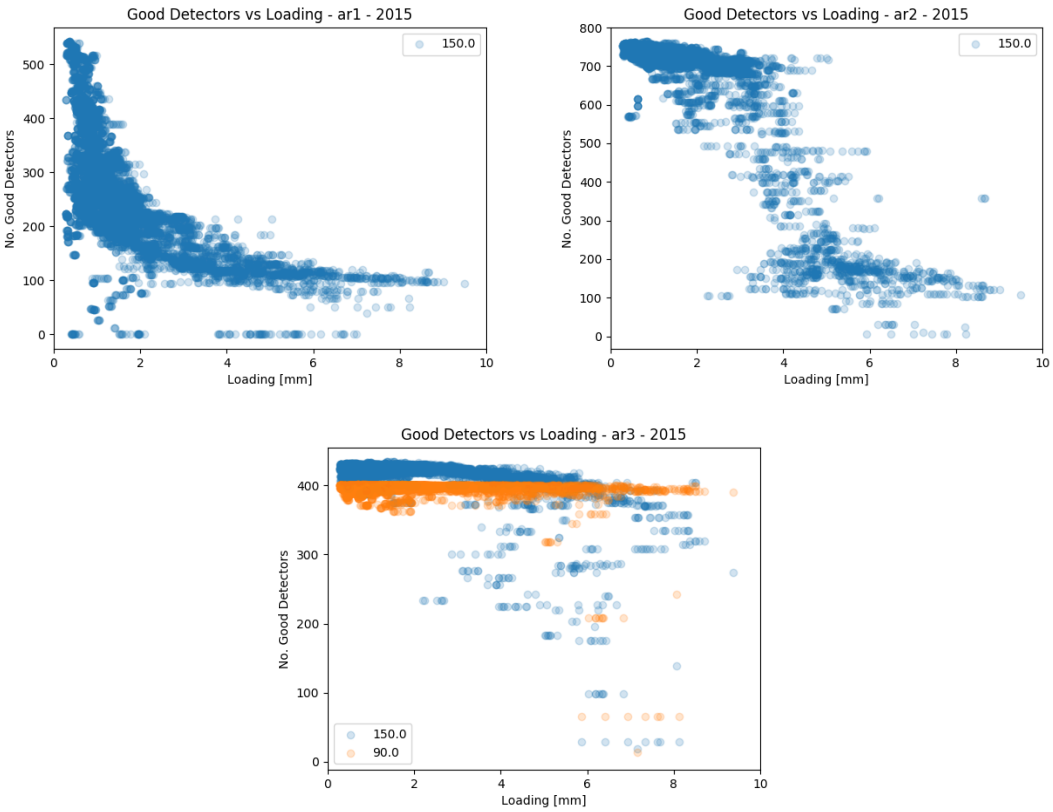

Figure 6.8: Number of detectors which pass the IV-curve cuts vs estimated sky loading, which is given by the $\mathrm{PWV}/\sin(alt)$ for each array in the 2015 observation season. The legends indicate the frequency of the detectors in GHz. Plots contain 26,014 of the 62,359 TODs from the 2015 season.

10^8. For these detectors the feedback loop within the MCE is likely failing to lock or is unstable for some reason. We have begun to identify detectors that are consistently in this ramping state and are disabling their feedback lines, meaning they will be added to the 'null response' category. Figure 6.10 shows some example timestreams for the 'low amplitude' and 'ramping' categories, as well as a working detector from the same timestream.

The timestream categorization code categorizes every detector which fits into one of the three categorizes described above. It then examines which re-

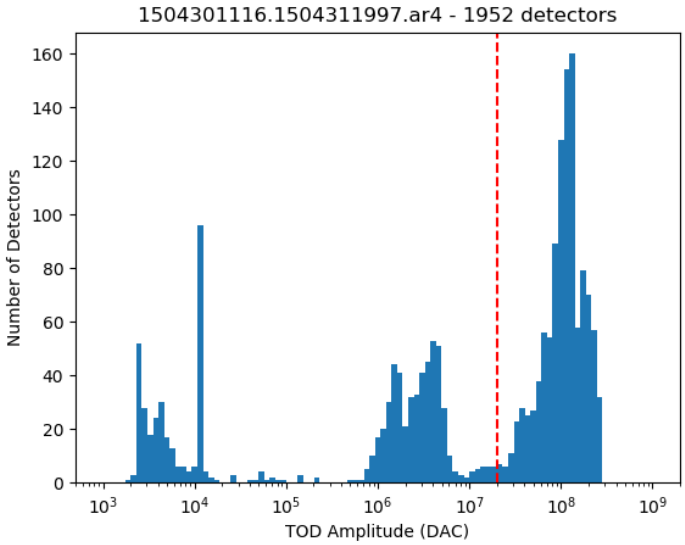

Figure 6.9: Raw timestream amplitude histogram. The bins represent the amplitude of the entire detector timestream after removing large single sample glitches with a filter. This example is for 1,952 detectors in one timestream from the HF array. The vertical red line shows the cutoff used for categorizing 'ramping' detectors of 2×10^7.

maining detectors do not pass the IV-curve cuts. Any of these detectors that do not fit into one of the three other categories gets counted in a catch all category called 'other'. This is done for every collected timestream and plotted in a stacked area plot like the one shown in Figure 6.11.

The actdm code runs on a computational node in San Pedro. A web interface served with the main ACT control pages displays each plot and allows users to scroll through old plots. The remote observers have access to this page and are tasked with checking the state of the detectors for the day leading up to their shift.

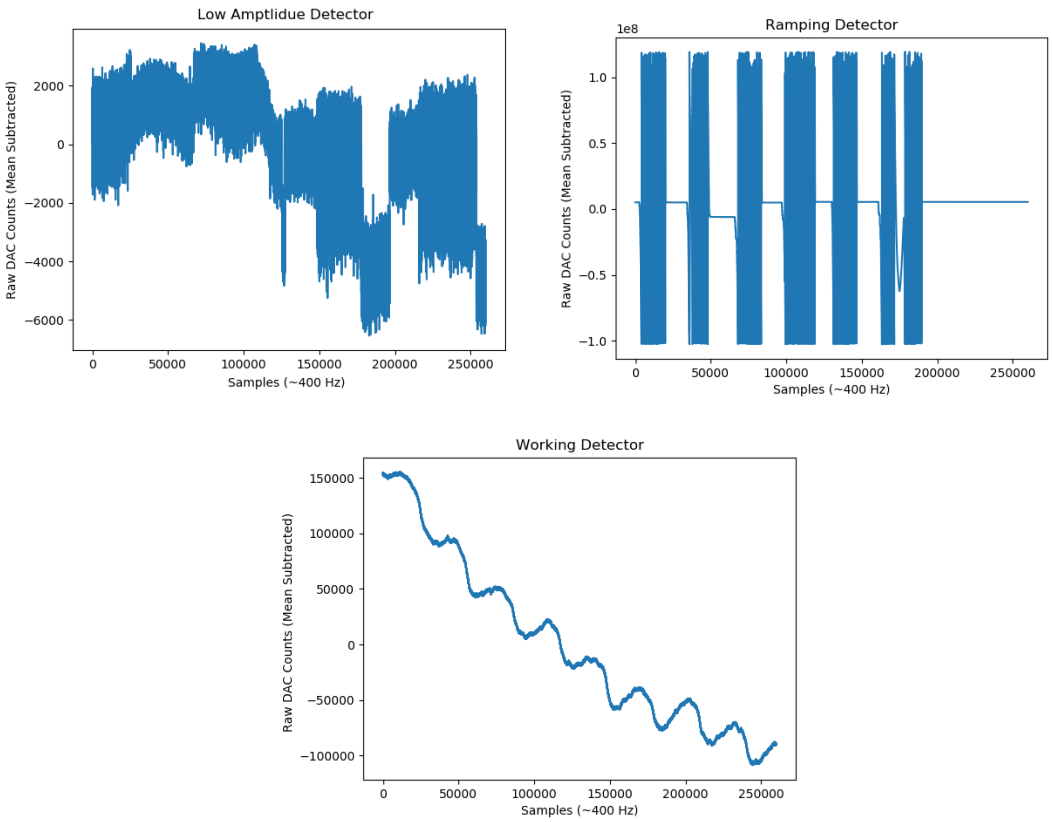

Figure 6.10: (Top Left): A 'low amplitude' detector, with amplitude spanning only 8000 DAC counts. Contrast this to the working detector in the bottom plot, exercising a range of 250,000 DAC counts. (Top Right): A 'ramping' detector. This detector exercises the full range of the DAC, 10^8 DAC counts and looks nothing like the expected atmospheric fluctuations during scanning demonstrated by the working detector in the bottom plot. (Bottom): A well-behaved, working detector with a typical DAC count amplitude of 250,000. The sinusoidal pattern is due to the telescope scanning in azimuth while the longer timescale drift may be due to a gradual change in atmospheric loading.

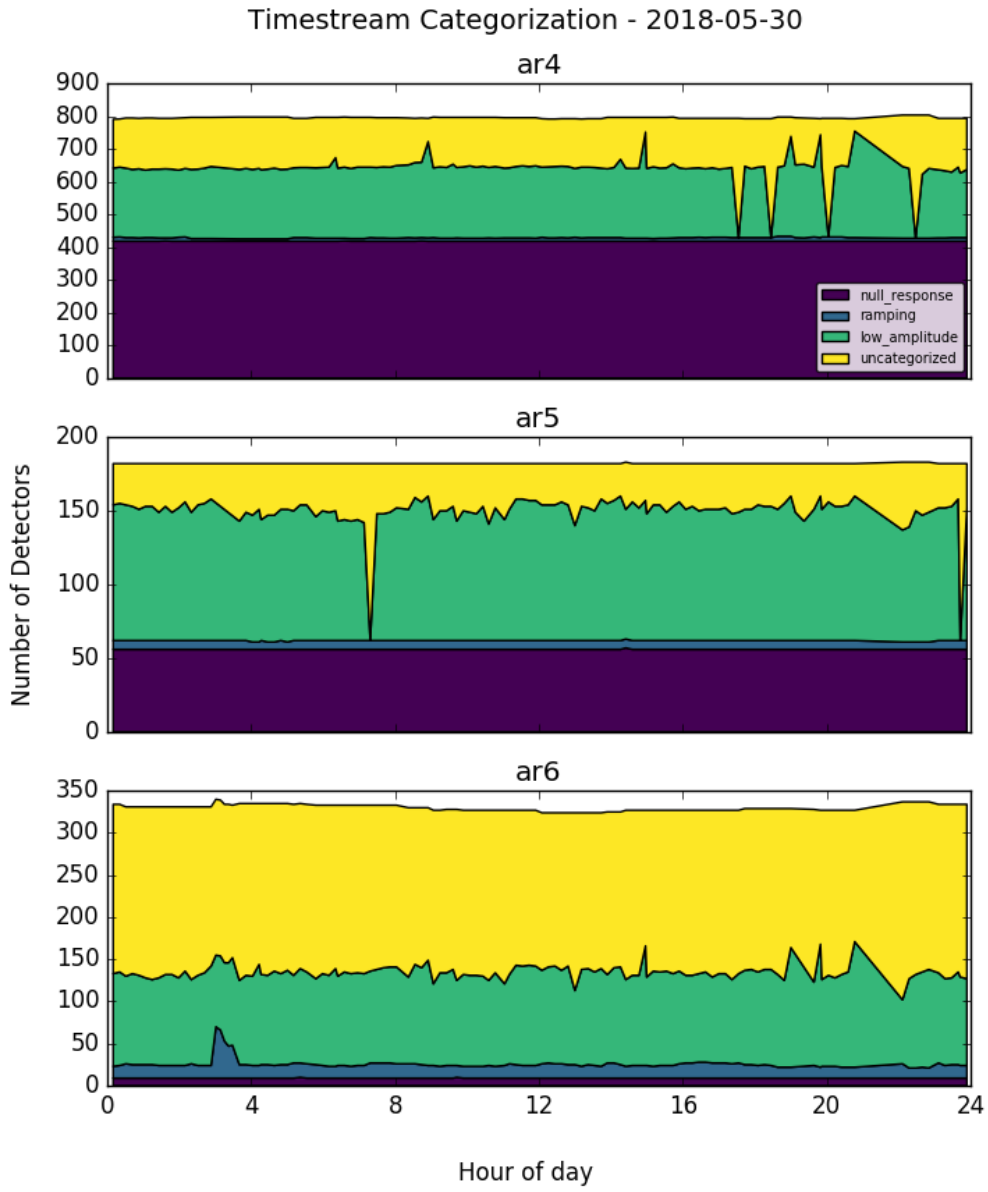

Figure 6.11: An example plot from the Timestream Categorization (timecat) data monitor. Each subplot represents one array with ar4 on top and ar6 on bottom. The y-axis in each plot shows the number of non-working detectors with the x-axis being the hour of the day. For scale, the total number of detectors in ar4, ar5, and ar6 is 2,024, 1,716, and 1,716, respectively. The colors correspond to the category the detector fits in with purple being 'null response', blue being 'ramping', green being 'low amplitude', and yellow being 'other'. See text for a description of each category.

6.3.1 Future Work

While developing the timecat code it was clear that I could easily, by eye, pick out the categories of detectors while scrolling through the timestreams. The difficulty came when trying to write down a function to do the same categorization. Ultimately this settled on a simple amplitude check, though this does not work for identifying superconducting detectors, a task I originally had planned to include in timecat. However, functions developed on one set of timestreams would fail on new sets, as each timestream can be fairly unique, especially when considering failure modes. The categorization problem, however, seems like it would map directly into the classification models that machine learning is good at. The development of a machine learning version of this timestream categorization code is an idea that I think would be worthwhile to pursue in the future. If the results are promising, taking it as far as developing a machine learning cuts packages to compare to the performance of the current cuts package would be a significant contribution to the collaboration and even the field. This may become even more significant as the total detector counts in future experiments continues to climb.

Another spinoff of this timestream analysis work is early searches for fast radio burst signals in our multichroic detectors. Preliminary results suggest that cosmic-ray-like events dominate the millisecond scale events in our timestreams. These searches will continue.

CHAPTER 7

CONCLUSIONS

ACT measurements continue to be on the cutting edge of modern cosmology. With the AdvACT upgrade, ACT will continue to measure the CMB temperature and polarization anisotropies at $\sim 1'$ resolution. The low frequency array, to be deployed in 2019, will enable measurements at 27 and 39 GHz, with some of the lowest saturation power devices of their kind. And with the deployment of a full set of rapidly rotating HWPs, ACT will probe the low multipole end of the B-mode power spectra, and possibly improve constraints on the tensor-to-scalar ratio, r.

This dissertation has detailed the unique optical modeling based approach to the ACT detector angle calibration, which has been shown to produce a calibration that results in an EB-nulling angle that is consistent with zero. AdvACT will continue to use this calibration technique for future data sets. We have also developed a series of polarizers, used to directly measure the relative angles of the detectors and to map the polarization rotation caused by the off axis optics. The latest iteration of which has achieved a relative detector angle calibration with 0.6 degree uncertainty.

Improving on these calibration techniques will be increasingly important in future polarization sensitive experiments which target measurement of r down to 0.01 and eventually 0.001. Detector angle uncertainties can limit measurements of B-mode polarization, and thus r, unless properly accounted for, with a miscalibration of 0.5° producing a B-mode signal corresponding to $r \sim 0.01$ [3]. This drives the need to continue work on both the optical modeling based approach for polarization angle calibration as well as the hardware calibrators.

Given the success this technique has seen on ACTPol, can the same process be used on the upcoming generation of telescopes? Application of the optical modeling approach to polarization calibration on another telescope, such as the Simons Observatory, would be demonstrate the portability of this technique. Developing robust uncertainties for the optically modeled angles should allow extraction of cosmological quantities such as constraints on CPR from the ACTPol EB and TB power spectra. The challenge for applying this technique to these telescopes, like SO, begins with translating the optical design into Code V from Zemax, which is widely used in the community. Alternatively, a study of the use of Zemax for such an analysis should be performed.

The use of hardware calibrators, such as the wire grids discussed in Chapter 4, while unable to measure polarization systematic contribution from the warm optics prior to the calibrator, should provide information about the polarization systematics from the cold optics. The best hardware calibrators on ground based telescopes have achieved $\sim 0.5^\circ$ precision. Improvements on this front may only come from more precise angular placement of the calibrator. On ACT, however, an absolute calibration should first be performed, by aligning the orientation of the grid to a known reference point on the HWP encoder mount.

The hardware calibration used on the Planck HFI used an aluminized Mylar polarizer, much like the aluminized PET thin film polarizer described in Chapter 4, on a 32,000 step rotator (better than 1' precision). This resulted in the conservative absolute angle uncertainty of 0.3° [88]. We should strive to achieve at least this level in the absolute calibration with our wire grids.

We have also presented maps of the polarized supernova remnant Tau A, across three seasons of ACTPol data, both at 150 and 90 GHz. Tau A is the best

celestial source available for use as a common polarization calibrator among experiments which are able to observe it. However, there are subtleties to the analysis stemming from the fact that Tau A is an extended source which makes direct comparison among experiments challenging. Reporting the polarization angle and polarization fraction in a manner which is easily compared among experiments is valuable in demonstrating to the greater community that we understand our polarization systematics. The effect of the polarization calibration on the maps presented in this thesis was shown to be a global rotation of the resulting polarization angle of the source equivalent to the average rotation determined from the optical modeling, emphasizing the importance of accurate modeling and calibration. On ACTPol I suggest we increase our observing cadence to improve our statistics in the analysis of this unique and important source.

Lastly, we described the telescope systems required to keep ACT running, including the computers systems and remote observing team, without which observations would be a challenge. These systems, while working well for ACTPol, do not necessarily all scale well for the increased detector counts planned for upcoming experiments, such as the Simons Observatory. We intend to adapt currently existing tools from SPT and Polarbear for use in the large scale detector live monitoring required for SO and eventually CMB-S4 and are designing a new, flexible system for control and live monitoring of telescope and housekeeping systems which can be used across experiments.

The calibration procedure presented has played a key role in the production of all the ACT collaboration's published CMB polarization results. The data volume shown in Chapter 6 indicates that there is a substantial amount of data on

disk to be processed. These measurements will continue to inform our knowledge about the universe.

APPENDIX A

COMPARISON OF OPTICAL DESIGN SOFTWARE

The ACTPol polarization angle calibration makes exclusive use of the Code V software from Synopsys[1]. However, much of the field uses a competing software called Zemax OpticStudio[2]. While there are tools hidden within each software to convert from one format to the other, in practice, translation between the two programs is difficult.

Some effort was made to convert the ACTPol optical design from Code V into Zemax years ago. Working from this as a starting point we attempted to verify that the designs did indeed match, so that the polarization analysis could be double checked in Zemax. This, however, never came to fruition.

With most of the CMB community using Zemax I thought it would be interesting to compare the polarization output of a very simple, single lens, system in the two programs. This study is by no means exhaustive, but might provide some insight into use of the two programs in the context of polarization modeling for calibration.

The test system is a single lens system with a 10° β-tilt. β-tilt being a tilt in the X-Z plane, about the Y-axis. The lens surface is a simple sphere, with a radius of 50 cm. The system is shown in a 2D cross section from both programs in Figure A.1. The +Z-axis is the direction in which the rays propagate. We then introduce a gradually increasing Y decenter (shift in the +Y direction) to study how the increasingly off-axis lens affects the polarization passing through it. The lens is set to have an index of refraction matching that of silicon, $n = 3.384$, and has a

[1] https://www.synopsys.com/optical-solutions/codev.html
[2] https://www.zemax.com/products/opticstudio

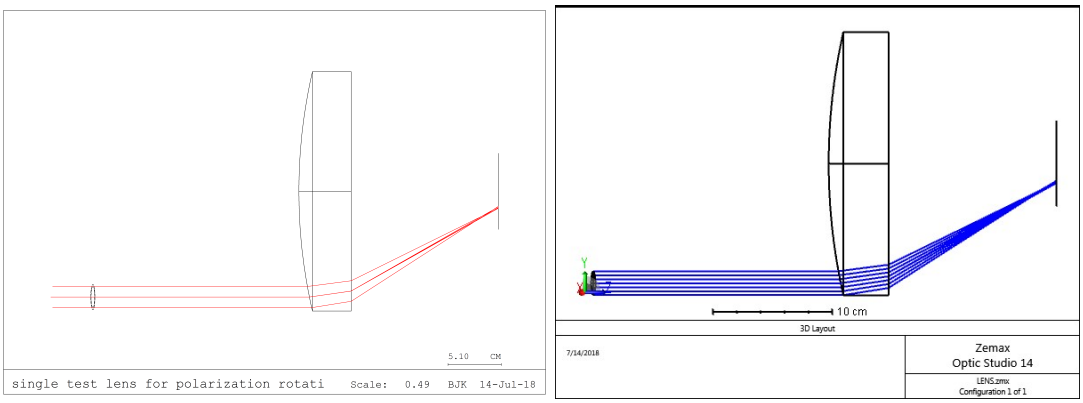

Figure A.1: The simple single lens system in both Code V (left) and Zemax OpticStudio (right) as viewed from identical angles, tilted 10 degrees out of the Y-Z plane.

two layer anti-reflection coating on both sides, the first layer being $365\,\mu\mathrm{m}$ thick with an index of refraction of 1.38 and the second layer being $200\,\mu\mathrm{m}$ thick with an index of refraction of 2.50. For completeness, screenshots of the lens/system data in each program are shown in Figure A.3 at the end of this Appendix.

We put in a perfectly polarized beam and determine the polarization state at the output. This uses the Zemax "Polarization Pupil Map" analysis, and the Code V "poldsp" user MACRO. The resulting output angles for each program are reported in Table A.1 and shown in Figure A.2.

As we can see in the results, the output polarization angle, given a perfectly polarized input, differs between the two programs by about a factor of 4.5. We believe the Zemax angle to be incorrect, due to the following statement made in the Zemax manual in the section about the 'Polarization Pupil Map':

> WARNING: The polarization pupil map assumes the rays are close to parallel to the z-axis and only uses the Ex and Ey components of

Y-Decenter (cm)	Zemax Angle (deg)	Code V Angle (deg)
0	0.0000	0.0000
1	0.3102	0.0705
2	0.6228	0.1410
3	0.9405	0.2115
4	1.2657	0.2823
5	1.6016	0.3530

Table A.1: Resulting average polarization angle across the pupil for identical lens systems (as shown in Figure A.1) in both Zemax and Code V. Each performed with an 11x11 array of rays across the pupil diameter.

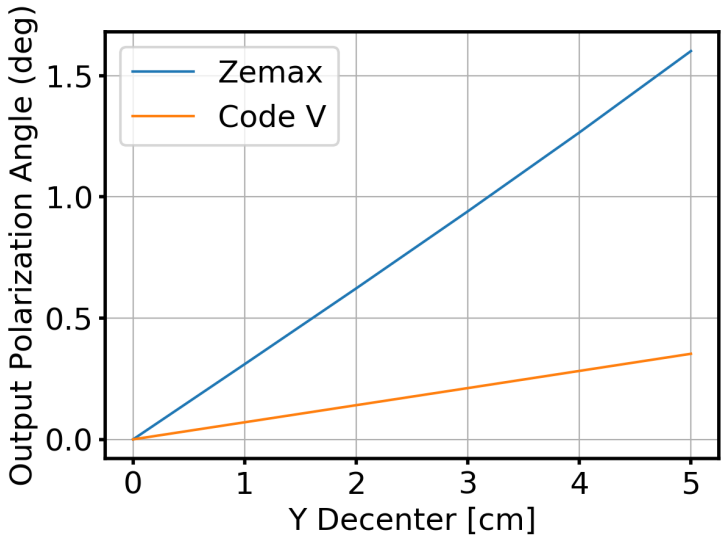

Figure A.2: Resulting average polarization angle across the pupil for identical lens systems in Code V and Zemax. Values correspond to those reported in Table A.1.

the electric field to calculate the polarization ellipse. If the rays have a significant angle relative to the z-axis, this approximation will be invalid.

This seems to mean that the Zemax polarization pupil map is not well suited for particularly fast optics. Slowing the optics by increasing the radius of curvature to 100 cm reduces the angle output by a factor of two in both programs, meaning the angle is still a factor of ~ 4.5 larger in Zemax than in Code V, which I am not sure how to reconcile.

The fact that the Code V polarization analysis produces a calibration for ACTPol which gives an EB-nulling angle consistent zero gives at least one convincing result in favor of the Code V polarization capabilities over Zemax, however it would be interesting to study the difference between the programs further if a similar analysis is to ever be done in Zemax.

Surface #	Surface Name	Surface Type	Y Radius	Thickness	Glass	Refract Mode	Y Semi-Aperture	Non-Centered Data
Object		Sphere	Infinity	Infinity		Refract		
Stop		Sphere	Infinity	20.0000		Refract	1.0000	
2		Sphere	50.0000	5.0000	'silicon'	Refract	6.0003	Basic Decenter
3		Sphere	Infinity	0.0000		Refract	5.6112	
4		Sphere	Infinity	0.0000 V		Refract	5.6112	
Image		Sphere	Infinity	17.7861 V		Refract	3.5225	

End Of Data

	Surf:Type		Comment	Radius	Thickness	Material	Coating	Clear Semi-Dia		Chip Zone	Mech Semi-Dia	Conic	TCE x 1E-6
0	OBJECT	Standard		Infinity	Infinity			0.000		0.000	0.000	0.000	0.000
1	STOP	Standard		Infinity	20.000			1.000	U	0.000	1.000	0.000	0.000
2	(tilt/dec)	Standard		50.000	5.000	NEWGLA...	DOUBLE_LAYER	6.000		0.000	6.000	0.000	-
3		Standard		Infinity	14.062		DOUBLE_LAYER	5.611		0.000	6.000	0.000	0.000
4	IMAGE	Standard		Infinity	-			3.257		0.000	3.257	0.000	0.000

Figure A.3: The lens data for the simple lens system in both Code V (top) and Zemax (bottom). Not pictured in these tables are the decenter parameters of Surface 2, which in this instance are 5 cm in the Y direction and 10 degrees in β (in Code V the angle is +10 degrees, in Zemax it is -10 degrees, due to the way the coordinate systems are defined in the two programs). The thickness to the image surface was optimized within each program separately.

APPENDIX B

THE CCATP TELESCOPE

B.1 Anti-reflective Coatings for CCATp

The silicon metamaterial anti-reflective (AR) coatings on ACTPol were the first demonstration of broad-bandwidth metamaterial AR coatings on silicon optics with finite curvature for use in millimeter bands [21]. AdvACT has deployed these coatings for use as high as 220 GHz. CCAT-p intends to observe as high as 850 GHz ($350\,\mu\mathrm{m}$). This presents a challenge in fabricating similar silicon metamaterial AR coatings, as the feature sizes need to be sub-wavelength. Dicing saw blades are available thin enough to fabricate coatings for use at 1 THz, however, the fabrication time rises dramatically with smaller feature size [18]. Thinner blades also break more often.

To avoid these challenges we developed a Deep Reactive Ion Etched anti-reflection coating procedure for application at these high frequencies. We have successfully fabricated, bonded, and measured these coatings, achieving better than 99% transmission around 900 GHz. For details see [31].

B.2 Optical Tolerancing

Early on in the development of CCATp I made use of my autov code for automating analyses in Code V (discussed in Section 3.4) to study the optical tolerances in the optical design. The analyses was set up to perturb the position of any given surface and then compute the change in the Strehl ratio from the

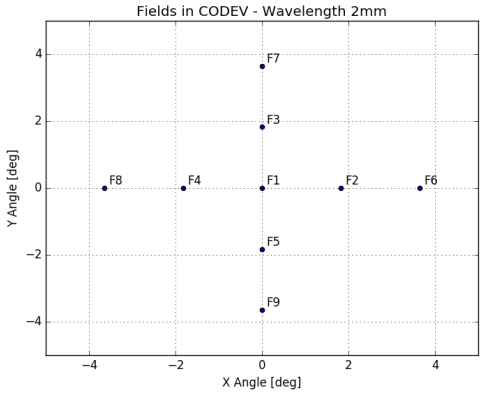

Figure B.1: Field definitions and labeled locations.

original model, specifically the file:

`Granet_CrDr_Prim5p5m_F3_20160820_S7_f3210_Ls1345.seq`

To use CODE V's tolerancing functions one specifies a maximum tolerance on each surface. CODE V then computes the "Nominal Strehl Ratio", leaving the surfaces unperturbed. Using this we compute the change in the Strehl ratio for plus and minus the specified tolerances. There are many tolerance specifications, but we have been focused on X, Y, Z translations (referred to as DLX, DLY and DLZ) and α, β, γ tilts (referred to as DLA, DLB and DLG), as well as the thickness tolerance (DLT) which is similar to a Z translation.

Since probing an interesting parameter space would involve running this process hundreds of times I've used the autov library[1]. We plot the Strehl Ratio as a function of the defined tolerance as shown in Figure B.2. We then linearly interpolate between the points to determine at what tolerance we see a 1% change in the Strehl Ratio for each of the fields (shown in Figure B.1). Taking

[1] https://github.com/BrianJKoopman/autov

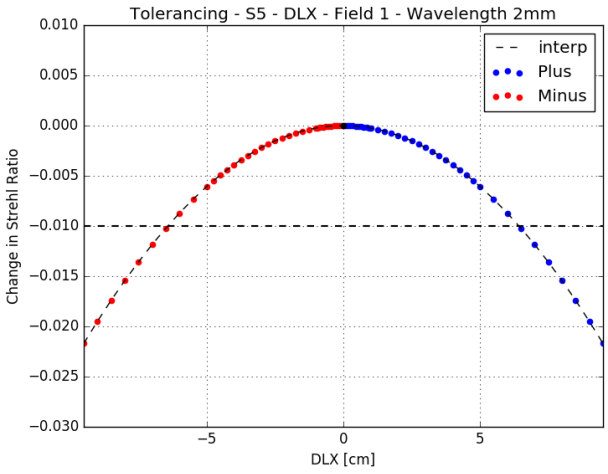

Figure B.2: Change in Strehl ratio as a function of X-decenter of the CCATp secondary mirror.

	S5 (Secondary)		S7 (Receiver)	
Tolerance	**Min**	**F1**	**Min**	**F1**
DLX	-2.772 cm	-6.424 cm	N/A	N/A
DLY	-0.630 cm	-0.630 cm	N/A	N/A
DLZ	0.255 cm	0.255 cm	-0.271 cm	-0.271 cm
DLT	-0.305 cm	-0.305 cm	-0.271 cm	-0.271 cm
DLA	0.015 deg	-0.021 deg	0.201 deg	-0.706 deg
DLB	0.081 deg	-0.118 deg	-0.243 deg	N/A

Table B.1: Constraints that produce a 1% change in the Strehl ratio. Listed are the tightest constraints for the nine chosen fields at each surface (Min) as well as the central field (F1). All for 2mm wavelength.

the most restrictive tolerance which produces a 1% change in the Strehl Ratio for any of the nine fields results in the values shown in Table B.1. This analysis is an early form of the tolerances presented in [81].

APPENDIX C

INTENSITY TO POLARIZATION LEAKAGE MODELING IN CODE V

The polarization analysis performed in Chapter 3 can also be used to model the instrumental polarization (IP) of the optics. IP leakage is a systematic where unpolarized power becomes polarized through differential transmission or reflection by optical elements [32].

The IP of the lenses can be estimated using the same polarization sensitive ray trace, in the optical design software Code V, used for modeling the systematic polarization rotation presented in the Chapter 3. Unpolarized fields are input, propagating from the sky to the detector focal plane. Code V does not model the finite conductivity of the reflectors, and so returns no contribution to

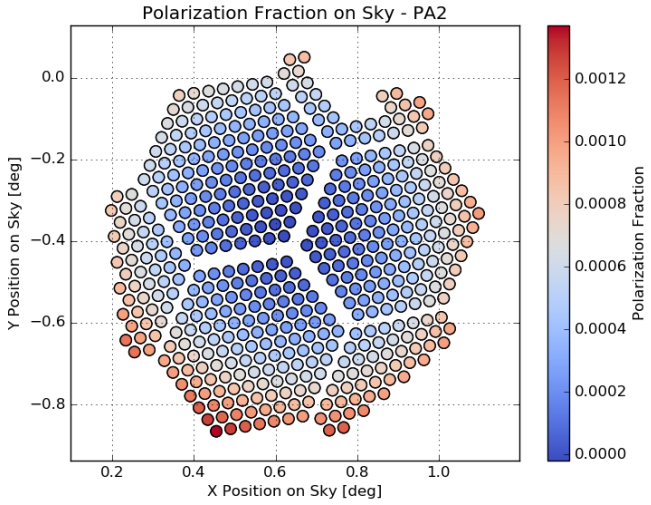

Figure C.1: IP from modeling ACTPol in Code V for array 2 (PA2). A set of 25 unpolarized inputs are propagated from the sky to the focal plane. The resulting polarization on the focal plane is then fit to a simple 2D quadratic and used to estimate the polarization fraction for each feedhorn location. IP is zero at the center of the focal plane and increases near the edges.

the polarization at the focal plane from the reflectors. In the case of ACTPol, the three lenses contribute, in total, a maximum of 0.14% near the edge of one of the off axis focal planes, shown in Figure C.1. The same analysis will be done on the SO optical design once the final design is converted to Code V.

APPENDIX D

ACRONYMS

In this Appendix you will find a (hopefully exhaustive) list of the acronyms used in this thesis.

Table D.1: Acronyms

Acronym	Meaning or Explanation
AASP	AdvACT Single Pixel
ABS	Atacama B-mode Search
ACT	The Atacama Cosmology Telescope
actdm	the ACT Data Monitor
ACTPol	The Atacama Cosmology Telescope Polarimeter, a polarization sensitive upgrade to ACT
AdvACT	Advanced ACTPol, the third generation ACT instrument, an upgrade to ACTPol
ALMA	Atacama Large Millimeter Array
AlMn	Aluminum Manganese
APEX	Atacama Pathfinder Experiment
bbbox	Beagle Bone Box, a small computer at the ACT site
BICEP	Background Imaging of Cosmic Extragalactic Polarization Telescope, located at the South Pole
BOSS-N	Baryon Oscillation Spectroscopic Survey - North, a named AdvACT field
CCATp	CCAT Prime (the CCAT bit doesn't stand for anything these days), a new telescope being built by Cornell
CIB	Cosmic Infrared Background
CMB	Cosmic Microwave Background
CMB-S4	CMB Stage 4, a future CMB experiment
COBE	Cosmic Background Explorer, the first CMB satellite, launched by NASA
CODE V	Commercial Ray Tracing software
CPR	Cosmic Polarization Rotation
CPT	Charge, parity, and time reversal (symmetry)
DAC	Digital to Analog Converter
DEC	Declination
DRIE	Deep Reactive Ion Etch
EEP	Einstein equivalence principle
FAS	Flux Activated Switch
FEA	Finite Element Analysis
FTS	Fourier Transform Spectrometer

Table D.1: Acronyms (continued)

Acronym	Meaning or Explanation
G	Thermal Conductivity
GRB	Gamma Ray Burst
HDF5	Hierarchical Data Format 5
HF	High Frequency, the 150/220 GHz bands for AdvACT
HFSS	High-Frequency Structure Simulator
HWP	Half Wave Plate
HSC	Hyper Suprime-Cam
IV	Current/Voltage, in context of IV-curve, a procedure used to determine device saturation power
KiDS	Kilo-Degree Survey
kst	A KDE based plotting application (with unknown acronym definition)
KUKA	Keller und Knappich Augsburg, a German robotics company
ΛCDM	Lambda Cold Dark Matter, the standard model of big bang cosmology
LF	Low Frequency, the 27/39 GHz bands for AdvACT
LOS	Line of Sight
MBAC	Millimeter Bolometer Array Camera, the first camera deployed on ACT
MCE	Multichannel Electronics, readout electronics used throughout the field, produced by UBC
MF	Mid Frequency, the 90/150 GHz bands for AdvACT
MoCu	Molybdenum Copper
MUL	Code V Multilayer Coating file, specifies surface coatings
NIST	National Institute of Standards and Technology
OMT	Ortho-Mode Transducer
PA	Polarization Array, one set of detectors in ACT
PCB	Printed Circuit Board
PCG	Preconditioned Conjugate Gradient, a method used in map making
PdAu	Palladium Gold
PET	PolyEthylene Terephthalate, a material similar to the more commonly known Mylar
PID	Proportional, Integral, Derivative, the three terms in a PID control loop, providing active feedback to a system
P_{sat}	Saturation Power
PSF	Point Spread Function
PT	Pulse Tube, a 4K cryocooler
PWV	Precipitable Water Vapor
RA	Right Ascension
RAID	Redundant Array of Independent Disks

Table D.1: Acronyms (continued)

Acronym	Meaning or Explanation
ROC	Remote Observing Coordinator, the name given to members of the ACT collaboration who take shifts controlling the telescope
SED	Spectral Energy Distribution
SO	The Simons Observatory
SiN	Silicon Nitride
SPIRE	The Herschel Spectral and Photometric Imaging Receiver
SQUID	Superconducting Quantum Interference Device
SPIDER	A balloon borne CMB telescope
SPT	The South Pole Telescope
SPTPol	The polarization upgrade to the South Pole Telescope
TDM	Time Division Multiplexing
TES	Transition Edge Sensor
TOD	Time Ordered Data
UBC	University of British Columbia
UCSD	University of California, San Diego
WEP	Weak Equivalence Principle
WMAP	Wilkinson Microwave Anisotropy Probe, a NASA satellite which measured the CMB; the successor to COBE

BIBLIOGRAPHY

[1] A non-metric theory of gravity. http://astrod.wikispaces.com/file/view/A%20Non-metric%20Theory%20of%20Gravity.pdf/134199975/A%20Non-metric%20Theory%20of%20Gravity.pdf. Accessed: 2015-05-20.

[2] K. N. Abazajian, P. Adshead, Z. Ahmed, S. W. Allen, D. Alonso, K. S. Arnold, C. Baccigalupi, J. G. Bartlett, N. Battaglia, B. A. Benson, C. A. Bischoff, J. Borrill, V. Buza, E. Calabrese, R. Caldwell, J. E. Carlstrom, C. L. Chang, T. M. Crawford, F.-Y. Cyr-Racine, F. De Bernardis, T. de Haan, S. di Serego Alighieri, J. Dunkley, C. Dvorkin, J. Errard, G. Fabbian, S. Feeney, S. Ferraro, J. P. Filippini, R. Flauger, G. M. Fuller, V. Gluscevic, D. Green, D. Grin, E. Grohs, J. W. Henning, J. C. Hill, R. Hlozek, G. Holder, W. Holzapfel, W. Hu, K. M. Huffenberger, R. Keskitalo, L. Knox, A. Kosowsky, J. Kovac, E. D. Kovetz, C.-L. Kuo, A. Kusaka, M. Le Jeune, A. T. Lee, M. Lilley, M. Loverde, M. S. Madhavacheril, A. Mantz, D. J. E. Marsh, J. McMahon, P. D. Meerburg, J. Meyers, A. D. Miller, J. B. Munoz, H. N. Nguyen, M. D. Niemack, M. Peloso, J. Peloton, L. Pogosian, C. Pryke, M. Raveri, C. L. Reichardt, G. Rocha, A. Rotti, E. Schaan, M. M. Schmittfull, D. Scott, N. Sehgal, S. Shandera, B. D. Sherwin, T. L. Smith, L. Sorbo, G. D. Starkman, K. T. Story, A. van Engelen, J. D. Vieira, S. Watson, N. Whitehorn, and W. L. Kimmy Wu. CMB-S4 Science Book, First Edition. *ArXiv e-prints*, October 2016.

[3] M. H. Abitbol, J. C. Hill, and B. R. Johnson. Foreground-induced biases in CMB polarimeter self-calibration. MNRAS, 457:1796–1803, April 2016.

[4] P. A. R. Ade, R. W. Aikin, D. Barkats, S. J. Benton, C. A. Bischoff, J. J. Bock, J. A. Brevik, I. Buder, E. Bullock, C. D. Dowell, L. Duband, J. P. Filippini, S. Fliescher, S. R. Golwala, M. Halpern, M. Hasselfield, S. R. Hildebrandt, G. C. Hilton, V. V. Hristov, K. D. Irwin, K. S. Karkare, J. P. Kaufman, B. G. Keating, S. A. Kernasovskiy, J. M. Kovac, C. L. Kuo, E. M. Leitch, M. Lueker, P. Mason, C. B. Netterfield, H. T. Nguyen, R. O'Brient, R. W. Ogburn, A. Orlando, C. Pryke, C. D. Reintsema, S. Richter, R. Schwarz, C. D. Sheehy, Z. K. Staniszewski, R. V. Sudiwala, G. P. Teply, J. E. Tolan, A. D. Turner, A. G. Vieregg, C. L. Wong, K. W. Yoon, and Bicep2 Collaboration. Detection of B-Mode Polarization at Degree Angular Scales by BICEP2. *Physical Review Letters*, 112(24):241101, June 2014.

[5] Mohamed Nurul Afsar and Hua Chi. Millimeter wave complex refractive index, complex dielectric permittivity and loss tangent of extra high pu-

rity and compensated silicon. *International Journal of Infrared and Millimeter Waves*, 15(7):1181–1188, July 1994.

[6] R. A. Alpher, H. Bethe, and G. Gamow. The Origin of Chemical Elements. *Physical Review*, 73:803–804, April 1948.

[7] R. A. Alpher and R. C. Herman. Theory of the Origin and Relative Abundance Distribution of the Elements. *Reviews of Modern Physics*, 22:153–212, April 1950.

[8] J. Aumont, L. Conversi, C. Thum, H. Wiesemeyer, E. Falgarone, J. F. Macías-Pérez, F. Piacentini, E. Pointecouteau, N. Ponthieu, J. L. Puget, C. Rosset, J. A. Tauber, and M. Tristram. Measurement of the Crab nebula polarization at 90 GHz as a calibrator for CMB experiments. A&A, 514:A70, May 2010.

[9] E. S. Battistelli, M. Amiri, B. Burger, M. J. Devlin, S. R. Dicker, W. B. Doriese, R. Dünner, R. P. Fisher, J. W. Fowler, M. Halpern, M. Hasselfield, G. C. Hilton, A. D. Hincks, K. D. Irwin, M. Kaul, J. Klein, S. Knotek, J. M. Lau, M. Limon, T. A. Marriage, M. D. Niemack, L. Page, C. D. Reintsema, S. T. Staggs, D. S. Swetz, E. R. Switzer, R. J. Thornton, and Y. Zhao. Automated SQUID tuning procedure for kilo-pixel arrays of TES bolometers on the Atacama Cosmology Telescope. In *Millimeter and Submillimeter Detectors and Instrumentation for Astronomy IV*, volume 7020, page 702028, July 2008.

[10] E. S. Battistelli, M. Amiri, B. Burger, M. Halpern, S. Knotek, M. Ellis, X. Gao, D. Kelly, M. Macintosh, K. Irwin, and C. Reintsema. Functional Description of Read-out Electronics for Time-Domain Multiplexed Bolometers for Millimeter and Sub-millimeter Astronomy. *Journal of Low Temperature Physics*, 151:908–914, May 2008.

[11] J. Beyer and D. Drung. A SQUID multiplexer with superconducting-to-normalconducting switches. *Superconductor Science Technology*, 21(10):105022, October 2008.

[12] Max Born and Emil Wolf. *Principles of Optics (7th Ed)*. Cambridge University Press, 1999.

[13] Edmund K. Burke, Patrick De Causmaecker, Greet Vanden Berghe, and Hendrik Van Landeghem. The State of the Art of Nurse Rostering. *Journal of Scheduling*, 7(6):441–499, November 2004.

[14] E. Calabrese, R. A. Hlozek, N. Battaglia, E. S. Battistelli, J. R. Bond, J. Chluba, D. Crichton, S. Das, M. J. Devlin, J. Dunkley, R. Dünner, M. Farhang, M. B. Gralla, A. Hajian, M. Halpern, M. Hasselfield, A. D. Hincks, K. D. Irwin, A. Kosowsky, T. Louis, T. A. Marriage, K. Moodley, L. Newburgh, M. D. Niemack, M. R. Nolta, L. A. Page, N. Sehgal, B. D. Sherwin, J. L. Sievers, C. Sifón, D. N. Spergel, S. T. Staggs, E. R. Switzer, and E. J. Wollack. Cosmological parameters from pre-planck cosmic microwave background measurements. Phys. Rev. D, 87(10):103012, May 2013.

[15] S. M. Carroll. Quintessence and the Rest of the World: Suppressing Long-Range Interactions. *Physical Review Letters*, 81:3067–3070, October 1998.

[16] Sean M. Carroll, George B. Field, and Roman Jackiw. Limits on a lorentz- and parity-violating modification of electrodynamics. *Phys. Rev. D*, 41:1231–1240, Feb 1990.

[17] S. K. Choi, J. Austermann, J. A. Beall, K. T. Crowley, R. Datta, S. M. Duff, P. A. Gallardo, S.-P. P. Ho, J. Hubmayr, B. J. Koopman, Y. Li, F. Nati, M. D. Niemack, L. A. Page, M. Salatino, S. M. Simon, S. T. Staggs, J. Stevens, J. Ullom, and E. J. Wollack. Characterization of the Mid-Frequency Arrays for Advanced ACTPol. *ArXiv e-prints*, November 2017.

[18] K. P. Coughlin, J. J. McMahon, K. T. Crowley, B. J. Koopman, K. H. Miller, S. M. Simon, and E. J. Wollack. Pushing the Limits of Broadband and High Frequency Metamaterial Silicon Antireflection Coatings. *ArXiv e-prints*, April 2018.

[19] K. Crowley, S. M. Duff, P. A. Gallardo, J. Hubmayr, B. J. Koopman, F. Nati, M. D. Niemack, M. Salatino, S. M. Simon, S. T. Staggs, E. M. Vavagiakis, and E. J. Wollack. Advanced ACTPol TES Device Parameters and Noise Performance in Fielded Arrays. *J. Low Temp. Phys. in prep.*, 2017.

[20] R. Datta, J. Austermann, J. A. Beall, D. Becker, K. P. Coughlin, S. M. Duff, P. A. Gallardo, E. Grace, M. Hasselfield, S. W. Henderson, G. C. Hilton, S. P. Ho, J. Hubmayr, B. J. Koopman, J. V. Lanen, D. Li, J. McMahon, C. D. Munson, F. Nati, M. D. Niemack, L. Page, C. G. Pappas, M. Salatino, B. L. Schmitt, A. Schillaci, S. M. Simon, S. T. Staggs, J. R. Stevens, E. M. Vavagiakis, J. T. Ward, and E. J. Wollack. Design and Deployment of a Multichroic Polarimeter Array on the Atacama Cosmology Telescope. *Journal of Low Temperature Physics*, 184:568–575, August 2016.

[21] R. Datta, C. D. Munson, M. D. Niemack, J. J. McMahon, J. Britton,

E. J. Wollack, J. Beall, M. J. Devlin, J. Fowler, P. Gallardo, J. Hubmayr, K. Irwin, L. Newburgh, J. P. Nibarger, L. Page, M. A. Quijada, B. L. Schmitt, S. T. Staggs, R. Thornton, and L. Zhang. Large-aperture wide-bandwidth antireflection-coated silicon lenses for millimeter wavelengths. Appl. Opt., 52:8747, December 2013.

[22] F. De Bernardis, J. R. Stevens, M. Hasselfield, D. Alonso, J. R. Bond, E. Calabrese, S. K. Choi, K. T. Crowley, M. Devlin, J. Dunkley, P. A. Gallardo, S. W. Henderson, M. Hilton, R. Hlozek, S. P. Ho, K. Huffenberger, B. J. Koopman, A. Kosowsky, T. Louis, M. S. Madhavacheril, J. McMahon, S. Næss, F. Nati, L. Newburgh, M. D. Niemack, L. A. Page, M. Salatino, A. Schillaci, B. L. Schmitt, N. Sehgal, J. L. Sievers, S. M. Simon, D. N. Spergel, S. T. Staggs, A. van Engelen, E. M. Vavagiakis, and E. J. Wollack. Survey strategy optimization for the Atacama Cosmology Telescope. In *Observatory Operations: Strategies, Processes, and Systems VI*, volume 9910 of Proc. SPIE, page 991014, July 2016.

[23] Paolo de Bernardis and Silvia Masi. Cosmic microwave background and cosmic polarization rotation: An experimentalist view. *International Journal of Modern Physics D*, 25(11):1640012, October 2016.

[24] S. M. Duff, J. Austermann, J. A. Beall, D. Becker, R. Datta, P. A. Gallardo, S. W. Henderson, G. C. Hilton, S. P. Ho, J. Hubmayr, B. J. Koopman, D. Li, J. McMahon, F. Nati, M. D. Niemack, C. G. Pappas, M. Salatino, B. L. Schmitt, S. M. Simon, S. T. Staggs, J. R. Stevens, J. Van Lanen, E. M. Vavagiakis, J. T. Ward, and E. J. Wollack. Advanced actpol multichroic polarimeter array fabrication process for 150 mm wafers. *Journal of Low Temperature Physics*, 184(3):634–641, Aug 2016.

[25] Rolando Dünner, Matthew Hasselfield, Tobias A. Marriage, Jon Sievers, Viviana Acquaviva, Graeme E. ˆM Addison, Peter A. R. Ade, Paula Aguirre, Mandana Amiri, John William Appel, L. Felipe Barrientos, Elia S. ˆM Battistelli, J. Richard Bond, Ben Brown, Bryce Burger, Erminia Calabrese, Jay Chervenak, Sudeep Das, Markˆ M J. Devlin, Simon R. Dicker, W. Bertrand Doriese, Joanna Dunkley, Thomas Essinger-Hileman, Ryan P. ˆM Fisher, Megan B. Gralla, Joseph W. Fowler, Amir Hajian, Mark Halpern, Carlos Hernández-Monteagudo, Gene C. ˆM Hilton, Matt Hilton, Adam D. Hincks, Renée Hlozek, Kevin M. Huffenberger, David H. Hughes, John P. ˆM Hughes, Leopoldo Infante, Kent D. Irwin, Jean Baptiste Juin, Madhuri Kaul, Jeff Klein, Arthurˆ M Kosowsky, Judy M. Lau, Michele Limon, Yen-Ting Lin, Thibaut Louis, Robert H. Lupton, Danica Marsden, Kristaˆ M Martocci, Phil Mauskopf, Felipe Menanteau, Kavilan Moodley, Harvey Moseley, Calvin B. Netterfield, Michaelˆ M D. Niemack,

Michael R. Nolta, Lyman A. Page, Lucas Parker, Bruce Partridge, Hernan Quintana, Beth^M Reid, Neelima Sehgal, Blake D. Sherwin, David N. Spergel, Suzanne T. Staggs, Daniel S. Swetz, Eric R. ^M Switzer, Robert Thornton, Hy Trac, Carole Tucker, Ryan Warne, Grant Wilson, Ed Wollack, and Yue Zhao. The Atacama Cosmology Telescope: Data Characterization and Mapmaking. *The Astrophysical Journal*, 762(1):10, 2013.

[26] J. R. Bond H. M. Cho R. Datta M. J. Devlin R. Dünner A. E. Fox P. Gallardo M. Hasselfield S. Henderson G. C. Hilton A. D. Hincks R. Hlozek J. Hubmayr K. Irwin J. Klein B. Koopman D. Li M. Lungu L. Newburgh Jo. P. Nibarger M. D. Niemack L. Maurin J. McMahon S. Naess L. A. Page C. Pappas B. L. Schmitt J. Sievers S. T. Staggs R. Thornton J. Van Lanen E. J. Wollack E. Grace, J. Beall. Actpol: on-sky performance and characterization. volume 9153, pages 9153 – 9153 – 13, 2014.

[27] S. M. Duff et al. Design and Fabrication of Large-Area Transition Edge Sensor Detector Arrays for Cosmic Microwave Background Polarimetry. *J. Low Temp. Phys. in prep.*, 2017.

[28] B. Feng, M. Li, J.-Q. Xia, X. Chen, and X. Zhang. Searching for CPT Violation with Cosmic Microwave Background Data from WMAP and BOOMERANG. *Physical Review Letters*, 96(22):221302, June 2006.

[29] J. P. Filippini, P. A. R. Ade, M. Amiri, S. J. Benton, R. Bihary, J. J. Bock, J. R. Bond, J. A. Bonetti, S. A. Bryan, B. Burger, H. C. Chiang, C. R. Contaldi, B. P. Crill, O. Doré, M. Farhang, L. M. Fissel, N. N. Gandilo, S. R. Golwala, J. E. Gudmundsson, M. Halpern, M. Hasselfield, G. Hilton, W. Holmes, V. V. Hristov, K. D. Irwin, W. C. Jones, C. L. Kuo, C. J. MacTavish, P. V. Mason, T. E. Montroy, T. A. Morford, C. B. Netterfield, D. T. O'Dea, A. S. Rahlin, C. D. Reintsema, J. E. Ruhl, M. C. Runyan, M. A. Schenker, J. A. Shariff, J. D. Soler, A. Trangsrud, C. Tucker, R. S. Tucker, and A. D. Turner. SPIDER: a balloon-borne CMB polarimeter for large angular scales. In *Millimeter, Submillimeter, and Far-Infrared Detectors and Instrumentation for Astronomy V*, volume 7741 of Proc. SPIE, page 77411N, July 2010.

[30] J. W. Fowler, M. D. Niemack, S. R. Dicker, A. M. Aboobaker, P. A. R. Ade, E. S. Battistelli, M. J. Devlin, R. P. Fisher, M. Halpern, P. C. Hargrave, A. D. Hincks, M. Kaul, J. Klein, J. M. Lau, M. Limon, T. A. Marriage, P. D. Mauskopf, L. Page, S. T. Staggs, D. S. Swetz, E. R. Switzer, R. J. Thornton, and C. E. Tucker. Optical design of the Atacama Cosmology Telescope and the Millimeter Bolometric Array Camera. Appl. Opt., 46:3444–3454, June 2007.

[31] P. A. Gallardo, B. J. Koopman, N. F. Cothard, S. M. M. Bruno, G. Cortes-Medellin, G. Marchetti, K. H. Miller, B. Mockler, M. D. Niemack, G. Stacey, and E. J. Wollack. Deep reactive ion etched anti-reflection coatings for sub-millimeter silicon optics. Appl. Opt., 56, March 2017.

[32] Patricio A. Gallardo, Jon Gudmundsson, Aamir Ali, Sean Bryan, Yuji Chinone, Gabriele Coppi, Nicholas Cothard, Mark J. Devlin, Simon Dicker, Giulio Fabbian, Nicholas Galitzki, Charles Hill, Brian Keating, Akito Kusaka, Jacob Lashner, Adrian T. Lee, Michele Limon, Philip D. Mauskopf, Jeff McMahon, Federico Nati, Michael D. Niemack, John L. Orlowski-Scherer, Stephen C. Parshley, Giuseppe Puglisi, Christian L. Reichardt, Maria Salatino, Suzanne Staggs, Aritoki Suzuki, Eve M. Vavagiakis, Edward J. Wollack, Zhilei Xu, Ningfeng Zhu, Frederick T. Matsuda, Sara M. Simon, and Brian J. Koopman. Systematic uncertainties in the Simons Observatory: optical effects and sensitivity considerations. In Jonas Zmuidzinas and Jian-Rong Gao, editors, *Millimeter, Submillimeter, and Far-Infrared Detectors and Instrumentation for Astronomy IX*, page 133, Austin, United States, August 2018. SPIE.

[33] G. Gamow. Expanding Universe and the Origin of Elements. *Physical Review*, 70:572–573, October 1946.

[34] G. Gamow. The Origin of Elements and the Separation of Galaxies. *Physical Review*, 74:505–506, August 1948.

[35] M. Gell-Mann and A. Pais. Behavior of Neutral Particles under Charge Conjugation. *Physical Review*, 97(5):1387–1389, March 1955.

[36] D. Götz, P. Laurent, S. Antier, S. Covino, P. D'Avanzo, V. D'Elia, and A. Melandri. GRB 140206A: the most distant polarized gamma-ray burst. MNRAS, 444:2776–2782, November 2014.

[37] Manuel Guizar-Sicairos, Samuel T. Thurman, and James R. Fienup. Efficient subpixel image registration algorithms. *Opt. Lett.*, 33(2):156–158, Jan 2008.

[38] D. Hanson, S. Hoover, A. Crites, P. A. R. Ade, K. A. Aird, J. E. Austermann, J. A. Beall, A. N. Bender, B. A. Benson, L. E. Bleem, J. J. Bock, J. E. Carlstrom, C. L. Chang, H. C. Chiang, H.-M. Cho, A. Conley, T. M. Crawford, T. de Haan, M. A. Dobbs, W. Everett, J. Gallicchio, J. Gao, E. M. George, N. W. Halverson, N. Harrington, J. W. Henning, G. C. Hilton, G. P. Holder, W. L. Holzapfel, J. D. Hrubes, N. Huang, J. Hubmayr, K. D.

Irwin, R. Keisler, L. Knox, A. T. Lee, E. Leitch, D. Li, C. Liang, D. Luong-Van, G. Marsden, J. J. McMahon, J. Mehl, S. S. Meyer, L. Mocanu, T. E. Montroy, T. Natoli, J. P. Nibarger, V. Novosad, S. Padin, C. Pryke, C. L. Reichardt, J. E. Ruhl, B. R. Saliwanchik, J. T. Sayre, K. K. Schaffer, B. Schulz, G. Smecher, A. A. Stark, K. T. Story, C. Tucker, K. Vanderlinde, J. D. Vieira, M. P. Viero, G. Wang, V. Yefremenko, O. Zahn, and M. Zemcov. Detection of B-Mode Polarization in the Cosmic Microwave Background with Data from the South Pole Telescope. *Physical Review Letters*, 111(14):141301, October 2013.

[39] S. W. Henderson, R. Allison, J. Austermann, T. Baildon, N. Battaglia, J. A. Beall, D. Becker, F. De Bernardis, J. R. Bond, E. Calabrese, S. K. Choi, K. P. Coughlin, K. T. Crowley, R. Datta, M. J. Devlin, S. M. Duff, J. Dunkley, R. Dünner, A. van Engelen, P. A. Gallardo, E. Grace, M. Hasselfield, F. Hills, G. C. Hilton, A. D. Hincks, R. Hlozek, S. P. Ho, J. Hubmayr, K. Huffenberger, J. P. Hughes, K. D. Irwin, B. J. Koopman, A. B. Kosowsky, D. Li, J. McMahon, C. Munson, F. Nati, L. Newburgh, M. D. Niemack, P. Niraula, L. A. Page, C. G. Pappas, M. Salatino, A. Schillaci, B. L. Schmitt, N. Sehgal, B. D. Sherwin, J. L. Sievers, S. M. Simon, D. N. Spergel, S. T. Staggs, J. R. Stevens, R. Thornton, J. Van Lanen, E. M. Vavagiakis, J. T. Ward, and E. J. Wollack. Advanced actpol cryogenic detector arrays and readout. *Journal of Low Temperature Physics*, 184(3):772–779, Aug 2016.

[40] S. W. Henderson, J. R. Stevens, M. Amiri, J. Austermann, J. A. Beall, S. Chaudhuri, H.-M. Cho, S. K. Choi, N. F. Cothard, K. T. Crowley, S. M. Duff, C. P. Fitzgerald, P. A. Gallardo, M. Halpern, M. Hasselfield, G. Hilton, S.-P. P. Ho, J. Hubmayr, K. D. Irwin, B. J. Koopman, D. Li, Y. Li, J. McMahon, F. Nati, M. Niemack, C. D. Reintsema, M. Salatino, A. Schillaci, B. L. Schmitt, S. M. Simon, S. T. Staggs, E. M. Vavagiakis, and J. T. Ward. Readout of two-kilopixel transition-edge sensor arrays for Advanced ACTPol. In *Millimeter, Submillimeter, and Far-Infrared Detectors and Instrumentation for Astronomy VIII*, volume 9914 of Proc. SPIE, page 99141G, July 2016.

[41] J. Jeff Hester. The Crab Nebula: An Astrophysical Chimera. *Annual Review of Astronomy and Astrophysics*, 46(1):127–155, September 2008.

[42] A. D. Hincks. *Toward a mass-limited catalog of galaxy clusters from the Atacama Cosmology Telescope*. PhD Thesis, Princeton University, 2009.

[43] G. Hinshaw, D. Larson, E. Komatsu, D. N. Spergel, C. L. Bennett, J. Dunkley, M. R. Nolta, M. Halpern, R. S. Hill, N. Odegard, L. Page, K. M. Smith, J. L. Weiland, B. Gold, N. Jarosik, A. Kogut, M. Limon, S. S. Meyer, G. S.

Tucker, E. Wollack, and E. L. Wright. Nine-year Wilkinson Microwave Anisotropy Probe (WMAP) Observations: Cosmological Parameter Results. ApJS, 208:19, October 2013.

[44] S. P. Ho, C. G. Pappas, J. Austermann, J. A. Beall, D. Becker, S. K. Choi, R. Datta, S. M. Duff, P. A. Gallardo, E. Grace, M. Hasselfield, S. W. Henderson, G. C. Hilton, J. Hubmayr, B. J. Koopman, J. V. Lanen, D. Li, J. McMahon, F. Nati, M. D. Niemack, P. Niraula, M. Salatino, A. Schillaci, B. L. Schmitt, S. M. Simon, S. T. Staggs, J. R. Stevens, J. T. Ward, E. J. Wollack, and E. M. Vavagiakis. The first multichroic polarimeter array on the atacama cosmology telescope: Characterization and performance. *Journal of Low Temperature Physics*, 184(3):559–567, Aug 2016.

[45] Wayne Hu and Martin White. Cmb anisotropies: Total angular momentum method. *Phys. Rev. D*, 56:596–615, Jul 1997.

[46] E. Hubble. A Relation between Distance and Radial Velocity among Extra-Galactic Nebulae. *Proceedings of the National Academy of Science*, 15:168–173, March 1929.

[47] K. M. Huffenberger and S. K. Næss. Cosmic Microwave Background Mapmaking with a Messenger Field. ApJ, 852:92, January 2018.

[48] K. D. Irwin, G. C. Hilton, D. A. Wollman, and John M. Martinis. Thermal-response time of superconducting transition-edge microcalorimeters. *Journal of Applied Physics*, 83(8):3978–3985, 1998.

[49] K.D. Irwin and G.C. Hilton. *Transition-Edge Sensors*, pages 63–150. Springer Berlin Heidelberg, Berlin, Heidelberg, 2005.

[50] B. R. Johnson, C. J. Vourch, T. D. Drysdale, A. Kalman, S. Fujikawa, B. Keating, and J. Kaufman. A CubeSat for Calibrating Ground-Based and Sub-Orbital Millimeter-Wave Polarimeters (CalSat). *Journal of Astronomical Instrumentation*, 4:1550007–65, October 2015.

[51] James A. Beall Steve K. Choi Kevin T. Crowley Mark J. Devlin Shannon M. Duff Patricio A. Gallardo Shawn W. Henderson Shuay-Pwu Patty Ho Gene Hilton Johannes Hubmayr Niloufar Khavari Jeffrey Klein Brian J. Koopman Dale Li Jeffrey McMahon Grace Mumby Federico Nati Michael D. Niemack Lyman A. Page Maria Salatino Alessandro Schillaci Benjamin L. Schmitt Sara M. Simon Suzanne T. Staggs Robert Thornton Joel N. Ullom Eve M. Vavagiakis Edward J. Wollack Jonathan T. Ward, Jason Auster-

mann. Mechanical designs and development of tes bolometer detector arrays for the advanced actpol experiment. volume 9914, pages 9914 – 9914 – 9, 2016.

[52] M. Kamionkowski and E. D. Kovetz. The Quest for B Modes from Inflationary Gravitational Waves. ARA&A, 54:227–269, September 2016.

[53] Marc Kamionkowski, Arthur Kosowsky, and Albert Stebbins. A probe of primordial gravity waves and vorticity. *Phys. Rev. Lett.*, 78:2058–2061, Mar 1997.

[54] J. Kaufman, B. Keating, and B. Johnson. Precision Tests of Parity Violation Over Cosmological Distances. *ArXiv e-prints*, page 0, September 2014.

[55] J. P. Kaufman, B. G. Keating, and B. R. Johnson. Precision tests of parity violation over cosmological distances. MNRAS, 455:1981–1988, January 2016.

[56] J. P. Kaufman, N. J. Miller, M. Shimon, D. Barkats, C. Bischoff, I. Buder, B. G. Keating, J. M. Kovac, P. A. R. Ade, R. Aikin, J. O. Battle, E. M. Bierman, J. J. Bock, H. C. Chiang, C. D. Dowell, L. Duband, J. Filippini, E. F. Hivon, W. L. Holzapfel, V. V. Hristov, W. C. Jones, S. S. Kernasovskiy, C. L. Kuo, E. M. Leitch, P. V. Mason, T. Matsumura, H. T. Nguyen, N. Ponthieu, C. Pryke, S. Richter, G. Rocha, C. Sheehy, M. Su, Y. D. Takahashi, J. E. Tolan, and K. W. Yoon. Self-calibration of BICEP1 three-year data and constraints on astrophysical polarization rotation. Phys. Rev. D, 89(6):062006, March 2014.

[57] B. G. Keating, M. Shimon, and A. P. S. Yadav. Self-calibration of Cosmic Microwave Background Polarization Experiments. ApJ, 762:L23, January 2013.

[58] W. C. Keel. *The road to galaxy formation*. 2007.

[59] Jeffrey Kuan Jason A. Austermann James A. Beall Rahul Datta Shannon M. Duff Patricio A. Gallardo Matthew Hasselfield Shawn W. Henderson-Shuay-Pwu P. Ho Brian J. Koopman Michael D. Niemack Maria Salatino Sara M. Simon Suzanne T. Staggs Edward J. Wollack Kevin T. Crowley, Steve K. Choi. Characterization of almn tes impedance, noise, and optical efficiency in the first 150 mm multichroic array for advanced actpol. volume 9914, pages 9914 – 9914 – 12, 2016.

[60] E. Komatsu, K. M. Smith, J. Dunkley, C. L. Bennett, B. Gold, G. Hinshaw, N. Jarosik, D. Larson, M. R. Nolta, L. Page, D. N. Spergel, M. Halpern, R. S. Hill, A. Kogut, M. Limon, S. S. Meyer, N. Odegard, G. S. Tucker, J. L. Weiland, E. Wollack, and E. L. Wright. Seven-year Wilkinson Microwave Anisotropy Probe (WMAP) Observations: Cosmological Interpretation. ApJS, 192:18, February 2011.

[61] B. Koopman, J. Austermann, H.-M. Cho, K. P. Coughlin, S. M. Duff, P. A. Gallardo, M. Hasselfield, S. W. Henderson, S.-P. P. Ho, J. Hubmayr, K. D. Irwin, D. Li, J. McMahon, F. Nati, M. D. Niemack, L. Newburgh, L. A. Page, M. Salatino, A. Schillaci, B. L. Schmitt, S. M. Simon, E. M. Vavagiakis, J. T. Ward, and E. J. Wollack. Optical modeling and polarization calibration for CMB measurements with ACTPol and Advanced ACTPol. In *Millimeter, Submillimeter, and Far-Infrared Detectors and Instrumentation for Astronomy VIII*, volume 9914 of Proc. SPIE, page 99142T, July 2016.

[62] B. J. Koopman, N. F. Cothard, S. K. Choi, K. T. Crowley, S. M. Duff, S. W. Henderson, S. P. Ho, J. Hubmayr, P. A. Gallardo, F. Nati, M. D. Niemack, S. M. Simon, S. T. Staggs, J. R. Stevens, E. M. Vavagiakis, and E. J. Wollack. Advanced ACTPol Low-Frequency Array: Readout and Characterization of Prototype 27 and 39 GHz Transition Edge Sensors. *Journal of Low Temperature Physics*, May 2018.

[63] J. M. Kovac, E. M. Leitch, C. Pryke, J. E. Carlstrom, N. W. Halverson, and W. L. Holzapfel. Detection of polarization in the cosmic microwave background using DASI. Nature, 420:772–787, December 2002.

[64] J. Krupka, J. Breeze, A. Centeno, N. Alford, T. Claussen, and L. Jensen. Measurements of Permittivity, Dielectric Loss Tangent, and Resistivity of Float-Zone Silicon at Microwave Frequencies. *IEEE Transactions on Microwave Theory and Techniques*, 54(11):3995–4001, November 2006.

[65] A. Kusaka, J. Appel, T. Essinger-Hileman, J. A. Beall, L. E. Campusano, H.-M. Cho, S. K. Choi, K. Crowley, J. W. Fowler, P. Gallardo, M. Hasselfield, G. Hilton, S.-P. P. Ho, K. Irwin, N. Jarosik, M. D. Niemack, G. W. Nixon, M. Nolta, L. A. Page, Jr, G. A. Palma, L. Parker, S. Raghunathan, C. D. Reintsema, J. Sievers, S. M. Simon, S. T. Staggs, K. Visnjic, and K.-W. Yoon. Results from the Atacama B-mode Search (ABS) Experiment. *ArXiv e-prints*, January 2018.

[66] A. Kusaka, T. Essinger-Hileman, J. W. Appel, P. Gallardo, K. D. Irwin, N. Jarosik, M. R. Nolta, L. A. Page, L. P. Parker, S. Raghunathan, J. L. Sievers, S. M. Simon, S. T. Staggs, and K. Visnjic. Modulation of cosmic

microwave background polarization with a warm rapidly rotating half-wave plate on the Atacama B-Mode Search instrument. *Review of Scientific Instruments*, 85(2):024501, February 2014.

[67] J. P. Leahy. Comment on the Measurement of Cosmological Birefringence. *ArXiv Astrophysics e-prints*, April 1997.

[68] Dale Li, Jason E. Austermann, James A. Beall, Daniel T. Becker, Shannon M. Duff, Patricio A. Gallardo, Shawn W. Henderson, Gene C. Hilton, Shuay-Pwu Ho, Johannes Hubmayr, Brian J. Koopman, Jeffrey J. McMahon, Federico Nati, Michael D. Niemack, Christine G. Pappas, Maria Salatino, Benjamin L. Schmitt, Sara M. Simon, Suzanne T. Staggs, Jeff Van Lanen, Jonathan T. Ward, and Edward J. Wollack. Almn transition edge sensors for advanced actpol. *Journal of Low Temperature Physics*, 184(1):66–73, Jul 2016.

[69] Y. Li, J. E. Austermann, J. A. Beall, S. M. Bruno, S. K. Choi, N. F. Cothard, K. T. Crowley, S. M. Duff, P. A. Gallardo, S. W. Henderson, S.-P. P. Ho, J. Hubmayr, B. J. Koopman, J. J. McMahon, M. D. Niemack, M. Salatino, S. M. Simon, S. T. Staggs, J. R. Stevens, J. N. Ullom, J. Ward, and E. J. Wollack. Performance of the advanced ACTPol low frequency array. In *Millimeter, Submillimeter, and Far-Infrared Detectors and Instrumentation for Astronomy IX*, volume 10708 of *Society of Photo-Optical Instrumentation Engineers (SPIE) Conference Series*, page 107080A, July 2018.

[70] A. P. Lobanov, D. Horns, and T. W. B. Muxlow. VLBI imaging of a flare in the Crab nebula: more than just a spot. A&A, 533:A10, September 2011.

[71] Thibaut Louis, Emily Grace, Matthew Hasselfield, Marius Lungu, Loïc Maurin, Graeme E. Addison, Peter A. R. Ade, Simone Aiola, Rupert Allison, Mandana Amiri, Elio Angile, Nicholas Battaglia, James A. Beall, Francesco de Bernardis, J Richard Bond, Joe Britton, Erminia Calabrese, Hsiao-mei Cho, Steve K. Choi, Kevin Coughlin, Devin Crichton, Kevin Crowley, Rahul Datta, Mark J. Devlin, Simon R. Dicker, Joanna Dunkley, Rolando Dünner, Simone Ferraro, Anna E. Fox, Patricio Gallardo, Megan Gralla, Mark Halpern, Shawn Henderson, J. Colin Hill, Gene C. Hilton, Matt Hilton, Adam D. Hincks, Renée Hlozek, S.P. Patty Ho, Zhiqi Huang, Johannes Hubmayr, Kevin M. Huffenberger, John P. Hughes, Leopoldo Infante, Kent Irwin, Simon Muya Kasanda, Jeff Klein, Brian Koopman, Arthur Kosowsky, Dale Li, Mathew Madhavacheril, Tobias A. Marriage, Jeff McMahon, Felipe Menanteau, Kavilan Moodley, Charles Munson, Sigurd Naess, Federico Nati, Laura Newburgh, John Nibarger, Michael D. Niemack, Michael R. Nolta, Carolina Nuñez, Lyman A. Page, Christine

Pappas, Bruce Partridge, Felipe Rojas, Emmanuel Schaan, Benjamin L. Schmitt, Neelima Sehgal, Blake D. Sherwin, Jon Sievers, Sara Simon, David N. Spergel, Suzanne T. Staggs, Eric R. Switzer, Robert Thornton, Hy Trac, Jesse Treu, Carole Tucker, Alexander Van Engelen, Jonathan T. Ward, and Edward J. Wollack. The Atacama Cosmology Telescope: two-season ACTPol spectra and parameters. *Journal of Cosmology and Astroparticle Physics*, 2017(06):031–031, June 2017.

[72] Arthur Lue, Limin Wang, and Marc Kamionkowski. Cosmological signature of new parity-violating interactions. *Phys. Rev. Lett.*, 83:1506–1509, Aug 1999.

[73] G.G. Macfarlane. Surface impedance of an infinite parallel-wire grid at oblique angles of incidence. *Journal of the Institution of Electrical Engineers - Part IIIA: Radiolocation*, 93(10):1523–1527, 1946.

[74] J. F. Macías-Pérez, F. Mayet, J. Aumont, and F.-X. Désert. Global spectral energy distribution of the crab nebula in the prospect of the planck satellite polarization calibration. *The Astrophysical Journal*, 711(1):417, 2010.

[75] A. Manzotti, K. T. Story, W. L. K. Wu, J. E. Austermann, J. A. Beall, A. N. Bender, B. A. Benson, L. E. Bleem, J. J. Bock, J. E. Carlstrom, C. L. Chang, H. C. Chiang, H.-M. Cho, R. Citron, A. Conley, T. M. Crawford, A. T. Crites, T. de Haan, M. A. Dobbs, S. Dodelson, W. Everett, J. Gallicchio, E. M. George, A. Gilbert, N. W. Halverson, N. Harrington, J. W. Henning, G. C. Hilton, G. P. Holder, W. L. Holzapfel, S. Hoover, Z. Hou, J. D. Hrubes, N. Huang, J. Hubmayr, K. D. Irwin, R. Keisler, L. Knox, A. T. Lee, E. M. Leitch, D. Li, J. J. McMahon, S. S. Meyer, L. M. Mocanu, T. Natoli, J. P. Nibarger, V. Novosad, S. Padin, C. Pryke, C. L. Reichardt, J. E. Ruhl, B. R. Saliwanchik, J. T. Sayre, K. K. Schaffer, G. Smecher, A. A. Stark, K. Vanderlinde, J. D. Vieira, M. P. Viero, G. Wang, N. Whitehorn, V. Yefremenko, and M. Zemcov. CMB Polarization B-mode Delensing with SPTpol and Herschel. ApJ, 846:45, September 2017.

[76] S. Naess, M. Hasselfield, J. McMahon, M. D. Niemack, G. E. Addison, P. A. R. Ade, R. Allison, M. Amiri, N. Battaglia, J. A. Beall, F. de Bernardis, J. R. Bond, J. Britton, E. Calabrese, H.-m. Cho, K. Coughlin, D. Crichton, S. Das, R. Datta, M. J. Devlin, S. R. Dicker, J. Dunkley, R. Dünner, J. W. Fowler, A. E. Fox, P. Gallardo, E. Grace, M. Gralla, A. Hajian, M. Halpern, S. Henderson, J. C. Hill, G. C. Hilton, M. Hilton, A. D. Hincks, R. Hlozek, P. Ho, J. Hubmayr, K. M. Huffenberger, J. P. Hughes, L. Infante, K. Irwin, R. Jackson, S. Muya Kasanda, J. Klein, B. Koopman, A. Kosowsky, D. Li, T. Louis, M. Lungu, M. Madhavacheril, T. A. Marriage, L. Maurin,

F. Menanteau, K. Moodley, C. Munson, L. Newburgh, J. Nibarger, M. R. Nolta, L. A. Page, C. Pappas, B. Partridge, F. Rojas, B. L. Schmitt, N. Sehgal, B. D. Sherwin, J. Sievers, S. Simon, D. N. Spergel, S. T. Staggs, E. R. Switzer, R. Thornton, H. Trac, C. Tucker, M. Uehara, A. Van Engelen, J. T. Ward, and E. J. Wollack. The Atacama Cosmology Telescope: CMB polarization at $200 < l < 9000$. J. Cosmology Astropart. Phys., 10:7, October 2014.

[77] F. Nati, M. J. Devlin, M. Gerbino, B. R. Johnson, B. Keating, L. Pagano, and G. Teply. POLOCALC: A Novel Method to Measure the Absolute Polarization Orientation of the Cosmic Microwave Background. *Journal of Astronomical Instrumentation*, 6:1740008, 2017.

[78] J. Papez, L. Grigori, and R. Stompor. Solving linear equations with messenger-field and conjugate gradients techniques - an application to CMB data analysis. *ArXiv e-prints*, March 2018.

[79] C. G. Pappas, J. Austermann, J. A. Beall, S. M. Duff, P. A. Gallardo, E. Grace, S. W. Henderson, S. P. Ho, B. J. Koopman, D. Li, J. McMahon, F. Nati, M. D. Niemack, P. Niraula, M. Salatino, A. Schillaci, B. L. Schmitt, S. M. Simon, S. T. Staggs, J. R. Stevens, E. M. Vavagiakis, J. T. Ward, and E. J. Wollack. High-density superconducting cables for advanced actpol. *Journal of Low Temperature Physics*, 184(1):473–479, Jul 2016.

[80] V. V. Parshin, R. Heidinger, B. A. Andreev, A. V. Gusev, and V. B. Shmagin. Silicon as an advanced window material for high power gyrotrons. *International Journal of Infrared and Millimeter Waves*, 16(5):863–877, May 1995.

[81] S. C. Parshley, M. D. Niemack, R. Hills, S. R. Dicker, R. Dünner, J. Erler, P. A. Gallardo, J. E. Gudmundsson, T. Herter, B. J. Koopman, M. Limon, F. T. Matsuda, P. Mauskopf, D. A. Riechers, G. J. Stacey, and E. M. Vavagiakis. The optical design of the six-meter CCAT-prime and Simons Observatory telescopes. *ArXiv e-prints*, July 2018.

[82] A. A. Penzias and R. W. Wilson. A Measurement of Excess Antenna Temperature at 4080 Mc/s. ApJ, 142:419–421, July 1965.

[83] Planck Collaboration, P. A. R. Ade, N. Aghanim, F. Argüeso, M. Arnaud, M. Ashdown, J. Aumont, C. Baccigalupi, A. J. Banday, R. B. Barreiro, N. Bartolo, E. Battaner, C. Beichman, K. Benabed, A. Benoît, A. Benoit-Lévy, J.-P. Bernard, M. Bersanelli, P. Bielewicz, J. J. Bock, H. Böhringer, A. Bonaldi, L. Bonavera, J. R. Bond, J. Borrill, F. R. Bouchet, F. Boulanger,

M. Bucher, C. Burigana, R. C. Butler, E. Calabrese, J.-F. Cardoso, P. Carvalho, A. Catalano, A. Challinor, A. Chamballu, R.-R. Chary, H. C. Chiang, P. R. Christensen, M. Clemens, D. L. Clements, S. Colombi, L. P. L. Colombo, C. Combet, F. Couchot, A. Coulais, B. P. Crill, A. Curto, F. Cuttaia, L. Danese, R. D. Davies, R. J. Davis, P. de Bernardis, A. de Rosa, G. de Zotti, J. Delabrouille, F.-X. Désert, C. Dickinson, J. M. Diego, H. Dole, S. Donzelli, O. Doré, M. Douspis, A. Ducout, X. Dupac, G. Efstathiou, F. Elsner, T. A. Enßlin, H. K. Eriksen, E. Falgarone, J. Fergusson, F. Finelli, O. Forni, M. Frailis, A. A. Fraisse, E. Franceschi, A. Frejsel, S. Galeotta, S. Galli, K. Ganga, M. Giard, Y. Giraud-Héraud, E. Gjerløw, J. González-Nuevo, K. M. Górski, S. Gratton, A. Gregorio, A. Gruppuso, J. E. Gudmundsson, F. K. Hansen, D. Hanson, D. L. Harrison, G. Helou, S. Henrot-Versillé, C. Hernández-Monteagudo, D. Herranz, S. R. Hildebrandt, E. Hivon, M. Hobson, W. A. Holmes, A. Hornstrup, W. Hovest, K. M. Huffenberger, G. Hurier, A. H. Jaffe, T. R. Jaffe, W. C. Jones, M. Juvela, E. Keihänen, R. Keskitalo, T. S. Kisner, R. Kneissl, J. Knoche, M. Kunz, H. Kurki-Suonio, G. Lagache, A. Lähteenmäki, J.-M. Lamarre, A. Lasenby, M. Lattanzi, C. R. Lawrence, J. P. Leahy, R. Leonardi, J. León-Tavares, J. Lesgourgues, F. Levrier, M. Liguori, P. B. Lilje, M. Linden-Vørnle, M. López-Caniego, P. M. Lubin, J. F. Macías-Pérez, G. Maggio, D. Maino, N. Mandolesi, A. Mangilli, M. Maris, D. J. Marshall, P. G. Martin, E. Martínez-González, S. Masi, S. Matarrese, P. McGehee, P. R. Meinhold, A. Melchiorri, L. Mendes, A. Mennella, M. Migliaccio, S. Mitra, M.-A. Miville-Deschênes, A. Moneti, L. Montier, G. Morgante, D. Mortlock, A. Moss, D. Munshi, J. A. Murphy, P. Naselsky, F. Nati, P. Natoli, M. Negrello, C. B. Netterfield, H. U. Nørgaard-Nielsen, F. Noviello, D. Novikov, I. Novikov, C. A. Oxborrow, F. Paci, L. Pagano, F. Pajot, R. Paladini, D. Paoletti, B. Partridge, F. Pasian, G. Patanchon, T. J. Pearson, O. Perdereau, L. Perotto, F. Perrotta, V. Pettorino, F. Piacentini, M. Piat, E. Pierpaoli, D. Pietrobon, S. Plaszczynski, E. Pointecouteau, G. Polenta, G. W. Pratt, G. Prézeau, S. Prunet, J.-L. Puget, J. P. Rachen, W. T. Reach, R. Rebolo, M. Reinecke, M. Remazeilles, C. Renault, A. Renzi, I. Ristorcelli, G. Rocha, C. Rosset, M. Rossetti, G. Roudier, M. Rowan-Robinson, J. A. Rubiño-Martín, B. Rusholme, M. Sandri, H. S. Sanghera, D. Santos, M. Savelainen, G. Savini, D. Scott, M. D. Seiffert, E. P. S. Shellard, L. D. Spencer, V. Stolyarov, R. Sudiwala, R. Sunyaev, D. Sutton, A.-S. Suur-Uski, J.-F. Sygnet, J. A. Tauber, L. Terenzi, L. Toffolatti, M. Tomasi, M. Tornikoski, M. Tristram, M. Tucci, J. Tuovinen, M. Türler, G. Umana, L. Valenziano, J. Valiviita, B. Van Tent, P. Vielva, F. Villa, L. A. Wade, B. Walter, B. D. Wandelt, I. K. Wehus, D. Yvon, A. Zacchei, and A. Zonca. Planck 2015 results: XXVI. The Second Planck Catalogue of Compact Sources. *Astronomy & Astrophysics*, 594:A26, October 2016.

[84] Planck Collaboration, P. A. R. Ade, N. Aghanim, M. Arnaud, M. Ashdown, J. Aumont, C. Baccigalupi, A. J. Banday, R. B. Barreiro, J. G. Bartlett, and et al. Planck 2015 results. XIII. Cosmological parameters. A&A, 594:A13, September 2016.

[85] Planck Collaboration, Y. Akrami, F. Arroja, M. Ashdown, J. Aumont, C. Baccigalupi, M. Ballardini, A. J. Banday, R. B. Barreiro, N. Bartolo, S. Basak, K. Benabed, J.-P. Bernard, M. Bersanelli, P. Bielewicz, J. J. Bock, J. R. Bond, J. Borrill, F. R. Bouchet, F. Boulanger, M. Bucher, C. Burigana, R. C. Butler, E. Calabrese, J.-F. Cardoso, J. Carron, A. Challinor, H. C. Chiang, L. P. L. Colombo, C. Combet, D. Contreras, B. P. Crill, F. Cuttaia, P. de Bernardis, G. de Zotti, J. Delabrouille, J.-M. Delouis, E. Di Valentino, J. M. Diego, S. Donzelli, O. Doré, M. Douspis, A. Ducout, X. Dupac, S. Dusini, G. Efstathiou, F. Elsner, T. A. Enßlin, H. K. Eriksen, Y. Fantaye, J. Fergusson, R. Fernandez-Cobos, F. Finelli, F. Forastieri, M. Frailis, E. Franceschi, A. Frolov, S. Galeotta, S. Galli, K. Ganga, C. Gauthier, R. T. Génova-Santos, M. Gerbino, T. Ghosh, J. González-Nuevo, K. M. Górski, S. Gratton, A. Gruppuso, J. E. Gudmundsson, J. Hamann, W. Handley, F. K. Hansen, D. Herranz, E. Hivon, D. C. Hooper, Z. Huang, A. H. Jaffe, W. C. Jones, E. Keihänen, R. Keskitalo, K. Kiiveri, J. Kim, T. S. Kisner, N. Krachmalnicoff, M. Kunz, H. Kurki-Suonio, G. Lagache, J.-M. Lamarre, A. Lasenby, M. Lattanzi, C. R. Lawrence, M. Le Jeune, J. Lesgourgues, F. Levrier, A. Lewis, M. Liguori, P. B. Lilje, V. Lindholm, M. Lpez-Caniego, P. M. Lubin, Y.-Z. Ma, J. F. Macías-Pérez, G. Maggio, D. Maino, N. Mandolesi, A. Mangilli, A. Marcos-Caballero, M. Maris, P. G. Martin, E. Martínez-González, S. Matarrese, N. Mauri, J. D. McEwen, P. D. Meerburg, P. R. Meinhold, A. Melchiorri, A. Mennella, M. Migliaccio, S. Mitra, M.-A. Miville-Deschênes, D. Molinari, A. Moneti, L. Montier, G. Morgante, A. Moss, M. Münchmeyer, P. Natoli, H. U. Nørgaard-Nielsen, L. Pagano, D. Paoletti, B. Partridge, G. Patanchon, H. V. Peiris, F. Perrotta, V. Pettorino, F. Piacentini, L. Polastri, G. Polenta, J.-L. Puget, J. P. Rachen, M. Reinecke, M. Remazeilles, A. Renzi, G. Rocha, C. Rosset, G. Roudier, J. A. Rubiño-Martín, B. Ruiz-Granados, L. Salvati, M. Sandri, M. Savelainen, D. Scott, E. P. S. Shellard, M. Shiraishi, C. Sirignano, G. Sirri, L. D. Spencer, R. Sunyaev, A.-S. Suur-Uski, J. A. Tauber, D. Tavagnacco, M. Tenti, L. Toffolatti, M. Tomasi, T. Trombetti, J. Valiviita, B. Van Tent, P. Vielva, F. Villa, N. Vittorio, B. D. Wandelt, I. K. Wehus, S. D. M. White, A. Zacchei, J. P. Zibin, and A. Zonca. Planck 2018 results. X. Constraints on inflation. *ArXiv e-prints*, July 2018.

[86] Polarbear Collaboration, P. A. R. Ade, Y. Akiba, A. E. Anthony, K. Arnold, M. Atlas, D. Barron, D. Boettger, J. Borrill, S. Chapman, Y. Chinone, M. Dobbs, T. Elleflot, J. Errard, G. Fabbian, C. Feng, D. Flanigan,

A. Gilbert, W. Grainger, N. W. Halverson, M. Hasegawa, K. Hattori, M. Hazumi, W. L. Holzapfel, Y. Hori, J. Howard, P. Hyland, Y. Inoue, G. C. Jaehnig, A. H. Jaffe, B. Keating, Z. Kermish, R. Keskitalo, T. Kisner, M. Le Jeune, A. T. Lee, E. M. Leitch, E. Linder, M. Lungu, F. Matsuda, T. Matsumura, X. Meng, N. J. Miller, H. Morii, S. Moyerman, M. J. Myers, M. Navaroli, H. Nishino, A. Orlando, H. Paar, J. Peloton, D. Poletti, E. Quealy, G. Rebeiz, C. L. Reichardt, P. L. Richards, C. Ross, I. Schanning, D. E. Schenck, B. D. Sherwin, A. Shimizu, C. Shimmin, M. Shimon, P. Siritanasak, G. Smecher, H. Spieler, N. Stebor, B. Steinbach, R. Stompor, A. Suzuki, S. Takakura, T. Tomaru, B. Wilson, A. Yadav, and O. Zahn. A Measurement of the Cosmic Microwave Background B-mode Polarization Power Spectrum at Sub-degree Scales with POLARBEAR. ApJ, 794:171, October 2014.

[87] A. Ritacco, J. F. Macías Pérez, N. Ponthieu, R. Adam, P. Ade, P. André, J. Aumont, A. Beelen, A. Benoît, A. Bideaud, N. Billot, O. Bourrion, A. Bracco, M. Calvo, A. Catalano, G. Coiffard, B. Comis, A. D'Addabbo, M. De Petris, F. X. Désert, S. Doyle, J. Goupy, C. Kramer, G. Lagache, S. Leclercq, J. F. Lestrade, P. Mauskopf, F. Mayet, A. Maury, A. Monfardini, F. Pajot, E. Pascale, L. Perotto, G. Pisano, M. Rebolo Iglesias, V. Revéret, L. Rodriguez, C. Romero, H. Roussel, F. Ruppin, K. Schuster, A. Sievers, G. Siringo, C. Thum, S. Triqueneaux, C. Tucker, H. Wiesemeyer, and R. Zylka. NIKA 150 GHz polarization observations of the Crab nebula and its Spectral Energy Distribution. *ArXiv e-prints*, April 2018.

[88] C. Rosset, M. Tristram, N. Ponthieu, P. Ade, J. Aumont, A. Catalano, L. Conversi, F. Couchot, B. P. Crill, F.-X. Désert, K. Ganga, M. Giard, Y. Giraud-Héraud, J. Haïssinski, S. Henrot-Versillé, W. Holmes, W. C. Jones, J.-M. Lamarre, A. Lange, C. Leroy, J. Macías-Pérez, B. Maffei, P. de Marcillac, M.-A. Miville-Deschênes, L. Montier, F. Noviello, F. Pajot, O. Perdereau, F. Piacentini, M. Piat, S. Plaszczynski, E. Pointecouteau, J.-L. Puget, I. Ristorcelli, G. Savini, R. Sudiwala, M. Veneziani, and D. Yvon. Planck pre-launch status: High Frequency Instrument polarization calibration. *Astronomy and Astrophysics*, 520:A13, September 2010.

[89] James A. Beall Steve K Choi Kevin P. Coughlin Shannon M. Duff Patricio A. Gallardo Shawn W. Henderson Felicity B. Hills Shuay-Pwu Patty Ho Johannes Hubmayr Alec Josaitis Brian J. Koopman Jeff J. McMahon Federico Nati Laura Newburgh Michael D. Niemack Maria Salatino Alessandro Schillaci Benjamin L. Schmitt Suzanne T. Staggs Eve M. Vavagiakis Jonathan Ward Edward J. Wollack Sara M. Simon, Jason Austermann. The design and characterization of wideband spline-profiled feedhorns for advanced actpol. volume 9914, pages 9914 – 9914 – 13, 2016.

[90] James A. Beall Steve K. Choi Nicholas F. Cothard Kevin T. Crowley Rahul Datta Mark J. Devlin Shannon M. Duff Patricio A. Gallardo Matthew Hasselfield Shawn W. Henderson Gene Hilton Johannes Hubmayr Brian J. Koopman Yaqiong Li Jeffrey McMahon Michael D. Niemack Maria Salatino Sara M. Simon Suzanne T. Staggs Jonathan T. Ward Joel N. Ullom Eve M. Vavagiakis Edward J. Wollack Shuay-Pwu Patty Ho, Jason Austermann. Highly uniform 150 mm diameter multichroic polarimeter array deployed for cmb detection. volume 9914, pages 9914 – 9914 – 15, 2017.

[91] S. M. Simon, J. A. Beall, E. M. Vavagiakis, S. M. Duff, J. Hubmayr, M. D. Niemack, P. A. Gallardo, N. F. Cothard, and B. J. Koopman. The advanced actpol 27/39 ghz array. *J. Low Temp. Phys. in prep.*, 2017.

[92] D. S. Swetz, P. A. R. Ade, M. Amiri, J. W. Appel, E. S. Battistelli, B. Burger, J. Chervenak, M. J. Devlin, S. R. Dicker, W. B. Doriese, R. Dünner, T. Essinger-Hileman, R. P. Fisher, J. W. Fowler, M. Halpern, M. Hasselfield, G. C. Hilton, A. D. Hincks, K. D. Irwin, N. Jarosik, M. Kaul, J. Klein, J. M. Lau, M. Limon, T. A. Marriage, D. Marsden, K. Martocci, P. Mauskopf, H. Moseley, C. B. Netterfield, M. D. Niemack, M. R. Nolta, L. A. Page, L. Parker, S. T. Staggs, O. Stryzak, E. R. Switzer, R. Thornton, C. Tucker, E. Wollack, and Y. Zhao. Overview of the Atacama Cosmology Telescope: Receiver, Instrumentation, and Telescope Systems. *The Astrophysical Journal Supplement Series*, 194(2):41, June 2011.

[93] M. Tegmark and A. de Oliveira-Costa. How to measure CMB polarization power spectra without losing information. Phys. Rev. D, 64(6):063001, September 2001.

[94] The Polarbear Collaboration: P. A. R. Ade, Y. Akiba, A. E. Anthony, K. Arnold, M. Atlas, D. Barron, D. Boettger, J. Borrill, S. Chapman, Y. Chinone, M. Dobbs, T. Elleflot, J. Errard, G. Fabbian, C. Feng, D. Flanigan, A. Gilbert, W. Grainger, N. W. Halverson, M. Hasegawa, K. Hattori, M. Hazumi, W. L. Holzapfel, Y. Hori, J. Howard, P. Hyland, Y. Inoue, G. C. Jaehnig, A. H. Jaffe, B. Keating, Z. Kermish, R. Keskitalo, T. Kisner, M. Le Jeune, A. T. Lee, E. M. Leitch, E. Linder, M. Lungu, F. Matsuda, T. Matsumura, X. Meng, N. J. Miller, H. Morii, S. Moyerman, M. J. Myers, M. Navaroli, H. Nishino, A. Orlando, H. Paar, J. Peloton, D. Poletti, E. Quealy, G. Rebeiz, C. L. Reichardt, P. L. Richards, C. Ross, I. Schanning, D. E. Schenck, B. D. Sherwin, A. Shimizu, C. Shimmin, M. Shimon, P. Siritanasak, G. Smecher, H. Spieler, N. Stebor, B. Steinbach, R. Stompor, A. Suzuki, S. Takakura, T. Tomaru, B. Wilson, A. Yadav, and O. Zahn. A Measurement of the Cosmic Microwave Background B-mode Polarization

Power Spectrum at Sub-degree Scales with POLARBEAR. ApJ, 794:171, October 2014.

[95] R. J. Thornton, P. A. R. Ade, S. Aiola, F. E. Angilè, M. Amiri, J. A. Beall, D. T. Becker, H.-M. Cho, S. K. Choi, P. Corlies, K. P. Coughlin, R. Datta, M. J. Devlin, S. R. Dicker, R. Dünner, J. W. Fowler, A. E. Fox, P. A. Gallardo, J. Gao, E. Grace, M. Halpern, M. Hasselfield, S. W. Henderson, G. C. Hilton, A. D. Hincks, S. P. Ho, J. Hubmayr, K. D. Irwin, J. Klein, B. Koopman, D. Li, T. Louis, M. Lungu, L. Maurin, J. McMahon, C. D. Munson, S. Naess, F. Nati, L. Newburgh, J. Nibarger, M. D. Niemack, P. Niraula, M. R. Nolta, L. A. Page, C. G. Pappas, A. Schillaci, B. L. Schmitt, N. Sehgal, J. L. Sievers, S. M. Simon, S. T. Staggs, C. Tucker, M. Uehara, J. van Lanen, J. T. Ward, and E. J. Wollack. The Atacama Cosmology Telescope: The Polarization-sensitive ACTPol Instrument. ApJS, 227:21, December 2016.

[96] L. J. van der PAUW. A METHOD OF MEASURING SPECIFIC RESISTIVITY AND HALL EFFECT OF DISCS OF ARBITRARY SHAPE. In *Semiconductor Devices: Pioneering Papers*, pages 174–182. WORLD SCIENTIFIC, March 1991.

[97] Arthur R. Von Hippel. *Dielectrics and waves*. Artech House microwave library. Artech House, Boston, 1995.

[98] James R. Wait. Reflection at arbitrary incidence from a parallel wire grid. *Applied Scientific Research, Section B*, 4(1):393–400, Dec 1955.

[99] J. F. C. Wardle, R. A. Perley, and M. H. Cohen. Observational evidence against birefringence over cosmological distances. *Phys. Rev. Lett.*, 79:1801–1804, Sep 1997.

[100] J. L. Weiland, N. Odegard, R. S. Hill, E. Wollack, G. Hinshaw, M. R. Greason, N. Jarosik, L. Page, C. L. Bennett, J. Dunkley, B. Gold, M. Halpern, A. Kogut, E. Komatsu, D. Larson, M. Limon, S. S. Meyer, M. R. Nolta, K. M. Smith, D. N. Spergel, G. S. Tucker, and E. L. Wright. SEVEN-YEAR WILKINSON MICROWAVE ANISOTROPY PROBE (WMAP) OBSERVATIONS: PLANETS AND CELESTIAL CALIBRATION SOURCES. *The Astrophysical Journal Supplement Series*, 192(2):19, February 2011.

[101] Steven Weinberg. *The first three minutes: a modern view of the origin of the universe*. Basic Books, New York, 1977.

[102] E. Y. S. Wu, P. Ade, J. Bock, M. Bowden, M. L. Brown, G. Cahill, P. G.

Castro, S. Church, T. Culverhouse, R. B. Friedman, K. Ganga, W. K. Gear, S. Gupta, J. Hinderks, J. Kovac, A. E. Lange, E. Leitch, S. J. Melhuish, Y. Memari, J. A. Murphy, A. Orlando, L. Piccirillo, C. Pryke, N. Rajguru, B. Rusholme, R. Schwarz, C. O'Sullivan, A. N. Taylor, K. L. Thompson, A. H. Turner, and M. Zemcov. Parity violation constraints using cosmic microwave background polarization spectra from 2006 and 2007 observations by the quad polarimeter. *Phys. Rev. Lett.*, 102:161302, Apr 2009.

[103] J.-Q. Xia, H. Li, X. Wang, and X. Zhang. Testing CPT symmetry with CMB measurements. A&A, 483:715–718, June 2008.

[104] J.-Q. Xia, H. Li, G.-B. Zhao, and X. Zhang. Testing CPT Symmetry with CMB Measurements: Update after WMAP5. ApJ, 679:L61–L63, June 2008.

[105] Shuay-Pwu Ho Kevin T. Crowley Maria Salatino Sara M. Simon Suzanne T. Staggs Federico Nati Jonathan Ward Benjamin L. Schmitt Shawn Henderson Brian J. Koopman Patricio A. Gallardo Eve M. Vavagiakis Michael D. Niemack Jeff McMahon Shannon M. Duff Alessandro Schillaci Johannes Hubmayr Gene C. Hilton James A. Beall Edward J. Wollack Yaqiong Li, Steve Choi. Assembly and integration process of the first high density detector array for the atacama cosmology telescope, 2016.

[106] Matias Zaldarriaga. Cosmic microwave background polarization experiments. *The Astrophysical Journal*, 503(1):1, 1998.

[107] Matias Zaldarriaga. Nature of the $e-b$ decomposition of cmb polarization. *Phys. Rev. D*, 64:103001, Oct 2001.

[108] Matias Zaldarriaga and Uro š Seljak. All-sky analysis of polarization in the microwave background. *Phys. Rev. D*, 55:1830–1840, Feb 1997.